Microbubble size and dose effects on sonoporation *in vitro* and *in vivo*

by

Kang-Ho Song

B.S., Yale University, 2008

M. Eng., Cornell University, 2010

Department of Mechanical Engineering at
the University of Colorado at Boulder

2016

Dissertation submitted in partial fulfillment of the requirements for the degree of Doctor of Philosophy in the Department of Mechanical Engineering in the Graduate School of the University of Colorado at Boulder.

2016

This thesis entitled:
Microbubble size and dose effects on sonoporation *in vitro* and *in vivo*
written by Kang-Ho Song

has been approved by the following committee members

_____
Dr. Mark A. Borden, Advisor

_____
Dr. Brandon Harvey

NIH ACUC Protocol # *15-OSD-7*

The final copy of this thesis has been examined by the signatories, and we find that both the content and the form meet acceptable presentation standards of scholarly work.

Date: _____

_____
Dr. Virginia Ferguson

_____
Dr. Andrew Goodwin

_____
Dr. Arthur Gutierrez-Hartmann

_____
Dr. Mark Rentschler

_____
Dr. Wei Tan

Abstract

Song, Kang-Ho (Ph.D., Mechanical Engineering)

Microbubble size and dose effects on sonoporation *in vitro* and *in vivo*

Thesis directed by Associate Professor Mark A. Borden

Microbubbles interact with ultrasound to induce transient microscopic pores in the cellular plasma membrane in a highly localized thermo-mechanical process called sonoporation. The objective of this study was to advance *in vitro* and *in vivo* sonoporation through the development of novel devices and methodologies to precisely characterize the effects of microbubble size on suspended cell and blood-brain barrier sonoporation. The three core findings of our study were: 1) microbubble size allows for control over sonoporation power and energy, 2) the previously cited "soft" limit on *in vitro* sonoporation efficiency can be overcome utilizing sequential, low-energy sonoporation with small-diameter microbubbles, and 3) microbubble volume, not size, is the unifying parameter representing microbubble dose in blood-brain barrier (BBB) sonoporation. These findings greatly simplify the planning of future *in vivo* sonoporation studies, which benefit from a unified microbubble dose parameter, and provide precise methods to measure BBB permeabilization efficiency both *in vitro* and *in vivo*.

Dedication

To my family.

Acknowledgments

I am deeply grateful to my advisor of six years, Dr. Mark A. Borden, for his passionate mentorship and uncompromising vision of excellence. Under all circumstances, he has shouldered risk and uncertainty to enable me to explore far beyond the expected boundaries of our initial research goals. I would also like to thank Dr. Brandon K. Harvey at the NIH for his willingness to bridge two worlds, engineering and neurobiology, to materialize something truly remarkable. It has been my greatest honor to witness the nascent stages of this adventure, called sonoporation, with Dr. Borden and Dr. Harvey.

Over the years, several special individuals have guided my career in science. I would like to thank my first scientific mentor, Dr. Stephen M. Strittmatter at the Yale School of Medicine, for his generosity during my years in the field of neuroscience, and Dr. Stephane Budel, for his warm and tireless instruction during that time and beyond. I would like to thank my mentor during my stay at Cornell Biomedical Engineering, Dr. Michael L. Shuler, for his kind acceptance and mentorship of a new biochemist in the field of engineering. Additionally, it has been my privilege to have received the guidance and attention of untiring supporters, the members of my final examination committee: Dr. Virginia Ferguson, Dr. Andrew Goodwin, Dr. Arthur Gutierrez-Hartmann, Dr. Mark Rentschler and Dr. Wei Tan.

The studies presented here are the result of a community of like-minded people supporting my personal endeavor. I would first like to express my admiration and thanks to my student and good colleague, Alexander C. Fan, for his unwavering commitment towards improvement in all things. Through thick and thin, Alexander has demonstrated remarkable character and perseverance in assisting with the studies presented here. I would also like to thank my friends in

the department and the members of the Borden Laboratory, specifically Shashank Sirsi and Jameel Feshitan for their advice on experimental design, as well as Paul Mountford, Jake Dove, Jordan Lum and Alec Thomas, for their comradeship and shared passion in scientific pursuit. Additionally, I would like to thank my friends at the NIH: Pyry Koivula, Julie Necarsulmer and YaJun Zhang for help with animal-related procedures, as well as Christopher Richie, Emily Heathward and Susanne Bäck for their hospitality and assistance in the last year of my doctoral studies. Finally, I would like to thank John Brlansky and Dr. Michael Calvisi at UCCS for their kind assistance in modeling microbubble cavitation.

Table of Contents

List of Tables

List of Figures

Chapter 1. Introduction

1.1. Specific Aims

The purpose of my dissertation studies is to optimize both *in vitro* and *in vivo* sonoporation through characterization of the effects of microbubble size and concentration on tissue permeabilization efficiency and cell death. Specifically, centrifugally size-isolated 2-, 4- and 6-μm lipid microbubbles are utilized to:

1) Improve sonoporation through development of new sonoporation devices, changes to existing devices, and development of novel methods *in vitro* and *in vivo*.
2) Characterize the effect of microbubble size on *in vitro* persistence under therapeutic ultrasound (1 MHz, 10% duty cycle, 0.53 MPa, 2.0 W/cm^2, and 1000 cycles per pulse at 100 Hz pulse repetition frequency).
3) Characterize effects of microbubble size and concentration on sonoporation and cell death in suspended carcinoma (HeLa) cells, utilizing fluorescein isothiocyanate (FITC) dextran (70 kDa) as a model drug and ethidium homodimer-1 as a nonviability marker.
4) Correlate mathematically modeled relationships of microbubble power and energy dissipation to cell permeabilization efficiency.
5) Develop and implement an optimized sonoporation methodology, with the aim of surpassing previously published "soft limit" of 50% viable sonoporated cells (1), accounting for non-viable and disintegrated cells.
6) Characterize the effects of microbubble size, concentration and volume on blood-brain-barrier sonoporation, with the purpose of identifying unifying trends and parameters for future pre-clinical sonoporation studies for gene delivery to the rat brain.

1.2. Microbubble Composition

Microbubbles utilized in contemporary sonography and drug delivery are the result of characterization and optimization studies spanning decades. Initially approved by the U.S. Food and Drug Administration (FDA) for use as ultrasound contrast agents, the acoustically responsive nature of microbubbles have lent well to their use as acoustically activated cell and tissue permeabilization agents. Two components of microbubbles, the gas core and encapsulating shell, determine their biological functionality, surface structure, stability, and behavior under ultrasound (Fig 1.1). Microbubble formulations commonly utilize a perfluorocarbon gas, such as perfluorobutane (PFB, density: 11.2 kg/m^3 vs. air, 1.3 kg/m^3). This slows microbubble dissolution, and allows for a compressible, buoyant sphere which can oscillate volumetrically under acoustic stimulus and be concentrated through centrifugation. Altering the volume of gas in a microbubble significantly alters its echogenicity and cavitation behavior under ultrasound. Furthermore, the incorporation of a stabilizing shell, such as a polyethylene glycol (PEG) conjugated lipid monolayer, provides a semipermeable barrier to gas escape, reduces the immune response and offers a functionalizable surface for attachment of targeting ligands and therapeutics.

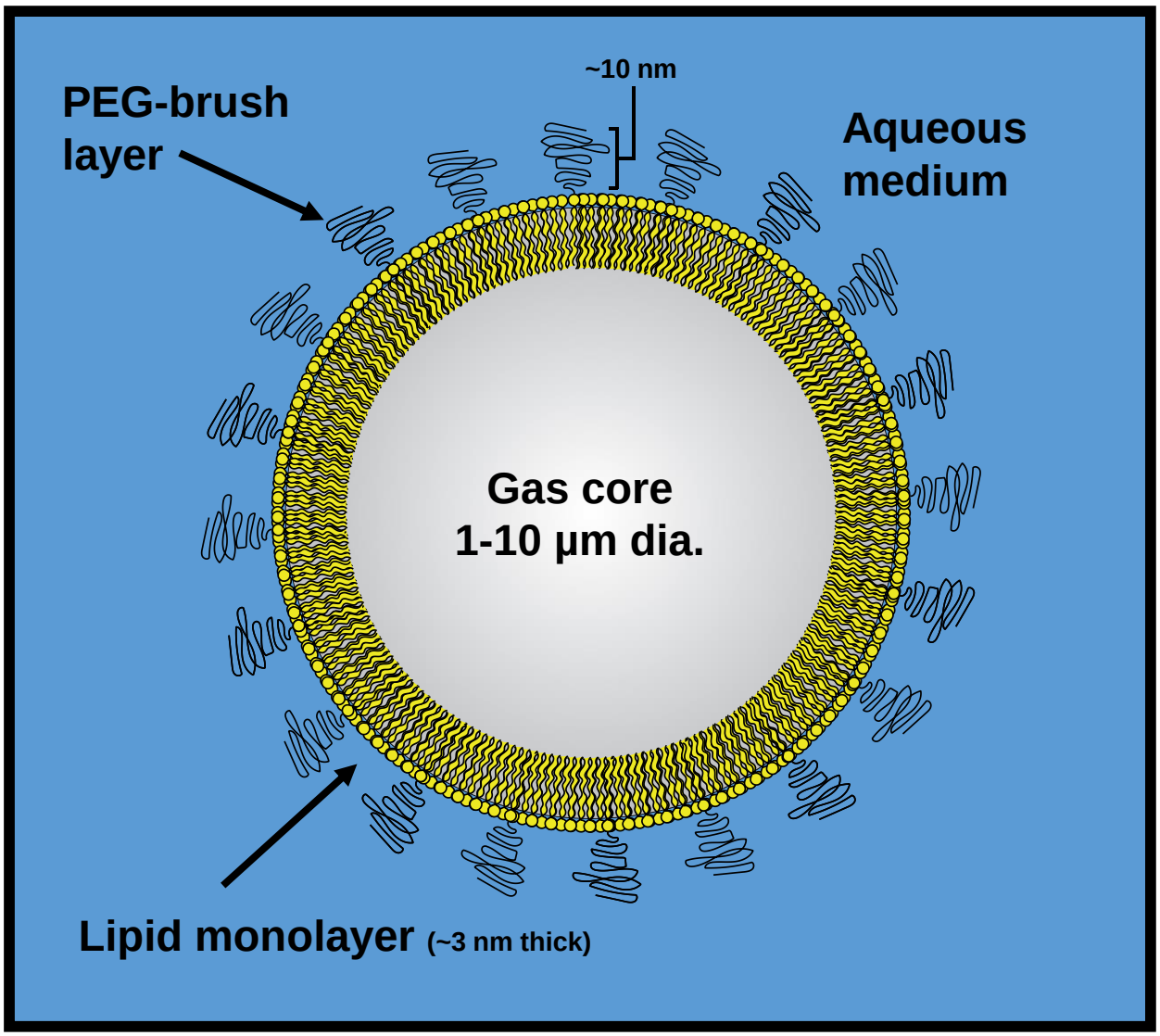

Figure 1.1. Diagram of the lipid microbubble, comprised of a dense gas core (air and/or perfluorocarbon), encapsulated with phospholipid (90 mol%) and lipid-polyethylene-glycol conjugates (10% mol%).

1.2.1. The gaseous core

Microbubbles can be generated when a gas-liquid interface is subject to mechanical agitation or temperature change (boiling). Microbubbles are generated in liquid by A) inducing outgassing of a dissolved gas solute or boiling of the liquid (2,3), B) microfluidic extrusion or flow focusing (4,5), or C) mechanically agitating a gas-liquid interface (Fig. 1.2). Once formed, microbubbles dissolve at a rate inverse to their size due to Laplace pressure (see *1.3 Passive microbubble dynamics*). A common strategy to enhance the lifetime of microbubbles in imaging and therapeutic applications has been the use of sulfur hexafluoride or perfluorocarbon gases.

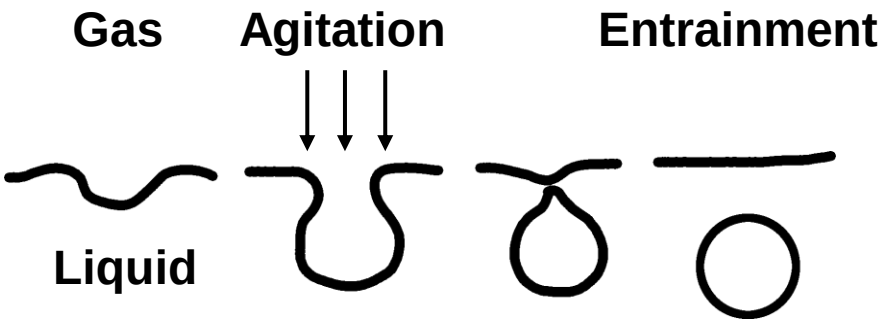

Figure 1.2. The formation of a microbubble through the entrainment of gas in liquid.

An essential advantage of perfluorocarbon gas is relatively high resistance to dissolution: about 300 times that of oxygen for perfluorobutane (PFB; 6). This effect is due to its hydrophobicity and surface area, and the stabilizing effect is found to be even more pronounced with the presence of a microbubble shell. Encapsulated PFB has shown to have 1400 times the dissolution resistance of oxygen when permeating through a lipid shell (6). This results in significantly better stability and consistency in size distribution over time for PFB microbubbles.

Additionally, the gas core represents a highly compressible volume which can expand or contract under environmental pressure gradients. In the case of acoustic waves, an absorption and scattering cross section, σ_a and σ_s, represented as a fraction of the absorbed and scattered power, P_a and P_S of incoming acoustic intensity, I, is attributed to the microbubble:

$$\sigma_a = \frac{P_a}{I}, \quad \sigma_s = \frac{P_S}{I} \tag{1.1}$$

The sum of absorbed and scattered cross sections represents the extinction cross section:

$$\sigma_e = \sigma_a + \sigma_s = 4\pi R^2 \frac{\Omega^4 - 1}{\left(1-\Omega^2\right)^2 + \left(\Omega\delta\right)^2} \frac{\delta}{\delta_c} \tag{1.2}$$

where Ω is acoustic frequency normalized to the resonance frequency, δ is the dimensionless damping constant, and δ_c is the damping constant for acoustic radiation.

Furthermore, under acoustic stimulus, microbubbles expand and contract in times of low and high pressure, respectively (Fig. 1.3), which will be discussed further in *1.4 Acoustic-microbubble dynamics*.

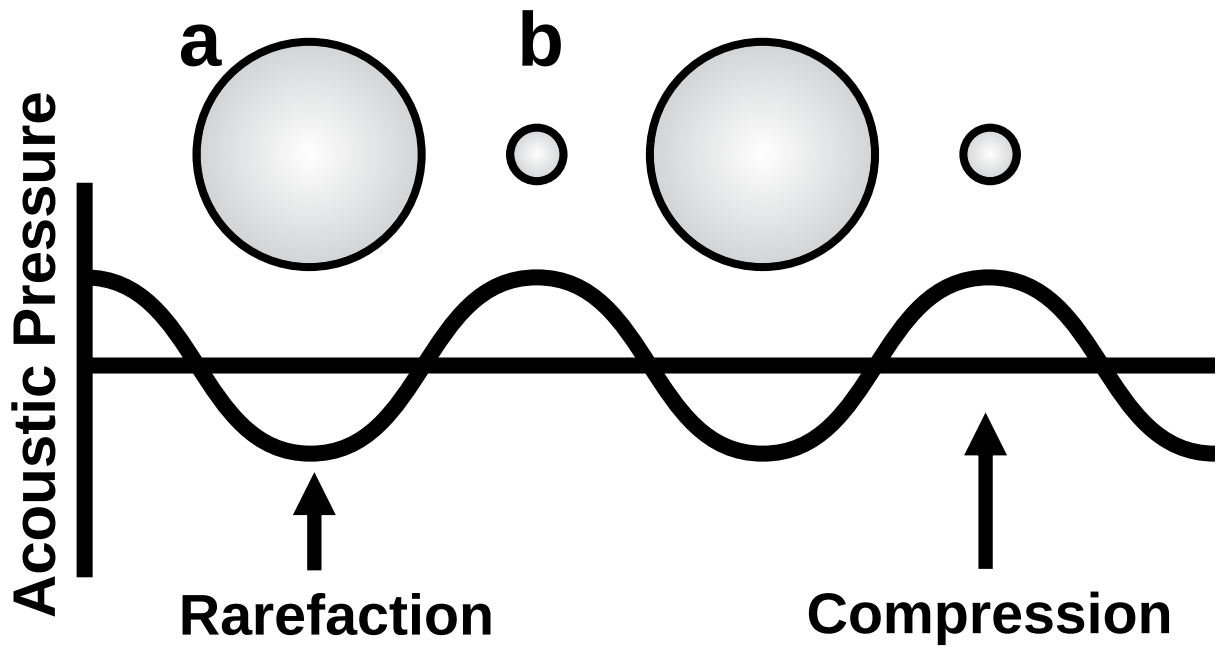

Figure 1.3. (a) Expansion and (b) contraction of microbubbles under the low (rarefaction) and high (compression) pressure regions of a sound wave.

1.2.2. The encapsulating layer

During microbubble formation, lipid molecules dispersed as aggregates in aqueous solution rapidly adsorb to the newly formed gas microsphere due to their amphiphilic structure—the hydrophobic tails organize facing the gas core, while the hydrophilic heads orient towards the surrounding water. The surface molecules continue to rearrange and pack to minimize configurational energy until equilibrium is reached, sometimes forming organized domains in the case of heterogeneous lipid formulations (Fig. 1.4). Lipid formulations are often comprised of phospholipids with varying tail lengths (16-22 carbons), with an emulsifier such as PEG-lipid conjugate, which reduce coalescence and immunogenicity. The addition of charged (cationic 1,2-stearoyl-3-trimethylammonium-propane, DSTAP, or anionic 1,2-distearoyl-sn-glycero-3-phosphate, DSPA) or conjugated (DSPE-PEG-biotin) lipids is generally conducted before microbubble generation, and can extend functionality. The lipid monolayer serves to stabilize the microbubble as a semipermeable barrier to gas escape, and its mechanical parameters, such as elasticity and viscosity, affect cavitation behavior.

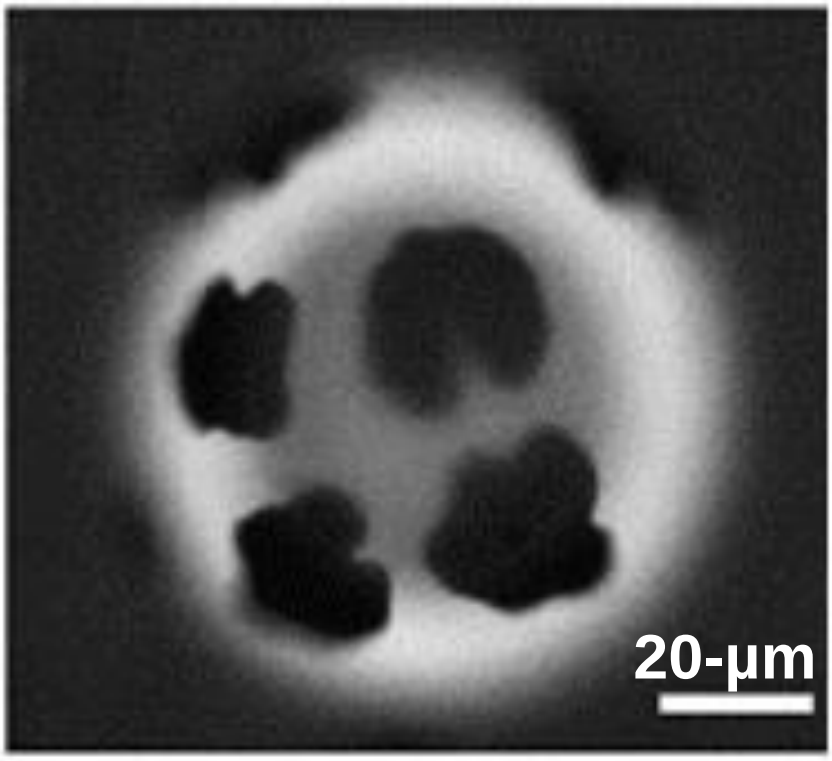

Figure 1.4. Lipid microbubble composed of 89% diC16:0PC, 10% PEG40S, 1% NBD-PC (fluorescent probe, light regions). Dark regions of indicate lipids in a condensed phase, while lighter regions indicate emulsifier (PEG40S)-rich regions in expanded state (Borden 2004).

1.3. Passive microbubble dynamics

1.3.1. Surface Tension

The tension at the gas-water interface stems from the affinity of water for itself through hydrogen bonding. Thus, gas-in-water emulsions adopt the smallest surface area (spherical) to minimize interactions between dissimilar molecules. Surface tension can be conceptualized as the asymmetric intermolecular "bonding" of water molecules at the gas-liquid interface, which cumulatively exerts a constricting pressure on the gas sphere. This increased pressure inside the bubble is known as Laplace pressure, expressed by surface tension, γ, and radius, R:

$$\Delta P = 2\gamma / R \tag{1.3}$$

Laplace pressure affects the partial pressure gradient between the gas phase and dissolved gases in the surrounding medium, affecting gas diffusion and thus, microbubble lifetime. To more accurately estimate microbubble lifetime, we must also account for other factors, such as the kinetics of gas diffusion.

1.3.2. The Epstein-Plesset Model of Microbubble Stability

An early mathematical model of microbubble stability was published by Epstein and Plesset in 1950, which incorporated surface tension, gas solubility, hydrostatic pressure, and degree of gas saturation of the medium outside the microbubble (8). The Epstein-Plesset model utilizes the mathematics of gas diffusion to predict the change in mass (and radius) of the microbubble as a function of gas diffusivity (κ), gas concentration gradient (δ) across the shell, and time (t):

$$\frac{dR}{dt} = \frac{\kappa\delta}{\rho}\left(\frac{1}{R} + \frac{1}{\sqrt{\pi\kappa t}}\right), \quad \delta = c_i - c_s \tag{1.4}$$

where c_i and c_s represent the actual concentration (or partial pressure through Henry's law) of gas in the surrounding medium, and partial pressure at the microbubble surface, respectively.

In this simple relationship, we can see that a decrease in gas density, ρ, or an increase in gas diffusivity and/or concentration gradient result in an increase in the rate of change in radius of the microbubble. The effect of surface tension is accounted for in the concentration gradient, specifically in the surface concentration term c_s. The EP model accomplishes this by first equating the pressure term of the ideal gas law:

$$P = nBT/V \tag{1.5}$$

to the sum of Laplace pressure (Eq. 1.3) and ambient pressure (P_A) to obtain:

$$P_A + \frac{2\gamma}{R} = \left(\frac{B}{M} \rho(R) T \right) \tag{1.6}$$

where M is the molar mass of the gas, B is the universal gas constant, $\rho(R)$ represents mass density and T is absolute temperature. Microbubble density, $\rho(R)$, is solved for, and substituted into Equation 1.4 to obtain *dR/dt* containing a surface tension term:

$$-\frac{dR}{dt} = \frac{\kappa\delta}{\rho(\infty) + 2\tau/3R} \left(\frac{1}{R} + \frac{1}{\sqrt{\pi\kappa t}} \right) \tag{1.7}$$

where $\tau = 2M\gamma/BT$.

We see from the Epstein-Plesset equation that increasing radius and molecular weight (nestled within the τ term) reduces the change in microbubble radius.

1.3.3. Borden and Longo Revision

The first significant revision to the Epstein-Plesset equation occurred in 2002, with the inclusion of a gas permeability-resistance term representing the barrier effect of an encapsulating shell. This became especially relevant for commercially available ultrasound contrast agent formulations such as Definity® (Lantheus Medical Imaging, North Billerica, MA, USA) and Optison™ (GE Healthcare, Little Chalfont, UK), which are stabilized using lipid and protein shells, respectively.

Borden and Longo incorporate this shell permeability resistance term as R_{shell} in the evolution of the Epstein-Plesset model:

$$-\frac{dR}{dt} = \frac{L_g\left[\left(1+\frac{2\gamma}{P_A R}\right) - f\right]}{\left(\frac{R}{\kappa} + R_{shell}\right)\left(1+\frac{4\gamma}{3P_A R}\right)}, \quad f = \frac{c_i}{c_s} \tag{1.8}$$

where L_g is the Ostwald coefficient, the degass ratio is f, and c_s is the saturation concentration of the dissolved gas in the surrounding medium at the ambient temperature.

Note for the surrounding medium:

- if $f < 1$: the medium is undersaturated with the gas
- $f > 1$: the medium is oversaturated with the gas
- $f = 1$: the medium is saturated with the gas.

We see that as the gas permeability resistance of the shell increases, the rate of bubble dissolution decreases. Additionally, we see that omitting the permeability resistance of the shell yields the original Epstein and Plesset equation for a naked microbubble.

1.3.4. Katiyar and Sarkar Revision

The most recent revision of the Epstein-Plesset equation is from Katiyar, Sarkar et al., who adds elasticity to diffusivity and shell permeability (9). The revision begins with the Epstein and Plesset model. The Katiyar-Sarkar model then adds the surface elasticity term, E^s, to surface tension, γ, in three logical cases:

$$\gamma(R) > 0, \quad \text{for} \quad \frac{E^S}{\gamma_0} \ll 1, \tag{1.9}$$

and

$$\gamma(R) > 0, \text{ for } R > R_s, \tag{1.10}$$

$$\gamma(R) > 0, \quad \text{for} \quad \frac{E^S}{\gamma_0} \ll 1, \tag{1.11}$$

$$\gamma(R) = 0, \text{ for } R \ll R_s \text{ and } \frac{E^S}{\gamma_0} > 1, \tag{1.12}$$

$$\text{where } R_S - R_0(1 - \frac{\gamma_0}{E^S})^{1/2} \tag{1.13}$$

That is, low surface stress when the bubble is at a "stress-free" size (R_s), and greater surface stress due to a bubble with radius smaller than R_s (compression) or a microbubble with radius greater than R_s (expansion). This results in a more detailed expression of surface tension:

$$\gamma(R) = \gamma_0 + E^S \left[\left(\frac{R}{R_0}\right) - 1\right] \tag{1.14}$$

Note that $\gamma(R) = 0$ represents a bubble in stress-free conformation. We incorporate equation 1.14 into the Borden-Longo model, obtaining:

$$-\frac{dR}{dt} = \frac{3L_g\kappa\left[P_A(1-f) + \frac{2\gamma}{R} + \frac{2E^S}{R}\left\{\left(\frac{R}{R_0}\right)^2 - 1\right\}\right]}{\left(\frac{R}{\kappa} + R_{shell}\right)\left[3P_A + \frac{4\gamma}{R} + \frac{4E^S}{R}\left\{2\left(\frac{R}{R_0}\right)^2 - 1\right\}\right]} \tag{1.15}$$

We see that as the elasticity term, $\frac{2E^S}{R}$, goes to zero, the equation returns to the Borden-Longo revision of the Epstein-Plesset equation.

1.3.5. Summary of Mathematical Models

These mathematical models uphold five fundamental laws of microbubble stability:

1. As **microbubble size** decreases, bubble lifetime decreases.
2. As **gas concentration** in the liquid environment decreases, bubble lifetime decreases.
3. As **gas diffusivity** into the liquid environment increases, bubble lifetime decreases.
4. As **surface tension** of the bubble shell increases, bubble lifetime decreases.
5. As **shell permeability resistance** to gas increases, bubble lifetime increases.
6. As **shell elasticity** increases, bubble lifetime increases.

1.4. Acoustic microbubble dynamics

1.4.1. The Marmottant model

Microbubbles in liquid water oscillate strongly under acoustic stimulation due to the highly compressible gas core. Several mechanisms have been predicted to affect the velocity and symmetry of these oscillations, some of which have been experimentally verified for stable cavitation, defined as periodic non-terminal microbubble expansion and contraction (10,11). However, much of our current understanding on inertial cavitation (transient oscillation resulting in violent collapse and subsequent fragmentation) remains limited to experimental analyses.

In 2005, Marmottant et al. developed a model of microbubble cavitation based on the Rayleigh-Plesset model of unencapsulated microbubble oscillation (12), which itself was built upon the Navier-Stokes equation of motion for an oscillating compressible sphere in a viscous medium. The main addition of the Marmottant model was the inclusion of realistic lipid monolayer shell effects, such as shell friction (shell viscosity) and, more importantly, a shell-dependent surface tension term that captured buckling, a linear elastic regime, and rupture. Distinguishing between these three shell states allowed for more accurate non-linear oscillation, such as compression-only behavior observed experimentally (Fig. 1.5; 13).

The first of these three shell states is the buckled state (occurring during the ultrasonic compression phase), in which zero tension is assigned to the shell under a threshold surface area $A_{buckling}$. In the buckled state, shell strain is relieved through microscopic fold generation (upheavals and invaginations). The surface tension is considered to be zero here owing to complete exclusion of water from the gas surface by the tightly packed lipid molecules.

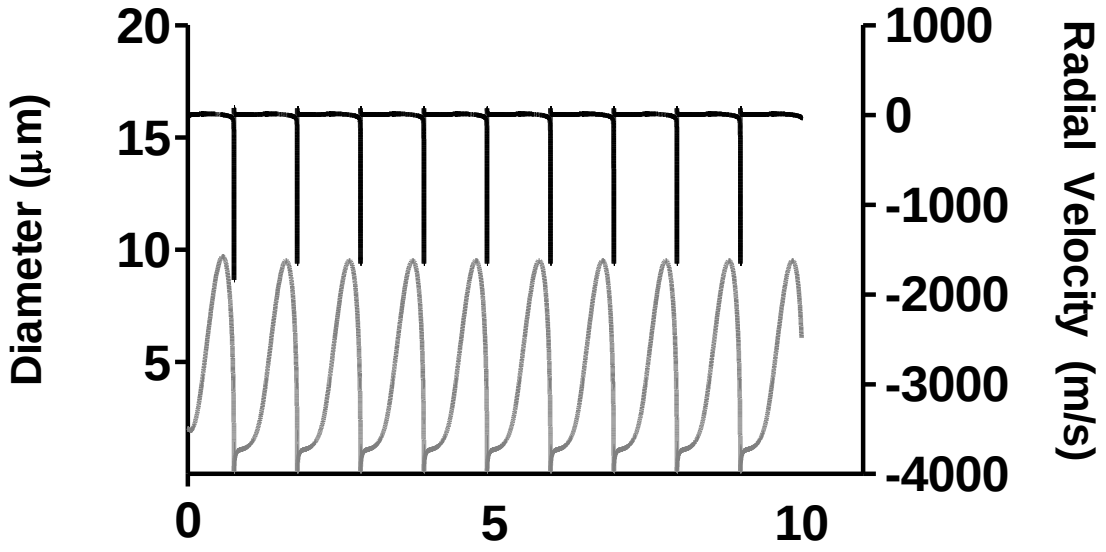

Figure 1.5. Diameter-time plot of microbubble expansion and collapse (gray line) and radial velocity (black line). Simulations courtesy of Calvisi et al.

Above the buckling threshold ($A_{buckling}$) and below the shell break-up threshold ($A_{breakup}$), a linear elastic regime dictates the dependence of surface tension (γ) with the elastic compression modulus (χ) and surface area (A):

$$\gamma = \chi(\frac{A}{A_{buckling}} - 1) \tag{1.16}$$

This term allows for modeling of shell material with both low and high tensile strength, such as lipids and polymer shells, respectively. Lastly, the expanded/ruptured shell was treated as an unencapsulated shell, with surface tension equivalent to that of water owing to the incoherency of the lipid shell and exposure of the gas surface to surrounding water. On collapse, $A_{rupture}$ dictates the start of the elastic regime as opposed to $A_{break\text{-}up}$, due to the hysteresis in the cohesion of the shell before and after break-up. This contributes to asymmetry in the expansion and collapse stages

of oscillation, such as “compression-only” behavior observed under high-speed videomicroscopy (14). Beyond these surface tension terms, the Marmottant model incorporated shell and liquid viscosity, as well as Laplace capillary pressure to balance the stresses between gas and liquid pressures at the microbubble wall. Basic hydrodynamics in the Marmottant equation were modeled as in the classic Rayleigh-Plesset equation, which incorporated the acoustic driving pressure.

The Marmottant model bridges the regimes of low and high acoustic forcing that are captured by the Rayleigh-Plesset equation (See section *2.3.5 Theoretical radial dynamics calculations* for Marmottant equations and modeling). At low acoustic forcing, both models predict linear oscillations, where expansion and contraction are equal in magnitude. The Marmottant model deviates from the Rayleigh-Plesset equation at moderate acoustic behavior, where the Marmottant model predicts the experimentally observed “compression-only” behavior, in which the magnitude of compression was noticeably more than that of expansion. At high acoustic forcing, the Marmottant model then re-converges with the Rayleigh-Plesset equation and predicts highly asymmetric expansion and compression. The expansion phase during rarefaction is relatively slow compared to the rapid collapse and rebound observed during compression (Fig. 1.5).

In summary, encapsulated microbubble oscillations can be modeled to reasonable accuracy utilizing the Marmottant model, which incorporates elements of past models (Rayleigh-Plesset) with a flexible surface-tension term representing the behavior of buckled, elastic and ruptured lipid shell states. In the context of microbubble size, the Marmottant model predicts that larger microbubbles oscillate at smaller relative amplitudes than smaller microbubbles. Limitations of the Marmottant model are: 1) the core is treated as an ideal gas, which may affect predictions at

very high compression ratios where the core should be treated as a real gas; and 2) the gas and shell mass is assumed to be constant, although in reality, gas may accumulate (rectified diffusion) or dissolve, and the shell material may collapse and detach from the surface.

1.4.2. Microbubble acoustic phenomena

Microbubble cavitation has been the subject of investigation in several studies, often as microbubble-size and acoustic-parameter-dependent phenomena. In 2004, Postema et al. listed oscillation, translation, coalescence, fragmentation, sonic cracking and jetting as typical microbubble behaviors under ultrasonic stimulation (15). Translation will be covered separately in the description of Bjerknes forces below.

Non-hysteretic oscillation as described by Postema et al. is best demonstrated by stable cavitation, in which microbubbles demonstrate periodic and non-periodic oscillation with minimal loss in gas volume (15). All cavitation models (such as the Marmottant equation) can be considered to simulate oscillation without volume hysteresis. The efficacy of stable cavitation in cell sonoporation has been shown to rely upon ultrasound parameters more so than inertial cavitation, due to the wide range of mechanical output amplified by the enhanced persistence of the microbubbles (16–18). Stably cavitating microbubbles have been shown to porate cells, demonstrate prolonged translation, and induce endocytosis in non-porated cells (19,20).

Inertial cavitation can be described as microbubble oscillation which leads to short-term collapse via jetting, sonic cracking, and/or fragmentation. Chomas et al. and other investigators have shown that microbubbles expanding beyond a certain radial expansion ratio undergo inertial cavitation (21–23). Of these, microbubbles contracting near boundaries have been shown to result

in jetting, or the propulsion of an involuted liquid jet toward or away from the boundary, depending on the type of boundary. This collapse asymmetry is thought to be due to the free hemisphere of the microbubble retaining a high velocity compared to the restricted, surface-side hemisphere. In the case of jetting, the velocity of the free hemisphere exceeds the boundary of the restricted hemisphere, and a funnel-shaped liquid protrusion is formed as collapse causes the free boundary to strike and pass through the restricted boundary. Jetting phenomena have been shown to result in sonoporation in past studies, inducing well-defined circular pores under scanning electron microscopy (SEM), while stable cavitation has been shown to result in more membrane irregularities (16–18).

Fragmentation is another form of inertial cavitation, which results in the fission of microbubbles into smaller microbubbles. In 2001, Chomas et al. observed fragmentation occurring at maximum compression, which suggested that some of the compression energy was utilized in causing interfacial splitting and microbubble fission (21). The distinction in effect between fragmentation and jetting in sonoporation has not yet been characterized in depth; however, it has been speculated that shock waves from fragmentation may affect sonoporation (15), and jetting may occur in microbubbles resulting from fragmentation, which would also result in sonoporation. Sonic cracking, or the expulsion of gas away from a surface due to defects in the shell, is a form of inertial cavitation which has been observed to propel the remaining shell into the cell surface, inducing poration and potentially aiding in intracellular delivery of shell-loaded drugs (15,24).

1.4.3. Bjerknes forces

Microbubble translation under acoustic pressure can be described by Bjerknes forces, which increase with microbubble radius and driving pressure intensity (25). The effect is maximal when forcing at the microbubble resonance frequency. Two types of Bjerknes forces have been defined: primary Bjerknes forces (single-microbubble translation in the direction of the propagating wave, of particular interest in traveling waves and summarized below), and secondary Bjerknes forces (multi-microbubble interactions which result in attraction or repulsion between microbubbles). The cause of primary Bjerknes forces can be sourced to the acoustic pressure gradient formed by ultrasonic wave, as well as the size-dependence of oscillation (given a fixed frequency): $f_b = \frac{4}{9}\pi k^2 \langle R^3(t) p_a(t) \rangle$, in which R^3 corresponds to volume and $p_a(t)$ corresponds to acoustic pressure, where the Bjerknes force (f_b) direction is relative to the acoustic anti-node (26,27). In cases where the f_b is negative, the microbubble attracts towards the anti-node and remains trapped, while positive f_b results in repulsion and displacement away from the anti-node. In effect, one can expect greater displacement per time with larger microbubbles, while smaller microbubbles demonstrate reduced velocities. Additionally, small Reynolds numbers contribute to very rapid deceleration after each ultrasonic pulse, which is speculated to result in sharp step-wise displacement. It is important to note from the k^2 term, where k is the wave number, that microbubbles greater than the Minnaert resonance radius are repelled from the pressure anti-node, while the inverse is true for microbubbles smaller than the resonance radius. Microbubble translation resulting from such acoustic radiation forces have been observed at speeds up to 500 mm/s, resulting in cell membrane deformation, sonoporation and cell death (17,25).

1.5. Historical perspective on *in vitro* sonoporation

Independent Variable	Effect	References
Inertial cavitation dose (ICD)	Increased permeabilization, cell death, microbubble destruction	(28)
Acoustic intensity	Increased mechanical index (MI), jetting, sonic cracking, pore size, cell death, transfection rates, propidium iodide (PI) uptake, permeabilization, ICD, cellular debris, endocytosis	(19,20,24,29–33)
Acoustic frequency	Reduced MI, cell death	(19,34)
Pulse duration and PRF	Increased pore size, permeabilization, cell death, transfection rates, duration of poration (recovery time), PI uptake, microbubble translation, increased ultrasonic energy, ICD	(17,19,19,35)
Treatment duration	Increased permeabilization, cell death, microbubble destruction	(33,36)
Microbubble diameter	Increased pore size, duration of poration (recovery time), PI uptake, reduced jetting	(17)
Microbubble rigidity	Increased transfection	(37)
Microbubble transience	Reduced transfection, increased cell viability	(37)
Cell-microbubble distance	Reduced permeabilization	(17)
Rotation of sample	Increased permeabilization	(34)
Microbubble concentration	Increased permeabilization, cell death, decreased rate of microbubble destruction	(19,36)
Drug size	Reduced uptake of model drug	(32)
Ca2+	Pore resealing	(38,39)
Increased permeabilization	Reduced cellular adhesion	(19)

Table 1.1. Cellular effects of sonoporation parameters.

1.5.1. Experimental studies in single-microbubble sonoporations

Studies on sonoporation with single cells have allowed for close observation of microbubble poration mechanics without the complexities of multi-cell physiology and multi-microbubble effects encountered in population studies. Early investigations studied the effects of microbubble size, distance to the cell and ultrasonic parameters, as well as methodologies to improve drug delivery, such as ligand-receptor binding. The resulting pore sizes, cell recovery mechanisms and diffusion of material into cells were examined. Characterizing the effects of these parameters was seen to be an essential step towards optimizing multi-cell in vitro studies, in which such effects would manifest themselves with confounding effects of multi-cell physiologies and multi-microbubble effects, such as secondary radiation forces.

In 2005, Prentice et al. (24) investigated the sonoporation of plated MCF7 breast cancer cells (characteristic length: 20-25 μm) with Optison™ protein/perfluoropropane microbubbles (mean diameter: 2.0-4.5 μm (40) placed approximately 27 μm from the cells during single-shot ultrasound (1 MHz center frequency, 1.39 MPa peak negative pressure (PNP), 1.39 mechanical index (MI), 20 cycles). Using high-speed videomicroscopy, the authors observed microbubble translation to the cell monolayer and asymmetric flattening of the microbubble against the monolayer. At 8 μs after insonation, microjetting (the formation of a sharp involuted water jet from the flattening microbubble) was observed, which resulted in poration as confirmed by atomic force microscopy (AFM). Jet velocity was observed to be 5 m/s. Interestingly, in 35% of cases at the above ultrasound settings, "sonic cracking", or the rapid expulsion of gas and propulsion of shell material, was observed, although permeabilization was unconfirmed in this case. Sonic cracking is a phenomenon associated with brittle, chemically cross-linked microbubble shells (in this case disulfide bridges), such as those comprising protein or polymer (15,41). While molecular

diffusion into the cell and cell death were not examined, it was hypothesized that the large pores would cause a significant influx/efflux of material and cell death had either parameter been measured.

In 2006, van Wamel et al. studied the sonoporation of plated bovine endothelial cells (characteristic length = 10-50 μm) with lipid/perfluorobutane microbubbles (BR14™, mean diameter = 2.9 μm) with a 5 s ultrasonic insonation (1 MHz, 0.4 MPa PNP, 0.4 MI, 50 Hz pulse repetition frequency (PRF), 10 cycles; 42). High-speed videomicroscopy was utilized to image stable (non-jetting) microbubble cavitation on the cell surface, as well as propidium iodide (PI) uptake into permeabilized cells. Cells were allowed to recover for 15 to 180 s before PI was added to the solution to characterize cell permeability and membrane recovery. Two cellular response phenomena were observed and characterized: (1) the progressive reduction of PI uptake in reversibly permeabilized cells over the course of 3 min, indicating cell recovery, and (2) increasing PI uptake in irreversibly permeabilized cells. Additionally, membrane recovery time did not vary significantly between trials, suggesting similar behavior between the cells examined. The results suggested that stable microbubble oscillations (without jetting) could permeabilize cells through membrane deformation, as opposed to jet-induced puncture.

In 2009, Kudo et al. investigated sonoporation of plated bovine endothelial cells (10 x 150 μm^2) with lipid/galactose-shell, air-core microbubbles (Levovist®, 1–20 μm) during single-shot pulsed ultrasound (1 MHz, 1.1 MPa PNP, 1.1 MI, 3 cycles; 39). Using light microscopy and scanning electron microscopy (SEM), they showed co-localization of microbubbles before sonication with PI internalization after sonication. Utilizing high-speed videomicroscopy, the authors captured microbubbles expanding to approximately ten times the initial radius while in immediate contact with cells, then collapsing to sizes undetectable by their inverted microscope.

Further videomicroscopy of Optison and Levovist microbubbles showed smaller (3 μm) microbubbles formed an involuted jet, while larger (20 μm) microbubbles crumpled and deformed but did not form a jet. Interestingly, the smallest microbubble examined (1 μm, Levovist) fragmented into smaller microbubbles before disappearing, with no jet formation. Increased Ca^{2+}-mediated cell repair after sonoporation also was documented with Ca^{2+}-supplemented media, intracellular Ca^{2+}-binding dye (fura-2) and PI. Utilizing Ca^{2+} was later utilized by Zhou et al. to inhibit pore resealing.

In 2009, Zhou et al. (43) utilized patch-clamp transmembrane current measurements (TMC) of plate-fixed Xenopus laevis oocytes (mean diameter = 1.1 mm) sonicated with Definity™ lipid/perfluoropropane microbubbles (1–10 μm diameter) for a single-shot 200 ms duration at 1 MHz and 0.3 MPa PNP (MI = 0.3). TMC results were converted to pore size by a simple diffusion model, which yielded a median pore diameter of ~100 nm. Additionally, the effective range of poration from the microbubble center was generalized to ~4 μm. TMC measurements also showed a drastic change within 0.3 s, which slowed over the course of approximately 5 s.

In a subsequent study, Zhou et al. (2011) investigated the effect of microbubble size and distance from plated cells by generating inception-cavitation microbubbles with a femtosecond laser, then optically trapping the air microbubbles near a Xenopus oocyte utilizing the same laser (17). A sustained 7 MHz ultrasonic pulse (1.4 MPa PNP, 0.53 MI, 70 cycles, 10 kHz PRF) was utilized to push the microbubbles to a set distance D from the cell, and a single-shot 1.5 MHz ultrasonic pulse (1.5 vs. 1.7 MPa PNP, 20 vs. 60 cycles) was utilized to induce microbubble cavitation. A strong relationship between microbubble-to-cell standoff distance D and significant TMC change was established: microbubbles only affected cellular TMC when D was approximately 75% of the microbubble diameter, with rapidly diminishing effects outside that

range. Additionally, Ca^{2+}-free media was utilized to inhibit pore resealing, and the cell was subsequently preserved for SEM. The results showed a clear increase in pore size and duration of permeabilization utilizing larger microbubbles and longer pulse lengths. Two sonoporation mechanisms were observed: 1) microbubble collapse with jetting near the cell membrane and 2) symmetric microbubble oscillation against the membrane. Both mechanisms were documented to be effective at sonoporating cells. Microbubble translation was seen when longer (60 cycle) pulse durations were used at low amplitudes of 0.27 MPa PNP (MI = 0.22), which effected indentation of the cell membrane. A delayed TMC change, indicating permeabilization of the cell membrane, was seen in this case.

Qiu et al. (2012) studied sonoporation and transfection of MCF-7 breast cancer cells (20-24 μm) with phospholipid/sulfur-hexafluoride microbubbles (SonoVue®, mean diameter = 3-4 μm) and EGFP plasmid DNA at ultrasound settings of 1 MHz, 0.05-0.3 MPa PNP, 0.05-0.3 MI, 10-15 cycles, 5-60 s total exposure times and unspecified PRF (29). Utilizing SEM imaging of fixed cells post-sonoporation, the authors found increasing pore sizes correlating to increased ultrasound intensity and treatment duration: 200-1100 nm pore diameters for 0.05-0.3 MPa.

Fan et al. (2012) conducted studies on single anti-CD51 antibody conjugated lipid microbubbles (Targestar SA™, median diameter = 2.6 μm) and HEK cells (13-20 μm) under ultrasound settings of 1.25 MHz, 0.17 vs. 0.26 MPa PNP (0.15 vs. 0.23 MI), 10 cycles (44). Microbubbles were seen to selectively attach to individual cells by ligand-receptor mediating binding. Sonoporation was visualized with fluorescence microscopy in the presence of PI, showing that larger microbubbles increased PI uptake. Additionally, cells with internalized calcein were sonoporated to examine calcein efflux from the cells. The results showed that calcein efflux was smaller than the influx of PI, despite similarity in size for both molecules.

Additional studies by Fan et al. (2013) characterized the effects of acoustic intensity on sonoporation (45). Similar to the aforementioned experiment, anti-CD51 Targestar SA™ microbubbles were attached to and sonoporated with plated HUVEC cells (17 μm) and cellular permeability and transfection were measured through PI and GFP expression, respectively. Pore size was calculated through video analysis of PI diffusion throughout the intracellular space, and extrapolating the initial pore diameter from a simple diffusion model. Three microbubble behaviors were observed at 1.25 MHz, 20 Hz PRF, 1 s exposure: 1) 0.06 MPa (MI = 0.05) acoustic pressure, 8,000 cycles, which effected the least permeabilization (<3%) but highest cell viability (95%); 2) 0.4 MPa (MI = 0.36), 8,000 cycles, which effected more permeabilization (7%) but minimal cell viability (7%); and 3) 0.4 MPa sustained ultrasound, 6 cycles, which effected the most permeabilization (33%) and medium cell viability (51%). Significant microbubble aggregation was observed during stable cavitation, as well as compelling evidence of cellular indentation and membrane compression effected by microbubble translation under primary Bjerknes force. Additionally, one, two and twenty shot pulses at 1.25 MHz, 0.4 MPa, 20 Hz PRF, 6 cycles per pulse were compared, with higher pulse numbers increasing pore diameter and PI uptake and reducing cell viability.

In 2013, Gelderblom et al. (30) studied the sonoporation of plated HUVEC cells with lipid/perfluorobutane microbubbles (mean diameter = 4 μm) at varying ultrasound settings (1 MHz; 0.2, 0.4 vs. 1.2 MPa PNP; 0.2-1.2 MI). Resulting sonoporation was visualized through first-of-its-kind 10 fps fluorescence videomicroscopy of PI staining. Results from microscopy showed progressively increasing PI spread within the cell from an individual pore, as well as increasing permeabilization in cells correlating to ultrasound intensity: at 200 kPa PNP, 50% of cells showed PI uptake, while at 1.2 MPa PNP, all of the cells showed PI uptake.

1.5.2. Experimental studies on cellular biological response

The study of cellular biological response has allowed for improved analysis and optimization of *in vitro* sonoporation. A handful of studies have examined the effect of sonoporation on cellular metabolism (20,46), change in cytoskeletal structure (47,48), nuclear organization (46), and recovery mechanisms (38,39,46), with applications towards translating sonoporation to more time-dependent processes such as transfection. The following studies characterize a wide variety of cell lines; however, to the best of our knowledge, characterization of primary cell response to sonoporation has yet to be published.

In 2008, Juffermans et al. (48) studied the effect of sonoporation on BK_{Ca}-channel dependent Ca^{2+} transport in plated H9c2 rat cardiomyoblast cells (10-42 μm) utilizing phospholipid/sulfur-hexafluoride microbubbles (Sonovue®, mean radius = 1.5-2 μm) and 30-s sustained ultrasound (1 MHz, 0.05 vs. 0.25 MPa PNP, 0.05 vs. 0.25 MI, 20 Hz PRF, 100 cycles). Membrane potential analysis was conducted with di-4-ANEPPS, an internalized fluorescent dye, which was observed to undergo a 10% increase in fluorescence intensity per 100 mV increase in transmembrane electric potential. They observed an 18% to 25% increase in median fluorescence intensity (MFI) for 0.05 MPa to 0.25 MPa (MI = 0.05-0.25), respectively, over control samples (ultrasound only), just inside the cell membrane. The fluorescence increase was observed at sonoporation sites and indicated localized hyperpolarization (significant influx of Ca^{2+} ions, as opposed to compensatory efflux of K^{+} ions expected during membrane permeabilization). Hyperpolarization was confirmed to be instigated by BK_{Ca} through the inclusion of two BK_{Ca} channel blockers (catalase or Ibtx), which completely eliminated MFI changes at sonoporation sites (<1.0% change in MFI). Slight depolarization was seen to occur, however, in samples treated by the most intense ultrasound (0.25 MPa PNP; MI = 0.25).

The same year, Zhou et al. (38) investigated the Ca^{2+}-dependence of post-sonoporation membrane healing, utilizing Xenopus laevis oocytes and lipid/perfluoropropane microbubbles (Definity™, 1-10 μm diameter) and single-shot ultrasound (1.06 MHz, 0.3 MPa PNP, 0.3 MI, 200 cycles) in the presence of 0-3 mM Ca^{2+}. Voltage clamp measurements showed that membrane recovery was a two-stage process with a time-dependence on Ca^{2+} concentration: rapid resealing occurred in the first phase, and slower resealing occurred in the second. Interestingly, Ca^{2+} concentrations under 0.54 mM effected incomplete recovery even after 60 min; full membrane recovery required a Ca^{2+} concentration of at least 0.54 mM over 170 s. Recovery durations were seen to decrease as concentration increased, with 3.0 mM of Ca^{2+} effecting recovery after only 10 s.

Fan et al. (2010) studied Ca^{2+} loss from H9c2 cells as a function of intracellular fluorescent Ca^{2+}-binding dye (fura-2) intensity utilizing Definity microbubbles under single-shot ultrasound (1 MHz, 0.27 MPa PNP, 0.27 MI, 10-15 cycles). Sonication was observed to induce a rapid increase in intracellular Ca^{2+} concentration over 50 s, corresponding to PI influx into cells over 60 s (16). In a small number of cells, no significant PI uptake was realized while small-magnitude Ca^{2+} efflux was observed. The presence of delayed (40 s) Ca^{2+} uptake was also seen in some cells, which indicated that Ca^{2+} efflux from other adjacent cells was triggering a "calcium wave" response in surrounding non-sonoporated cells.

In 2012, Zeghimi et al. (46) investigated the gross microcellular physiology of U-87 MG human primary glioblastoma cells utilizing lipid/perfluorobutane microbubbles (BR14™, mean diameter: 2.9 μm) under sustained ultrasound (1 MHz, 1 W/cm^2 intensity, unspecified PRF, 20 cycles, 10 s vs. 60 s total exposure duration). SEM images of cells fixed immediately after sonoporation revealed a significant increase of 50-100 nm open caveolae (invaginated lipid rafts

which can expand and form endocytotic vesicles) after sonoporation, which appeared pore-like in morphology. Cells fixed 15 min after sonoporation were observed to have a significantly smaller number of invaginated structures. Larger (70-160 nm) pore-like structures were seen to disappear before smaller (10-50 nm) structures, which indicated prioritization of cellular repair favoring larger membrane defects. Transmission electron microscopy (TEM) images of intracellular structures showed chromatin condensation (a transcriptional and reproductive inhibitor and potential protective mechanism), as well as a lightening of the cytoplasm (reduced cytoplasmic viscosity and cytoskeletal change) in sonoporated cells, which suggested that the cellular response mechanisms had a retarding effect on cellular metabolism.

In 2013, Chen et al. (49) studied the developmental and morphological impact of sonoporation on suspended HL-60 human leukemia cells and adherent ZR-75-30 cells utilizing lipid/perfluorubutane microbubbles (Targeson TS-108, 2.09 μm mean diameter) during sustained ultrasound (1 MHz, 0.45 MPa PNP, 0.45 MI, 10 cycles, 1 kHz PRF). Confocal microscopy and flow cytometry of PI staining were utilized to measure size of both cell types, and a cell size reduction of 61% was seen in most non-sonoporated cells, suggesting that sonoporation effected morphological changes even in the absence of PI uptake. Specifically, both cell membranes (stained with FM4-64) and cell nuclei (PI) were seen to shrink, with rounding of the cell present. Vacuolar-like accumulation of FM4-64 stained lipid in the cytoplasm was observed during confocal microscopy analysis, as well as an increase in granularity (side scatter increase) under flow cytometry, suggesting a disruption to lipid metabolism in the cells. BrdU proliferative stains showed a near-complete arrest of the sonoporated cell cycle after 6 h, with most cells stuck in the S-phase (DNA-replication before cell division). DNA synthesis was also shown to be significantly

slower in sonoporated ZR-75-30 cells (6.2 h for control vs. 15.2 h for sonoporated cells), and less so for HL-60 cells (8.7 h for control vs. 13.4 h for sonoporated cells).

Effects of sonoporation on the cellular cytoskeleton was investigated by Chen et al. (2014) in suspended ZR-75-30 human breast carcinoma cells with VEGFR-targeted lipid/perfluorobutane microbubbles (1-4 μm diameter) and single-shot ultrasound (1 MHz, 0.45 MPa PNP, 0.45 MI, 30 cycles; 47). Fluorescent videomicroscopy of cell staining with phalloidin-FITC for filamentous-actin (F-actin), and Alexa fluor 594 DNase I for globular-actin (G-actin) revealed F-actin rupture and disappearance 10 s after single-shot sonoporation, propagating from the porated region to the surrounding cytoskeleton. Image analysis of F-actin orientation showed that near-complete disassembly of the cytoskeleton progressed up to 60 min after sonoporation. Cells displaying higher PI intensity were observed to more rapidly lose F-actin coherence by up to 85% over those with less PI uptake (10x reduction in PI median fluorescence intensity [MFI]). G-actin was seen to increase in proportions commensurate with F-actin loss, with sonoporation resulting in 3.7 times as much G-actin fluorescence compared to F-actin. Unfortunately, however, characterization of cell viability was not conducted at the end of the observation period.

In 2014, Leung et al. (50) studied the lipid peroxidation in Jurkat cell populations sonoporated with lipid/perfluorobutane microbubbles (1-5 μm diameter, 10^6/mL) under sustained ultrasound (1 MHz, 0.45 MPa PNP, 0.45 MI, 10 cycles, 1 kHz PRF, 1 min total treatment). Flow cytometry indicated changes in cell morphology (delayed apoptosis and cell-cycle rhythm) within the first 24 h. PI staining of the cells displayed a decrease in cell viability 4 h after sonoporation, and relatively constant viability of about 65% after 24 h. Liquid chromatography and mass spectrometry were performed to identify lipid peroxidation products as well as other cell membrane products: arachidonic acid products [(S)-HETE, (S)-HETE-$_{d6,8}$], F_2-isoprostane

variants, arichadonic acid, eicosapentoic acid and cholesterol oxidation products (COPS). Reductions in (S)-HETE-8 and -11, both tumor cellular adhesion factors were observed (51). Lipid and cholesterol decreased post-sonoporation, indicating an increase in lipid metabolism. An increase in lipid peroxidation was observed and suggested to be attributable to a decrease in antioxidant activity. However, endogenous antioxidant (cathalase, glutathione and superoxide dismutase) concentrations showed an increase in cathalase and glutathione activity (+25%) and decrease in dismutase concentrations (-55%). The study indicated several similarities between non-oncogenic HETE, COPS and anti-cancer activity, suggesting a potential anti-tumor application for non-drug-loaded microbubbles. The effect of anti-proliferative activity on non-cancerous cells remains uncharacterized.

Recently, De Cock et al. (20) studied the sonoporation of plated human melanoma cells with lipid/perfluorobutane microbubbles (1.4 μm diameter, 8.9 x 10^8/mL) under sustained ultrasound (1 MHz, 100-500 kPa PNP, 2000 cycles, 125 Hz PRF, 5 s exposure). Flow cytometry was utilized to analyze FITC-dextran (4 kDa, 2 MDa) uptake in a population of cells after sonoporation, and uptake was characterized as acoustic intensity vs. low- and high-intensity uptake (MFI thresholds were not given). Fluorescence microscopy images of FITC-dextran uptake revealed three modes: endocytosis (point-fluorescence), diffusion (whole-cell fluorescence) and mixed (both modes). In general, low-acoustic intensity/large FITC-dextran treated cells were seen to exhibit low MFI and point fluorescence, which suggested endocytotic mechanisms of uptake, while high acoustic intensity/small FITC-dextran treated cells exhibited high MFI and full-cell fluorescence, suggesting membrane poration. Additional fluorescence microscopy of low-acoustic-intensity sonoporated cells indicated deformation, but no significant PI uptake in low-

MFI (point-fluorescent/FITC) cells, suggesting that the membrane had not been porated and that molecular uptake in these cells was mediated solely via endocytosis.

In summary, sonoporation causes transient cell-wide response in cells, which begin at the membrane transport level and progress to cytoskeletal and cell trauma pathways (Fig. 1.6). Some of these effects are beneficial towards drug delivery, such as the formation of membrane invaginations and activation of endocytotic pathways, while others slow cellular metabolism, retard the cell cycle at the S-phase and change cytoskeletal cohesion. These characterizations may allow us to counteract sonoporation-related cell death through Ca^{2+} supplementation, for example. Additionally, these investigations direct attention toward new areas of study, such as the role of endocytosis in non-traumatic sonoporative drug delivery and mechano-signaling pathways involved in halting cellular metabolism and triggering antioxidant release, among others.

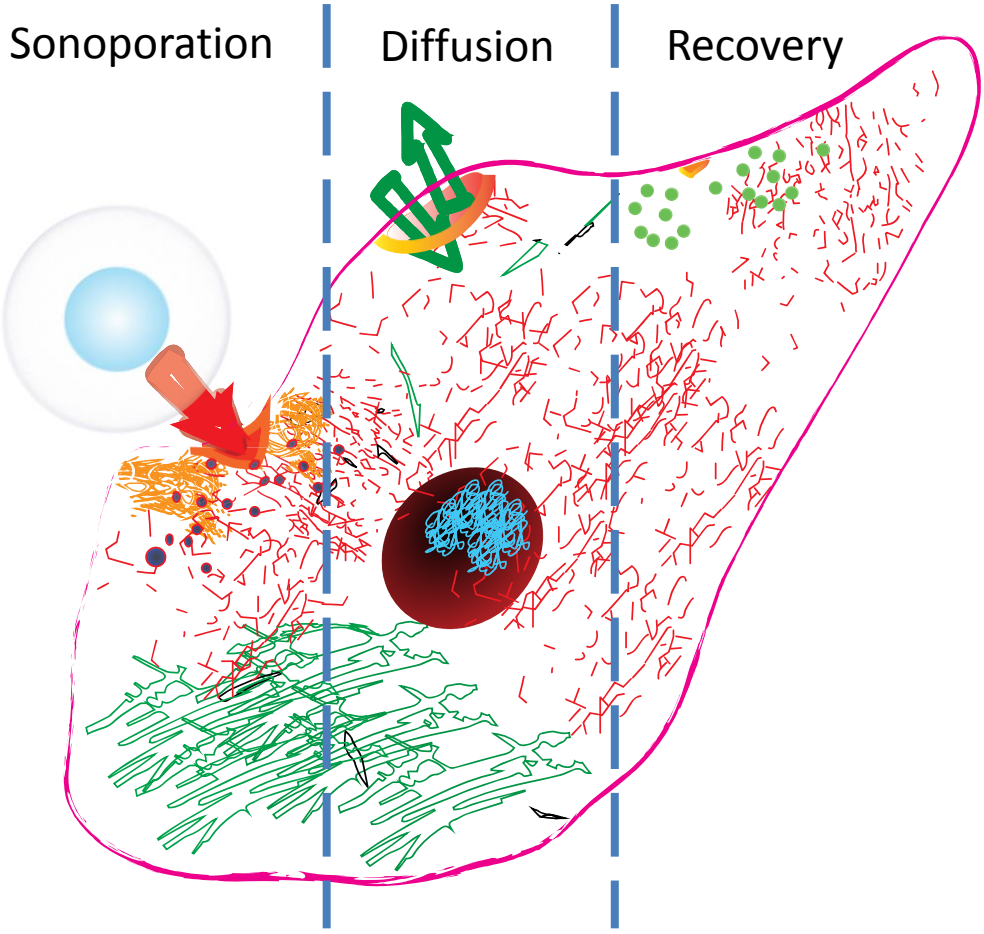

Figure 1.6. Bioeffects of sonoporation are characterized by membrane, cytoplasmic and nuclear changes of the cell. Sonoporation was seen to induce membrane pores (red arrow) and hypothesized to effect invaginated lipid-rafts (caveolae, orange) as well as trigger endocytosis (purple spheres; 20,46). Cytoskeletal f-actin (green) breakdown and large concentrations of g-actin were seen to propagate from the poration site, eventually replacing much of the f-actin in the cell (47). After sonoporation, molecular diffusion was observed to occurred, as well as protein-facilitated localized hyperpolarization (orange; 48), chromatin condensation in prophase (46) or cellular arrest in the S-phase of the cell cycle (indicated by the substitution of BrdU fluorescent molecules for thymidine during DNA synthesis, blue; 49). Simultaneously, calcium-mediated cellular recovery was shown to repair defects (orange; 38,39), over the course of several hours, with larger defects taking precedence (46). It has been hypothesized that the resealing process is facilitated by incorporation of lipid vesicules (green spheres; 39).

1.5.3. Experimental studies on multi-cell sonoporation

Multi-cell sonoporation extended the effects seen in single-cell sonoporation, applying prediction of acoustic intensity and microbubble behavior towards percent cells sonoporated and cell death in populations. These investigations characteristically studied microbubble destruction (as a population), cellular sonoporation and viability, as well as clonogenicity and other cellular behaviors as functions of microbubble concentration, ultrasonic amplitudes and inertial cavitation dose.

In 1999, Miller et al. (34) studied the sonoporation of suspended Chinese hamster ovary (CHO) cells with protein/air microbubbles (Albunex, 3.0-5.0 μm diameter, 10% dilution) under sustained ultrasound (1 to 7.15 MHz, 0.084-0.36 MPa PNP, $6.0x10^8$-$8.4x10^8$ cycles, 1 min total exposure) in rotating (60 RPM) vs. non-rotating flasks. Fluorescence and bright field optical microscopy were utilized to count FITC-dextran (580 kDa) permeabilized cells, as well as dead cells stained with trypan blue. Lower frequencies (1.0-2.25 MHz) were seen to increase sonoporation and cell death despite lower acoustic intensities (0.084-0.25 MPa, 0.056-0.25 MI), while higher frequencies (3.3-7.15 MHz) at all acoustic intensities (0.084-0.36 MPa, 0.031-0.18 MI) resulted in minimal cell permeabilization and cell death. The highest % cells sonoporated were effected with 2.25 MHz at 0.18 MPa (MI = 0.12; 5.8% sonoporated cells; 4.5% cell death), while the highest cell death was observed with 1 MHz, 0.14 MPa (MI = 0.14; 2.6% sonoporated cells; 8% cell death). Rotation of the flask under sonication at 2.25 MHz and 0.18 MPa resulted in a 20% increase in sonoporation over non-rotated samples; unfortunately, cell death was not reported for rotated samples. Additionally, adhesion of cells (colony formation on substrate) after sample sonication was seen to be reduced in sonoporated cells, indicating cell death (no PI was utilized in the study).

In 2004, Kamaev et al. (19) investigated the sonoporation of plated human prostate cancer cells (DU145) with Optison microbubbles under single-shot ultrasound (500 kHz, 0.6-3.0 MPa, 30,000 cycles) and sustained ultrasound (30,000 cycles, 1 Hz PRF). Coulter Counter measurements of microbubbles alone and during sonoporation indicated a PNP-dependent increase in microbubble destruction. An inverse linear relationship was observed between total ultrasound energy applied per area (0-110 J/cm^2), as calculated by $E = P^2 t/\rho$ (52), where P is rms pressure, t is time, ρ is water density and c is the speed of sound in water, and microbubble concentration at higher microbubble concentrations (1.7% dilution). Complete microbubble destruction was witnessed at lower concentrations (0.25% dilution), with the acoustic application of 13 J/cm^2. Flow cytometry was utilized to record calcein and PI uptake, which indicated a rapid drop in cell viability after 65% microbubble destruction under all ultrasonic conditions, while calcein uptake was seen to increase steadily with PNP. Interestingly, pre-sonicated/destroyed Optison microbubbles added to the sample resulted in approximately 50% the sonoporation efficiency of intact Optison microbubbles (1x10^7/mL) under 130 J/cm^2 and unspecified ultrasound parameters; the authors speculated that these effects were due to "secondary" microbubbles, which were undetectable by the Coulter Counter. As a whole, these results demonstrated that time-integrated metrics, such as total ultrasound energy, were potential indicators of sonoporationand cell viability.

In 2005, Karshafian et al. (32) studied the sonoporation of suspended KHT-C murine fibrosarcoma cells with protein/perfluoropropane (Optison, 2-4.5 μm diameter, 7% dilution) and lipid/perfluoropropane microbubbles (Definity, 1-10 μm diameter, 3.5% dilution) under sustained ultrasound (500 kHz, 125-570 kPa PNP, 8 cycles, 50 kHz PRF, 0-120 s total treatment duration). Flow cytometry was utilized to record the uptake of FITC-dextran (10 kDa to 2 MDa) and PI dilution. The results for 7% dilution of Optison showed that internalization of molecules larger

than 10 kDa was restricted. Comparison of the microbubble formulations revealed that Definity resulted in 20-40% greater FITC-dextran uptake over Optison at half the dilution (3.5%), although viability did not differ significantly.

In the same year, Larina et al. (36) studied the sonoporation of plated MCF7 (breast adenocarcinoma) cells with Optison microbubbles (1-20% dilution) under sustained ultrasound (1 vs. 3 MHz; unspecified PRF; 5, 10, 20% DC; 0.5-3 W/cm^2; 0.5-5 min total exposure). Flow cytometry was utilized to identify FITC-dextran (10 kDa) permeability. The highest sonoporation efficiency (72% of cells fluorescent) was achieved at the lower frequency (3 MHz) with the lowest microbubble concentration, while the lower frequency (1 MHz) resulted in peak efficiencies (55% of cells fluorescent) at the highest microbubble concentration. Sonoporation efficiency was seen to decrease as dilution was increased in high-frequency-treated samples. Generally, sonoporation efficiencies plateaued after 30 s total treatment duration, or at duty cycles greater than 5%. Plateaus in sonoporation efficiency occurred at higher acoustic intensities for 3 MHz vs. 1 MHz (1.5 W/cm^2 vs. 1.0 W/cm^2), suggesting that mechanical index was a more accurate indicator of applied cell stress. Interestingly, flow cytometry of EGFP transfected cells showed a reversal in trends compared to sonoporation, with 3 MHz insonations resulting in higher transfection efficiencies (32% peak efficiency) than 1 MHz treated samples (20% peak efficiency). Unfortunately, PNPs were not reported, and cell viability was not recorded concurrently with transfection.

In 2006, Lai et al. (28) studied the sonoporation of plated HeLa cells with Levovist lipid/SF_6 microbubbles (1.12 x 10^5/mL to 1.12 x 10^7/mL) under single-shot (1 MHz, 0.09-1.32 MPa PNP, 1-10 cycles) and sustained ultrasound (10 cycles, 50 Hz PRF, 0-30 s exposure). Passive cavitation analysis of microbubbles-only (no cells) samples (4.5 x 10^6/mL, 5 cycles, 1.32 MPa

PNP) revealed a ramp-up in inertial cavitation dose (ICD; defined as broadband response, or RMS amplitude between 9-11.5 MHz) 0.2 s after the start of sonication, peaking at 0.25 s and then disappearing after 0.6 s. Time-integrated ICD was observed to have a linear relationship with microbubble concentration and pulse duration, but ICD had a sigmoidal relationship with acoustic pressure. Regardless of the ultrasound parameters investigated, time-integrated ICD was seen to effect a linear increase in sonoporated cells and cell death.

In 2007, Mehier-Humbert et al. (37) investigated the sonoporation of suspended rat mammary carcinoma cells (10^6/mL) with lipid/perfluorobutane, lipid/air, triglyceride/perfluorobutane, triglyceride/air and polystyrene/air microbubbles (1.6-2.1 μm median diameters, $2x10^8$ to $2.6x10^9$ MB/mL) under sustained ultrasound (1.15 vs. 2.25 MHz, 0-809 kPa PNP, 2 ms pulse duration, 100 Hz PRF, 10 s total exposure). Coulter Counter measurements of microbubbles (12.5 x 10^6/mL) after cell sonoporation revealed a significant change in the microbubble size distribution 10 s after sonication, with 4-7 μm microbubbles showing the most noticeable change towards 1.5 μm and 9 μm. However, these size distributions were presented as percentages of total remaining microbubbles, as opposed to absolute concentrations; thus, the authors acknowledge the possibility of larger microbubbles surviving sonication, biasing results towards larger microbubbles, or the (initially) more numerous smaller microbubbles. In general, air microbubbles were seen to transfect fewer cells, while more rigid (triglyceride) microbubbles transfected more cells.

In 2008, Forbes et al. (31) studied the sonoporation of plated CHO cells (1.1 x 10^5 per 0.37 mL) with Optison (~8.8 x 10^8/mL) under sustained ultrasound (3.15 MHz, 0.12-3.5 MPa PNP, 20 ms pulse duration, 10 Hz PRF, 0-30 s total exposure). Flow cytometry was utilized to determine FITC-dextran (500 kDa) and PI uptake, as well as the optical scatter profiles of sonoporated cells.

Plotting PNP vs. % sonoporated cells resulted in a sigmoidal curve, revealing a sonopoation threshold at 0.5 MPa (0.3 MI), and a plateau at 1.8 MPa (1 MI). The results showed a linear relationship between PNP and dead cells up to 1.2 MPa PNP, at which point dead cells plateaued. Cell debris (a secondary indicator of cell death) also decreased slightly at PNP higher than 1.2 MPa, suggesting that the plateaus observed in % sonoporated and dead cells were unrelated to cell viability, and purely indicative of loss in sonoporative effect at higher PNP. The authors speculated that 1) microstreaming was necessary for sonoporation, 2) this microstreaming was occurring after 32 μs (one expansion/compression cycle at 3.15 MHz), and 3) the rapid collapse of microbubbles at PNP above 1.2 MPa (MI > 0.7) caused microbubble destruction after one pulse, thus reducing sonoporative effect on cells. The main problem with this explanation is that wall velocity also increases with acoustic intensity, even for a single expansion and collapse cycle.

In 2009, Karshafian et al. (53) investigated the sonoporation of suspended KHT-C fibrosarcoma cells (1.2 x 10^6/mL) with Definity microbubbles (3.3% dilution) under sustained ultrasound (500 kHz, 0-3.5 MPa PNP, 16 cycles, 0-3000 Hz PRF, 0-120 s total exposure). Flow cytometry was utilized to determine PI and FITC-dextran (70 kDa) uptake. MI, pulse duration and acoustic intensity positively correlated with FITC-dextran uptake and negatively correlated with PI staining. However, pulse duration and PRF were observed to have no significant effect, as long as pulse duration x PRF and acoustic intensity remained constant. The highest therapeutic indices (permeabilized cells/dead cells) were observed to be at low frequency (500 kHz), high PNP (570 kPa), short pulse duration (4 cycles), high PRF (3 kHz) and short exposure time (12 s). Maximum % cells sonoporated was achieved with identical parameters as above but with a longer pulse duration (6 cycles) and exposure time (120 s). Acoustic energy density, calculated by $E = I \cdot t$, where E is energy density, I is peak acoustic intensity and t is exposure time, demonstrated that

maximum therapeutic ratio occurred at an energy density of 1.1 J/cm^2 (MI = 0.55), with higher energy densities resulting in diminishing therapeutic ratios.

Additional studies by Karshafian et al. (33) studied sonoporation of KHT-C cells utilizing Optison (mean diameter = 1.1-3.3 μm) and Definity microbubbles (mean diameter = 3-4.5 μm) under sustained ultrasound (500 kHz, 570 kPa PNP, 0.8 MI, 16 cycles, 3 kHz PRF, 2 min total exposure). Microbubble concentration ranges were obtained from the manufacturer; multiplying these means to the dilution values presented, the estimated concentrations used were $8x10^6$-$1.6x10^9$/mL for Definity, and $4.4x10^5$-$8.6x10^7$/mL for Optison. As measured via flow cytometry, initial optimization of microbubble concentration revealed that maximum therapeutic index (TI; %sonoporated / %dead) was achieved at 3.3% dilution ($3.9x10^8$/mL) of Definity (TI = 0.9), and 6.67% dilution ($4.3x10^7$/mL) of Optison (TI = 0.55). Flow cytometry was utilized to determine viability (V) and clonogenic viability (Vc, PI uptake), as well as the sonoporation efficiency (% cells permeabilized to 70 kDa FITC-dextran) for both Optison and Definity. The results revealed that Optison ($4.3x10^7$/mL) demonstrated increased V_c over V, and Definity ($3.9x10^8$/mL) demonstrated increased V over V_c. Overall, Optison-treated samples were observed to result in more clonogenic and viable cells (than Definity-treated samples at 125-570 kPa (MI = 0.17-0.8)), and Definity microbubbles sonoporated more cells under the same ultrasound parameters. It was important to note that both the mean diameter and hypothetical concentration of Definity microbubbles was higher than Optison samples, which most likely resulted in increased % sonoporated cells and cell death. Similarly, it is possible that cells would proliferate in the more viable Optison-treated samples, in contrast with the reduced clonogenicity of Definity-treated samples.

1.6. Historical perspectives on BBB sonoporation

Sonoporation Parameter	Effect	*In vivo*
Inertial cavitation dose (ICD)	Increased permeabilization, cell death, microbubble destruction	(54,55)
Acoustic intensity	Increased mechanical index (MI), jetting, sonic cracking, pore size, cell death, transfection rates, PI diffusion, permeabilization, ICD, cellular debris, endocytosis	(56,57,54,58,55)
Acoustic frequency	Reduced MI, cell death	(59)
Pulse duration and pulse repetition frequency (PRF)	Increased pore size, permeabilization, cell death, transfection rates, duration of poration (recovery time), PI diffusion, microbubble translation, increased ultrasonic energy, ICD	(60,61)
Microbubble size	Increased microbubble persistence, permeabilization, cell death	(58,62)

Table 1.2. The study of BBB sonoporation parameters.

In 1956, Bakay et al. published one of the first studies on blood-brain-barrier (BBB) sonoporation utilizing ultrasound as the sole mediator of permeabilization (63). Although this new method was non-invasive and could spatially target treatment regions of deep within the body, resulting cell death and tissue damage limited translatability. It was almost 55 years before the first microbubble-assisted sonoporation of the BBB was conducted by Hynynen et al in 2001. These early microbubble studies demonstrated that BBB permeabilization could be achieved with much lower acoustic amplitudes than with ultrasound alone, greatly reducing the risk of neuronal and parenchymal tissue damage (56,57). The use of MRI was integral to early studies as a non-invasive means of analyzing contrast-agent propagation past the BBB, expediting characterization of the effects of several sonoporation parameters, namely acoustic settings (Table 1.2). A handful of preclinical studies have built upon these foundations to safely deliver chemotherapeutics and

nucleic acids to the brain. However, the study of sonoporation parameters has remained underdeveloped in comparison with translational studies, which we explore below.

The earliest characterization of BBB sonoporation parameters on small animals was conducted by Hynynen et al. (56), utilizing forward-thinking techniques such as MRI guidance, which were resurrected and saw widespread adoption over half a decade later. The brains of live rabbits were subject to multi-pulse sonications for 20 s with varying acoustic intensities and pulse lengths (0.2-11.5 W, 10-100 ms pulse length, 1.63 MHz center frequency, 1 Hz PRF) after a systemic injection of Optison (0.05 mL/kg, measured mean: 2.0-4.5 μm) and gadopentetate dimeglumine (GD), an MR contrast agent, used to measure change in signal intensity. Several details were addressed in this pioneering work, including the use of a focused ultrasound array to reduce the effects of skull and tissue attenuation, and improve localization of treatment regions. Using focused ultrasound, four brain regions were treated within the brain with differing acoustic amplitudes (1.0, 2.3, 3.3 and 4.7 MPa). MR thermometry revealed a peak temperature increase of 2.3 ± 0.8 to 4.8 ± 1.7°C. Hemotoxylin and eosin (H&E) staining was utilized to assess neuronal damage in the targeted areas. All amplitudes below 2 MPa resulted in no neuronal damage, with greater than 25% neuronal damage at 2.3 MPa, increasing to 60% neurons damaged at 4.7 MPa. Additionally, different time points of GD injection (2-7, 48 hr and 7d) were used to determine the duration in which the BBB remained permeabilized after sonoporation. Injection of contrast agents in the hours after sonoporation indicated steadily declining contrast intensity up to six hours after treatment, while at 24 and 48 hours, MR intensity changed very little with contrast agent injection. A key finding of this study can be drawn from the temperature increase and contrast agent data—Namely, the amount of temperature increase in the lowest-signal effective sonoporations were less than 0.3°C, suggesting that permeabilization occurred through mechanical

means, as opposed to tissue heating. Additionally, the authors noted that while specific extravasated molecular size was not studied, red blood cells could be found in the parenchyma, suggesting macromolecules could be transported through the BBB. Finally, acoustic amplitudes necessary for effective sonoporations incurred minimal cell death, demonstrating the safety of BBB sonoporation.

The next characterization of BBB sonoporation with microbubbles occurred six years later, in which Choi et al. (57) examined BBB extravasation of IP-injected gadolinium in mice, as a function of acoustic intensity utilizing Optison (400 µL/kg). Acoustic amplitudes were scaled for multi-pulse treatments from 0.8 to 2.7 MPa (1.5 MHz, 10 Hz pulse repetition frequency, 20 ms pulse length; five repetitions of 30s on, 30s off, 5 minute total treatment duration). A focused ultrasound transducer was used to target the left and right hippocampi, and beamform dispersion was examined in an *ex vivo* mouse skull model. Attenuation was found to be 18% through the left and right sagittal sutures, and minimal distortion of the signal was found at the experimental ultrasound settings. Accurate targeting of the left and right hippocampus was demonstrated at all ultrasound settings, and increasing acoustic amplitude was found to have a positive effect on MRI contrast agent propagation as measured by area per T1 scan plane. Additionally, gadolinium extravasation increased passively up to 100 min after sonoporation, which corroborated persistence-of-BBB-opening results obtained by Hynynen et al. and MacDannold et al. Finally, this study reinforced the value of FUS-mediated BBB sonoporation with microbubbles as a precise and non-invasive means of targeting brain regions. Subsequent studies by Choi et al. examined the effect of acoustic intensity (0.15, 0.30, 0.46 and 0.61) and size-isolated microbubbles (2- and 4-µm diameter) on FITC-dextran (3-kDa) extravasation in the hippocampi and thalami of mouse brains. Larger diameter microbubbles were found to more effectively open the BBB, especially at

low amplitudes (0.30 MPa), under which 2-μm microbubbles were ineffectual (58). Additionally, sonoporation of both the hippocampi and thalami resulted in differences in permeabilization efficiency, which suggested that treatment location was a significant factor in ultrasonic transmission to the targeted regions, even in the case of thin mouse skulls.

The first reported BBB-sonoporation characterization study in nonhuman primates was conducted by Tung et al. in 2011 (64). Three macaque monkeys were treated with 500 μL of Definity (1.1-3.3 μm) or 4-μm size-isolated lipid microbubbles, subject to multi-pulse sonications at 0.5 MHz center frequency and peak negative pressures ranging from 0.2-0.45 MPa. Pulse repetition frequency was varied as at 2 or 10 Hz, with 0.2 or 10 ms pulse durations. Although these conditions were varied over three monkeys, focus of this study was to reveal obstacles and considerations of utilizing sonoporation in larger animals. General trends were visible utilizing the MR contrast agent, gadodiomide, and MRI. Interestingly, the study showed that at some acoustic intensities which induced inertial cavitation (recorded with a passive cavitation detector), no permeabilization was visible. These occurrences coincided with the localization of microbubbles microbubbles in sinuses, which suggested that the cavitating microbubbles were not able to efficiently impinge upon the endothelium when stimulated in these relatively large fluid regions, as opposed to smaller diameter vessels. While the effects of acoustic intensity in smaller animals tested in previous studies were generally linear, the results in macaques showed that location played a significant role in sonoporation efficiency: 0.3 MPa treatments effected more permeabilization that 0.45 MPa sonications due to variation in location, suggesting that the skull and vascular structure at the treatment region is an important consideration for the translation of sonoporation to preclinical studies. Finally, the effect of microbubble size was examined between the smaller and polydisperse Definity microbubbles and the size-isolated 4-μm microbubbles. No

sonoporation was seen with the Definity microbubbles, which once again suggested that there was insufficient spatial overlap of the smaller microbubbles or possibly insufficient cavitation power. The clear implication of this study was that microbubble size may become an even more dominant parameter in human sonoporation trials.

A comprehensive study on the effects of acoustic parameters conducted by Choi et al. (2011) examined pulse repetition frequency, PRP and burst length in the context of permeabilization efficiency and cell damage (60). Pulse repetition frequency (6.25-100 kHz), PRP (0.13-0.51 MPa) were varied in Definity-injected mice. Pulse lengths of 2.3 μs and greater were organized in a distinct manner: resting periods were implemented via "burst repetition frequency" which repeated the pulses at low frequencies (0.1-10 Hz), effecting relatively long resting periods of 100 ms to 10 s between ultrasound transmission. Interestingly, very high burst repetition frequency was shown to reduce permeabilization in comparison to allowing for more recovery time—the mechanism remains elusive. As previous and subsequent studies showed, a sufficiently high PNP (0.51 MPa) was necessary to induce BBB permeabilization, although lower frequencies were cited to lower the PRP threshold for effective permeabiilzation (59). This is in line with the previously described concept of mechanical index, in which a lower frequency at the same acoustic intensity increases the mechanical index of the acoustic wave, thus increasing permeabilization. The authors also found that utilizing multiple pulses grouped in infrequent bursts retained permeabilization performance while reducing cell damage. This ideal resting period was determined to be somewhere between 0.1 and 1 s. More frequent bursts were found to *reduce* sonoporation, possibly due to hydrodynamic interference between microbubbles stimulated with each successive burst, or acoustic radiation force causing separation of subsequent microbubbles from the endothelium. Finally, a minimum total sonication time (total continuous acoustic output)

was required to induce permeabilization. The study also examined the permeabilization efficiency of three different sizes of FITC-dextran (3, 10, 70 kDa). Expectedly, the larger 70 kDa molecules showed less diffusion over smaller molecules. Interestingly, the larger drug molecules showed higher accumulation in punctate concentrated at the focal regions of treatment. Although not confirmed by the authors, this suggested that the 70 kDa molecules could escape into the parenchyma, the neural tissue limited its diffusion to a larger area. Finally, histology of the treated areas using TUNEL and H&E stains, as well as qualitative microscopy analysis of neurons, showed little cell damage at the tested settings. This suggested that safe and widespread permeabilization was possible, even with the larger (70 kDa) drug molecules. The primary implication of this study was that efficient permeabilization without detectable tissue damage can be achieved by allowing for sufficient recovery time between acoustic pulses during sonication.

A notable study on the effect of microbubble size on MR contrast agent (Omniscan™) was conducted by Samiotaki et al. in mouse models, utilizing 2-, 4- and 6-μm microbubbles (65). Although the primary aim of the study was to identify the rate at which the blood-brain barrier healed after sonoporation, several peripheral results provide compelling support for the implementation of size-isolated microbubbles to improve control over treatment. A 1.5 MHz focused ultrasound array was targeted to the area between the hippocampus and the thalamus on the right hemisphere for 60 s durations, 10 Hz pulse repetition frequency, 60 μs pulse lengths and at PRPs of 0.3-0.6 MPa. The results suggested that BBB healing occurred in the reverse of permeabilization, starting at the outer edges of the treatment region and moving towards the center. The reasoning behind this was that areas with more pores (such as the focal region) would close more slowly. However, an unexplored alternative interpretation was that denser vasculature in the focal region would result in a similar pattern, due to the greater number of latent microbubbles

present to create pores. Additionally, significantly less permeabilization was seen with the smaller 2-μm microbubbles as opposed to 4- and 6-μm microbubbles. Perhaps the most important finding of the study was that the time for BBB closing was dependent on microbubble size. Previous studies had shown that the time of BBB closing was approximately 24-48 hr with polydisperse commercial formulations. Sonoporating with larger microbubbles (4- and 6-μm) increased the duration of permeabilization to over five days. The authors point out that there are a handful of reasons for this discrepancy: the size of the 4- and 6-μm microbubbles used in Samiotaki's study are larger than previously used commercial formulations, creating larger pores which take longer to heal; the size of the model drug (Omniscan) is magnitudes smaller (570 Da) than previously utilized permeabilization markers such as Evans Blue (70 kDa), which may increase model drug transfer through the pores. Additionally, tissue damage (dark neurons, extravasated red blood cells) seen initially with short time-course studies was not seen, or greatly mitigated in the mice, suggesting that disrupted tissue may recover after a few days. In the context of size-isolated microbubbles, the implications of this study extend to the possibility of conducting a single permeabilizations and administering therapeutics over the course of several days without sonoporation; inversely, a low-energy, high power single sonoporation with small microbubbles may be utilized to avoid long-term BBB permeabilization.

In summary, sonoporation has been shown to be a safe method of BBB permeabilization, with several parameters affecting efficiency. Sonoporating at high acoustic intensities and larger microbubbles increased permeabilization, but resulted in higher cell death (54–58). Utilizing low burst-repetition frequencies, with millisecond-scale recovery times, reduced cell death and allowed for acoustic intensity and microbubble size to be increased, allowing for efficacious BBB permeabilization (65). Finally, skull thickness and relatively large vasculature structures was

shown to be a key consideration for translational research, as demonstrated by studies in nonhuman primate studies (64).

Chapter 2. Optimizing *in vitro* sonoporation with microbubble size

Sonoporation involves the transient permeabilization of cells with ultrasound-induced microbubble cavitation for intracellular drug and gene delivery. Despite favorable *in vitro* and *in vivo* trials and unprecedented levels of spatio-temporal control by focused ultrasound, improving transfection efficiency remains a key challenge. Previous reports have focused on the effects of changing ultrasound parameters on transfecting cells with polydisperse-sized microbubbles. In this study, we controlled neutral lipid microbubble size (2, 4 or 6-μm diameter) and concentration (10^6 to 10^8 mL^{-1}) while holding the ultrasound parameters constant (1 MHz, 2.0 W/cm^2, 10% duty cycle). The study used a novel exchangeable chamber system designed for high-throughput *in vitro* sonoporation and transfection of suspended cells by traveling waves emitted from a physiotherapy transducer. Poration, cell viability, and median fluorescence intensity were measured by flow cytometry and analyzed with a theoretical model of microbubble oscillation and translation. A clear trend was established between microbubble concentration and these sonoporation effects.Furthermore, larger microbubbles, which experience less relative expansion, were found to be more stable to insonation. However, the correlations between microbubble size and sonoporation effects were more complex owing to the interplay of inertial effects and residence time. Smaller (2-μm) bubbles were found to provide a higher fraction of sonoporated/transfected cells and fewer dead cells, but larger (6-μm) bubbles were found to producer greater intercellular delivery per cell. Mixing in the sonication chamber reduces the effects of translation induced by the primary Bjerknes force, leading to a higher proportion of affected cells. Overall, these results show the importance of controlling microbubble size to optimize the efficiency and reproducibility of *in vitro* sonoporation.

2.1. Introduction

While viral therapeutics promise a highly efficient means of gene delivery, safety concerns have pushed interest towards less efficient non-viral therapeutics. Previous *in vitro* studies have demonstrated that porative transfection methods such as microbubble-assisted sonoporation (MAS) offer improved transfection rates over other non-viral transfection methods in difficult-to-transfect cell types, as well as the potential for improved clinical translatability for *in vivo* gene therapy (66). MAS employs the acoustically responsive nature of microbubbles, also known as ultrasound contrast agents (UCAs); small (1-10 μm diameter) gas cores stabilized by a surfactant shell, to deliver suspended and shell-adsorbed drugs to cells and tissue upon application of ultrasound. MAS offers distinct advantages over other non-viral transfection methods, namely inherent biocompatibility and spatio-temporal control over drug delivery. However, like many non-viral transfection methods, improving the efficiency of MAS remains a challenge, with previous studies indicating high cell mortality as a limiting factor (67). Thus, understanding the mechanistic basis of cellular permeabilization during sonoporation, in addition to developing means of control over both the rate and magnitude of sonoporation, are crucial to improving MAS efficiency and viability.

Two sometimes overlapping approaches towards altering microbubble behavior and improving MAS have prevailed: (1) modifying the chemical properties of the microbubble shell or (2) adjusting the acoustic driving parameters to identify optimum settings for sonoporation. Regarding the former, prior studies have characterized the effect of cationic lipid shells, which were hypothesized to improve association of negatively-charged nucleic acids and target cells to microbubbles, improving payload delivery (68,69). An extreme version of cationic microbubble-modification was demonstrated by Borden et al., in which up to five alternating layers of cationic

polymer and DNA were added to the microbubble shell, increasing nucleic acid payload over ten-fold (70). However, these microbubbles produced very little *in vitro* cell transfection, indicating that the DNA molecules must be available (uncomplexed) for cell internalization. Several studies have shown that cationic lipid microbubbles improve *in vivo* transfection (69,71–73), but the advantage is diminished at higher injected doses of DNA (71,72), indicating the counteracting roles of complexation on localized delivery and bioavailability. Interestingly, an early study by Karshafian et al. demonstrated that even drastic differences in sonoporation between shell chemistries were overshadowed by differences in size or concentration (32). Specifically, commercially available microbubble formulations, such as lipid-based Definity® and albumin-based Optison™, showed that up to twice the sonoporation rates were obtained with the more concentrated Definity® formulation, but that efficiency-per-microbubble favored the large-diameter Optison™.

In an effort to improve sonoporation control and efficiency, several studies have investigated the effect of acoustic properties (53,74,75). While earlier observations generalized the effect of acoustic driving intensity as an increase in sonoporation and a reduction in cell viability, valuable insight was gathered on the need to identify a "threshold" of sonoporation (76). Further attempts to identify this threshold saw two parameters changed: (1) ultrasound pulse length and (2) pulse repetition frequency (PRF). A detailed series of experiments by Chen et al. on the hemolytic potential of microbubbles showed that increasing both the pulse length and PRF resulted in increased inertial cavitation, which was suggested to be the cause of hemolysis (77,78). The postulation that inertial cavitation causes cellular sonoporation was expanded upon by multi-parameter studies conducted by Fan et al., which linked microbubble-cell proximity and inertial cavitation to efficient transfection (45). A separate multi-parameter study by Karshafian et al.

showed that cell permeability increased and viability decreased with increasing peak negative pressure and decreasing pulse center frequency (53), both of which promote inertial cavitation. Interestingly, Karshafian et al. also showed that cell permeability and viability did not correlate with microbubble disruption.

The effect of microbubble concentration was only recently investigated, which revealed similar trends to those seen with higher acoustic driving intensities. Higher concentrations improved permeability to fluorescent markers up to a point, after which cellular viability started to diminish (33). Interestingly, bubble-bubble interactions have also been shown to play an important role in sonoporation (79).

Prior investigations have only glanced at the question of microbubble size and its effect on cellular sonoporation (32,44). However, investigations utilizing size-isolated microbubbles have revealed that both *in vivo* microbubble persistence (80,81) and tissue permeabilization (58) are enhanced with increasing microbubble size. In this study, we hypothesized that microbubble size also has a significant effect on *in vitro* cell sonoporation and transfection. To test this hypothesis, we employed centrifugally size-isolated microbubbles and a sealed, sterile cartridge with acoustically transparent windows. The cartridge bracket allowed for easy exchange of the sonoporation sample with minimal deviation between trials. Sonoporation and transfection effects were then measured by flow cytometry.

2.2. Materials

1,2-distearoyl-*sn*-glycero-3-phosphocholine (DSPC) and 1,2-distearoyl-sn-glycero-3-phosphoethanolamine-N-[(polyethylene glycol)-2000] (DSPE-PEG_{2000}) lipid powder was

obtained from Avanti Polar Lipids (Alabaster, AL, USA) for microbubble preparation. Perfluorobutane (PFB) gas was obtained from FluoroMed (Round Rock, TX, USA). HeLa cells (ATCC, Manassas, VA, USA) were cultured in DMEM solution with 10% FBS (Fisher Scientific, Hampton, NH) and 70 kDa FITC-dextran was utilized for sonoporation assays (Sigma-Aldrich, St. Louis, MO, USA). pEGFP-C3 plasmid (Clontech, Mountain View, CA, USA) was utilized for transfection assays, and dead cells were stained with ethidium homodimer-1 (Invitrogen, Grand Island, NY, USA).

2.3. Experimental Methods

2.3.1. Microbubble preparation

Lipid-encapsulated perfluorocarbon microbubbles were generated via sonication of DSPC and DSPE-PEG_{2000} lipid suspension (Avanti Polar Lipids, Alabaster, AL, USA) at a concentration of 2 mg/mL and molar ratio of 9:1 in 150 mM NaCl pH 7.4 phosphate buffered saline (PBS) solution, in the presence of perfluorobutane gas (Fluoromed, Round Rock, TX, USA). Microbubbles were separated based on size using differential centrifugation, and microbubble populations with median diameters of 2, 4 and 6 μm were isolated and stored in hermetically sealed serum vials (81). Samples were sized using an Accusizer (PSS Nicomp, Santa Barbara, CA, USA) and a Multisizer 3® (Beckman Coulter, Brea, CA, USA).

2.3.2. Design and fabrication of the in vitro sonoporation system

The sonoporation assembly (Fig. 2.1) was designed and constructed as a temperature-resistant, water-tight enclosure constructed from acrylic and polypropylene, modified to accept a 1" diameter ultrasound transducer from a Dynatron® 125 (Dynatronics, Salt Lake City, UT, USA). The transducer was characterized by a needle hydrophone (HNC-0200, Onda Corp., Sunnyvale, CA) and at a setting of 2.0 W/cm^2, shown to provide ultrasound bursts at 1.0 MHz, 0.53 ± 0.03 MPa, 10% duty cycle (10 cycles per pulse) and 100 Hz pulse repetition frequency (PRF; Fig. 2.2). A submersible polypropylene cartridge was modified with acoustically transparent polystyrene windows and sealed with a polyurethane serum vial cap to contain an internal fluid volume of 200 µL. The cartridge volume was designed with a reverse-bevel along its circumference to minimize acoustic reflections from the window edge into the sample. Window attenuation, as well as waveform distortion, was inspected along the cartridge area at a distance of 5 mm from the trailing acoustic window. The polypropylene bracket fixing the cartridge position in the chamber was designed to submerge in water up to 40 °C and allow for the exchange of cartridges with no variation in cartridge position relative to the transducer. Each cartridge was tested for acoustic transparency with a needle hydrophone (HNC-0200; Onda Corporation, Sunnyvale, CA, USA) to achieve less than 5% signal attenuation. De-ionized and de-gassed water held at a temperature of 37°C was used as an acoustic medium between the transducer and cartridge in the sonoporation assembly.

A second cartridge was designed and fabricated to accommodate a 2-mm long stir bar rotating at 800-1000 RPM. The mixing cartridge kept the sample homogenous and allowed study of the effect of counteracting cell/microbubble separation due to ultrasound radiation forces and buoyancy (Fig. 2.9d). The stir-bar equipped cartridge retained the 200 µL volume of the non-

mixing cartridge as well as the anti-reflection bevel, but was designed with a shorter and wider profile to accommodate the width of the stir bar.

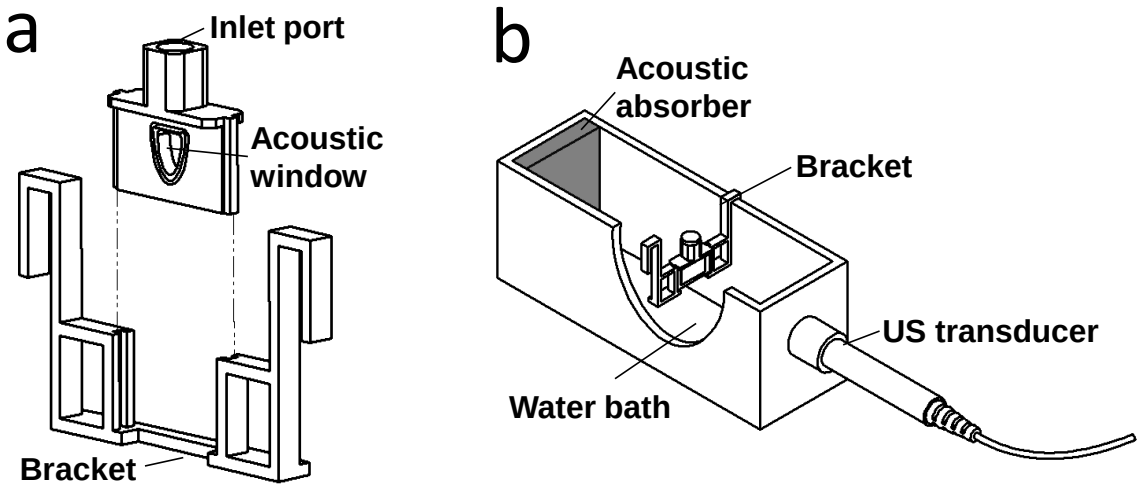

Figure 2.1. The *in vitro* sonoporation apparatus utilizes an immersed, sealed and ethanol-sterilized treatment cartridge, placed a fixed distance from the ultrasonic transducer. a) Microbubbles and cells were co-injected into the chamber of a sonoporation cartridge, which was mounted in a cartridge bracket. The chamber volume was 0.2 mL, with a total transverse internal width of 2.5 mm. Placement of acoustically transparent polystyrene windows (0.1-mm thick, ~2% reduction in PNP) on the front and back of the chamber allowed ultrasound to travel through with minimal reflections. b) The sonication cartridge bracket was mounted in a fixed distance of 40 mm from the ultrasound transducer, and a polypropylene foam acoustic damper was placed at the opposite end of the chamber to minimize reflections.

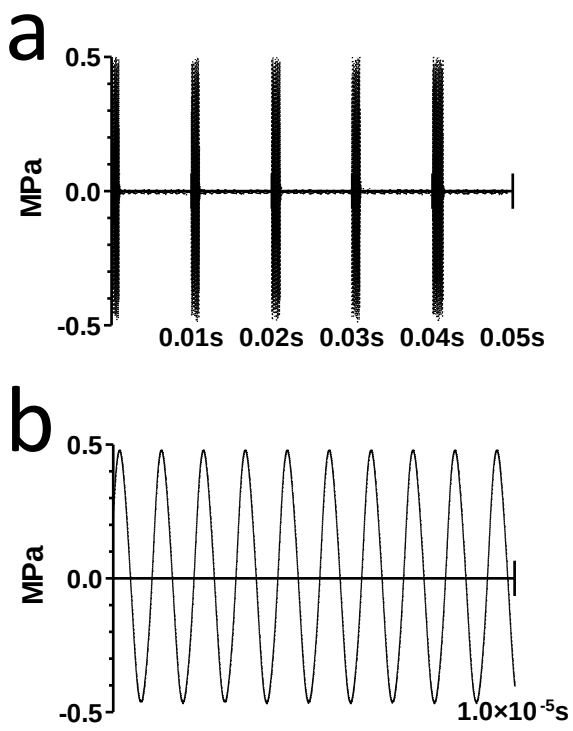

Figure 2.2. The acoustic driving pulse utilized in all experiments was characterized utilizing a membrane-type needle hydrophone, taken in a) long and b) short time increments. Hydrophone measurements showed a 1-ms pulse length, 100-Hz PRF, 1.0-MHz center frequency and 0.53 ± 0.03 MPa PNP at a transducer setting of 2.0 W/cm^2, which was used in all sonoporation and transfection experiments.

2.3.3. Microbubble survival during exposure to ultrasound

Microbubble survival was tested under sonoporation conditions (37°C, 2-min ultrasound exposure time), with experimental groups of 2, 4 and 6-µm diameter microbubbles at an initial concentration of 10^8/mL. The microbubble suspensions were insonified at 1.0 MHz, 0.53 ± 0.03 MPa PNP, 10% duty cycle, 100 Hz PRF for 2 min, with 2-µL aliquots taken at 5, 30 and 120 seconds. Each aliquot was analyzed for concentration and size.

2.3.4. Cell culture and handling

HeLa cells were procured from ATCC (Cat no. CCL-2) and thawed from 10% DMSO solution. Thawed cells were cultured at 37°C, 5% CO_2 in DMEM with 10% fetal bovine serum supplement (03-600-511, Fisher Scientific, Hampton, NH, USA) and 1% penicillin/streptomycin (P0781, Sigma-Aldrich, St. Louis, MO) and passaged until stable growth patterns were observed. Cells were harvested at 70% confluence for use in membrane permeabilization and transfection experiments. Sonoporation cell concentrations were held constant at $5x10^6$ cells per mL for each experimental group.

2.3.5. Cellular sonoporation assay

FITC-dextran (70 kDa, 0.77 mg/mL, Sigma-Aldrich, St. Louis, MO, USA), a long-chain sugar with a fluoroscein isothiocyanate moiety, was found to be a suitable indicator of cell permeabilization in previous sonoporation studies with 2-µL lipid-shelled microbubbles, as well as an indicator of drug loading (53,82,83). 20 µL of FITC-dextran (7.7 mg/mL) was added to 180 µL of microbubble/cell suspension. Four microbubble concentrations (10^6, 10^7, $5x10^7$, 10^8/mL) were tested for each group size (2, 4 and 6 µm diameter). Higher concentrations were avoided due

to their high viscosity, particularly for the larger size groups. Verification of microbubble and cell concentrations was conducted within ten minutes of sonication; in-cartridge concentration of microbubbles was verified to be within 5% of the target concentration, while cell concentration was verified by cytometric measurement to be $5x10^6 \pm 2.5x10^5$ cells/mL before sonication. Cell/microbubble/FITC-dextran suspensions were then subjected to ultrasound (1 MHz, 2.0 W/cm^2, 10% duty cycle, 100 Hz PRF) in the sonoporation system. Treated cell samples were removed from the cartridges and washed three times at 500 RCF in 15-mL cell media tubes. Anti-fluorescein (A-889, Invitrogen, Grand Island, NY, USA) was added to quench residual fluorescence on exterior cell surfaces after the third wash to eliminate FITC fluorescence from non-permeabilized cells. Additionally, ethidium homodimer-1 (E-1169, Invitrogen, NY, USA) was applied at 0.2 M quantity to each sample to identify damaged (non-viable) cells and minimize false positives from auto-fluorescence. Fluorescence microscopy (Olympus IX71) was conducted to confirm internalization of FITC-dextran in sonoporated (permeabilized and viable) cells. A flow cytometer (Accuri C5, Ann Arbor, MI, USA) was used to analyze populations of treated cells. Cells were gated in the forward-vs-side scatter plot as a relatively highly scattering group that was easily distinguishable from the serpentine pattern of microbubbles (84). Once gated in the scatter plot, cells were analyzed for fluorescence by plotting FL1 (520 nm) vs FL2 (585 nm) and gating for dead cells (ethidium homodimer-1 (FL2)), sonoporated cells (those permeabilized with FITC-dextran (FL1) but not ethidium homodimer-1 (FL2)) and unaffected cells (low FL1 and FL2 intensities). Sonoporated cells were analyzed for both percentage of viable cells that were sonoporated and median fluorescence intensity per sonoporated cell.

2.3.6. pDNA transfection assay

Transfection assays were conducted with pEGFP-C3 plasmid (Clontech, Mountain View, CA, USA) at a constant concentration of 25 µg/mL. EGFP-plasmid quality was verified by Southern blot, and pDNA concentration was verified before trials by measuring 260/280 nm (ex/em) absorbance of samples. Plasmid was added to cell suspensions with a range of microbubble concentrations (10^6, 10^7, $5x10^7$, 10^8/mL) for each microbubble size (2, 4 and 6 µm diameter), and the cell/microbubble/pDNA mixtures were sonoporated at identical ultrasound settings used in the sonoporation assay. After sonication, cells were placed in six-well polystyrene plates with 2 mL of additional media and incubated for 24 hours. After incubation, non-viable cells were stained with ethidium homodimer-1, and flow cytometry was conducted on the cell samples to determine viability, the transfected fraction of viable cells and the median fluorescence intensity of transfected cells for each experimental group.

2.3.7. Comparison of transfection efficiency vs. electroporation

Plasmid EGFP-C3 (Clontech, Mountain View, CA, USA) was used for transfection assays of HeLa cells in suspension (ATCC, Manassas, VA, USA). Electroporation was conducted with an IBI Gene Zapper 450/2200 (IBI, New Haven, CT) on cells in suspension (1-3 x 10^6 cells/200 ul with 5 ug DNA) at a voltage of 0.22 kV and capacitance at 500 µF. Microbubble-treated samples were sonoporated with 2- and 6-µm microbubbles at 10^8 MB/mL in a 200 µL volume with 5 µg of DNA for 2 minutes at 2 W/cm^2, 10% DC with a Dynatron® 125 (Dynatronics, Salt Lake City, Utah). HeLa cells from both electroporation and sonoporation were cultured for 24 hr before the addition of ethidium homodimer-1 (Invitrogen, NY, USA) to stain for dead cells. Flow-cytometric analysis was conducted to determine EGFP-expressing and dead cells.

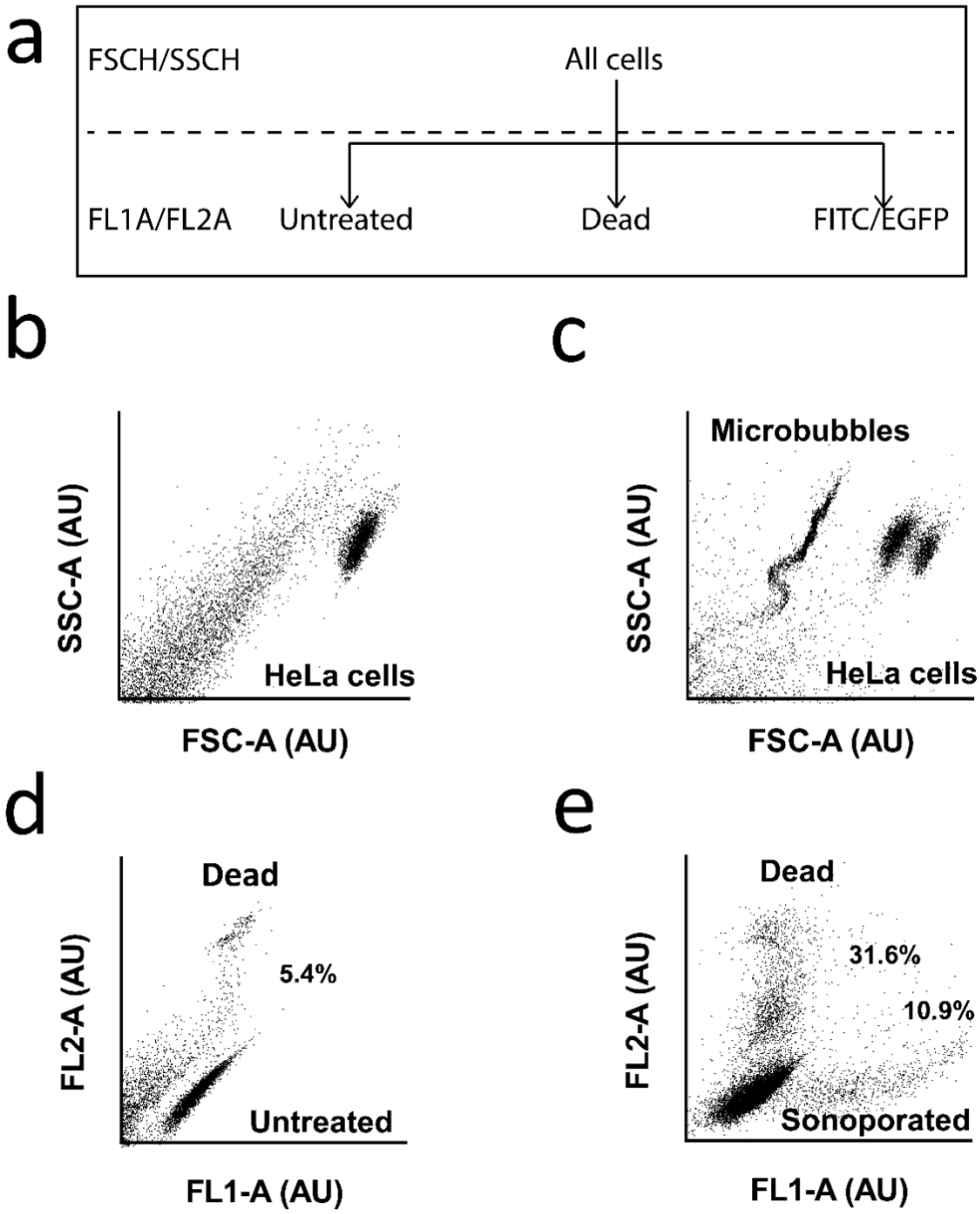

Figure 2.3. Flow cytometric analysis of sonoporated cells. (a) Gating scheme and relevant channels for analysis of sonoporated, dead and untreated cells. (b) Forward (FSC-A) versus side (SSC-A) scatter plot of HeLa cells treated with FITC-dextran and ultrasound, but not microbubbles. (c) Scatter plot of HeLa cells sonoporated with ultrasound, FITC-dextran and 6-µm diameter bubbles at $5x10^7$/mL concentration. Note that the HeLa cells were easily distinguished from the serpentine pattern of the microbubbles. Note also the presence of a second scatter group of HeLa cells with reduced forward scatter; this second group contained mostly dead cells. (d) Fluorescence plot (FL1 = 520 nm; FL2 = 585 nm) of the control cells from the gate in panel (b) showing regions of live (non-sonoporated) and dead cells. (e) Fluorescence plot of the treated cells from the gate in panel (c) showing regions of dead, non-sonoporated and sonoporated cells (high FL1 due to FITC-dextran internalization).

2.3.8. Flow cytometric analysis

The determination of optimal flow rates, cut-offs, compensation and gating were performed through the Accuri C5 and C6 software. The forward-scatter-H cutoff value for measured samples was $8x10^5$, with the upper limit being $10^{7.2}$. Gating was conducted as described in Supplementary Figure 4. Compensation of FL1-A (520 nm) and FL2-A (560nm) were conducted with both FITC dextran and EGFP in relation to ethidium homodimer-1 as detailed by the CU Denver Cancer Center flow cytometry core. A slight undercompensation on FL2-FL1 (<0.2%) was noted but signals from the live-treated and dead cell groups were considered to be strong and distinct when compared to the controls, with minimal gate contamination from autofluorescent cells (Fig. 2.3).

2.3.9. Data analysis

Comparison of sonoporation and transfection results was conducted through unpaired t-tests between size groups in GraphPad Prism software (La Jolla, CA, USA). Significant differences were determined for two sample groups if the p-value was found to be smaller than 0.05, $n \geq 3$.

2.3.10. Radial dynamics calculations

Simulations were conducted via MATLAB (Mathworks, Natick, MA, USA). The modeling of the radial dynamics of a lipid shell microbubble is performed through implementation of the model by Marmottant et al. (2005), which considers a variable surface tension in three linear regimes, dependent on bubble area (13). This model uses only three parameters: the buckling bubble area, $A_{buckling}$, below which the surface buckles; an elastic modulus, χ, which dictates the

dynamics in the elastic regime; and a break-up surface tension, $\gamma_{break-up}$, above which the surface tension is dictated by the surrounding liquid. Below, modeling of the three regimes is discussed.

In the buckled regime, it is assumed that surface tension is negligible ($\gamma = 0$), consistent with monolayered lipid shells. The buckling area is dependent on the number and size of lipid molecules at the interface. For the simulations presented in this report, it is assumed the bubble begins in a quiescent state at a specified initial radius, R_0, with an intact lipid shell. This leads to a buckling area $A_{buckling} = \pi {R_0}^2$, or equivalently a buckling radius $R_{buckling} = R_0$, below which surface tension is considered negligible.

The next regime considered is the elastic regime where the surface tension is dictated by $\gamma = \chi(\frac{A}{A_{buckling}} - 1)$. This case operates between two limits: $A_{buckling}$ for the lower limit and the break-up area, $A_{break-up}$, for the upper limit. For this narrow range of radii, surface tension is dictated by the shell elastic modulus, χ, and increases with surface area. Again, this surface tension is only valid between the two limits, for which the lipid shell is neither buckled nor broken. It is important to note that after a period of buckling, a rigid lipid shell can still be constructed, i.e., the elastic regime still dictates dynamics after radial growth above $R_{buckling}$, even after shell buckling.

The final regime is one in which the bubble radius has grown beyond the break-up radius, $R_{break-up}$, where $A_{break-up} = \pi R_{break-up}^2$, and has fractured. After the shell is broken up, the surface tension drops and the bubble is considered to have an exposed gas interface with lipid shell islands. In this scenario, surface tension is dictated by the gas-liquid interface and therefore by the surface tension of the exterior liquid, assumed to be water in this case ($\gamma = \gamma_{water}$). After break-up has occurred, the lipid shell reconstructs when the radius decreases below the ruptured radius,

$R_{ruptured}$, where $R_{ruptured} < R_{break-up}$, and operates in the linear elastic regime as before. However, upon subsequent expansions after break-up, the ruptured radius, not the break-up radius, sets the upper limit of the elastic regime, above which the surrounding liquid dictates surface tension. Surface tension expressions for each regime are presented below:

$$\gamma(R) = \begin{cases} 0 \; if \; R \le R_{buckling} \\ \chi\left(\dfrac{R^2}{R^2{}_{buckling}} - 1\right) if \; R_{buckling} \le R_{break-up} \\ \gamma_{water} \; if \; ruptured \; and \; R \ge R_{ruptured} \end{cases} \tag{2.1}$$

The radial limits above are determined as:

$$R_{buckling} = R_0$$

$$R_{break-up} = R_{buckling}\left(1 + \frac{\gamma_{break-up}}{\chi}\right)^{1/2} \tag{2.2}$$

$$R_{ruptured} = R_{buckling}\left(1 + \frac{\gamma_{water}}{\chi}\right)^{1/2}$$

The internal gas pressure, $P_g(t)$, of the lipid shelled bubble is determined by

$$P_g(t) = P_l(t) + \frac{2\gamma(R)}{R} + 4\mu\frac{\dot{R}}{R} + 4\kappa_S\frac{\dot{R}}{R^2}, \tag{2.3}$$

where $P_l(t)$ is the liquid pressure at the bubble surface, μ is the liquid viscosity, and the overdot $\dot{R}$ denotes a derivative with respect to time, *t*. The first term on the right is the liquid pressure, the second term is the surface tension, the third term arises from viscosity in the liquid, and the fourth term arises from friction in the shell. The constant κ_s is the surface dilation viscosity of the monolayer and is derived from $\kappa_S = 3 \in \mu_{lipid}$, where $\in$ is the shell thickness and μ_{lipid} is the bulk lipid viscosity. For the simulations presented here, the value for γ_{water} is set to 0.0728 N/m and the values for κ_S, χ, and $\gamma_{break-up}$ are set equal to 7.2×10^{-9} N-s/m, 1 N/m, and 0.13 N/m, respectively, based on the values reported in Marmottant et al. (2005) for the contrast agent BR14.

The radial dynamics of the microbubble are determined by combining the Rayleigh-Plesset equation with the polytropic gas law and the boundary condition (4). This process yields the second-order ordinary differential equation

$$\rho_l\left(R\ddot{R} + \frac{3}{2}\dot{R}^2\right) = \left[P_0 + \frac{2\gamma(R_0)}{R_0}\right]\left(\frac{R}{R_0}\right)^{-3\kappa}\left(1 - \frac{3\kappa}{c}\dot{R}\right) - P_0 - \frac{2\gamma(R)}{R} - \frac{4\mu\dot{R}}{R} - \frac{4\kappa_S\dot{R}}{R^2} - P_{ac}(t). \tag{2.4}$$

where ρ_l is the liquid density, P_0 is the hydrostatic pressure, κ is the polytropic gas constant, c is the speed of sound in the liquid, and $P_{ac}(t)$ is the acoustic forcing pressure. This equation is identical to that of a free bubble, modified only by a variable surface tension and the second to last term on the right side that accounts for shell friction. The acoustic forcing term is modeled as a sinusoid according to $P_{ac}(t) = P_a \sin(\omega t)$, where P_a is the acoustic pressure amplitude and $\omega = 2\pi f$ is the angular frequency corresponding to the transducer frequency, f. Associated values for P_a and ω are 530 kPa and 1 MHz, respectively. Simulations were conducted with water as the

surrounding liquid with properties of ρ_l = 1000 kg/m^3, μ = 0.001 Pa-s, C = 1485 m/s, and κ = 1.07 for the interior gas. The speed of sound was assumed to be that of water at room temperature, and the polytropic gas constant was chosen for a BR14 contrast agent filled with C4F10 gas in agreement with the aforementioned shell properties (85). Simulations were conducted for bubbles beginning at a quiescent state with initial radii of 1-µm, 2-µm, and 3-µm, corresponding to 2-µm, 4-µm, and 6-µm diameter bubbles, respectively. The radius and radial velocity are nondimensionalized according to,

$$R^* = \frac{R}{R_0} \qquad \dot{R}^* = \frac{\dot{R}}{R_0 \omega}, \tag{2.5}$$

where $\dot{R}$ is the radial velocity and the asterisk (*) denotes a dimensionless quantity.

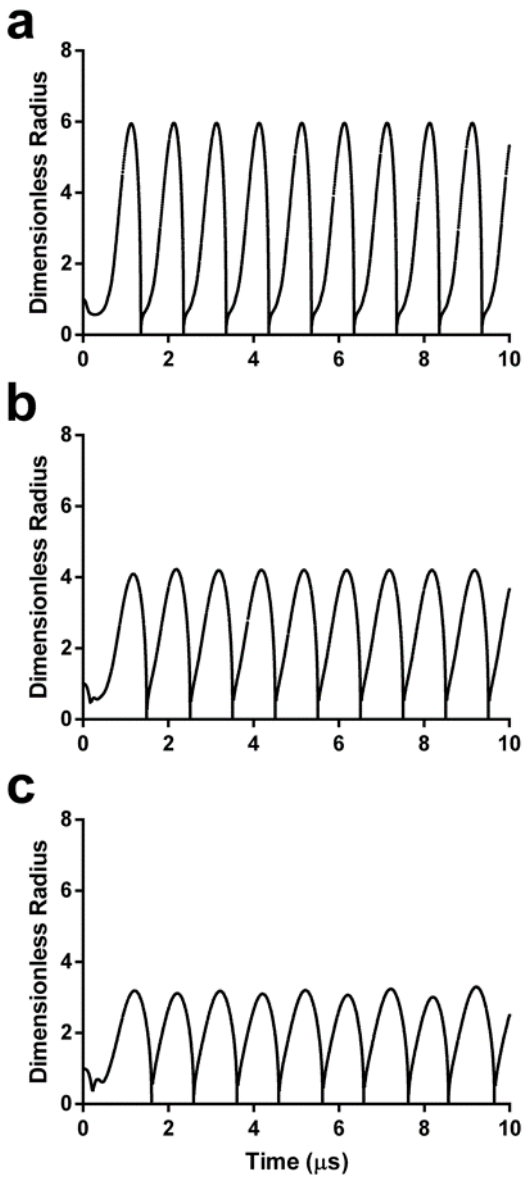

Figure 2.4. Dimensionless radius-time curves during acoustic forcing for initial microbubble diameters of 2 μm (a), 4 μm (b) and 6 μm (c).

2.3.11. Radiation force translation calculations

In addition to the radial dynamics, microbubble translation was computed using the model of Reddy and Szeri (86). This model is an expansion of models constructed by Magnaudet and Legendre who developed detailed expressions for the hydrodynamic force acting on a bubble of changing radius surrounded by an incompressible fluid (87). Reddy and Szeri concluded there are two distinct cases, one for $\mathrm{Re} \ll 1$ and one for $\mathrm{Re} \ll 1$. The minimum time-averaged Reynolds number computed for the cases in this report are around 44; therefore, we implement the model for the case $\mathrm{Re} \ll 1$. The translation model begins with the expression for hydrodynamic force on a microbubble, F_H, in a high Reynolds number scenario given by

$$F_H(t) = 12\pi\mu R(t)U(t) + \frac{2\pi}{3}\rho\frac{d}{dt}\left(R(t)^3 U(t)\right) + \frac{4\pi}{3}\rho R(t)^3 \dot{U}_a(t), \tag{2.6}$$

where $U(t)$ is the liquid velocity in the far field relative to the bubble and the absolute velocity of the liquid (relative to an inertial frame) is $U_a(t) = \dot{X}(t) + U(t)$, where $X(t)$ is the position of the bubble in an inertial frame. The terms on the right-hand side of the above equation represent from left to right a Stokes-like drag term, an added mass term, and an inertial force due to the fact that the expression for drag was derived in a noninertial frame. Next, a balance of fluid momentum in the far field yields

$$\rho\dot{U}_a \approx -\nabla P_\infty, \tag{2.7}$$

where $P_\infty(X,t) = P_0 + P_a \sin\left(2\pi X(t)/\lambda - \omega t\right)$ is the far-field pressure and λ is the acoustic wavelength. This equation enables the final term of $F_H(t)$ to be written as the primary Bjerknes force, $-V\nabla P_\infty$. Here it is assumed that the mass of the gas within the bubble is negligible, and

when the bubble is strongly forced the appropriate limit is $U\,\mathrm{Re} >> 1$. The equation governing microbubble translation is then given by

$$\frac{2\pi}{3}\rho\frac{d}{dt}\left(R(t)^3\left(U_a(t)-\dot{X}(t)\right)\right)=\frac{4\pi}{3}R(t)^3\nabla P_\infty\left(X(t),t\right)-12\pi\mu R(t)\left(U_a(t)-\dot{X}(t)\right). \qquad (2.8)$$

The Marmottant model for radial dynamics was coupled to the above translation model and simulations were conducted using the ordinary differential equation solver *ode45* in MATLAB® to solve for the bubble radius, $R(t)$, and position, $X(t)$, simultaneously.

2.4. Results

MB size class		Mean (µm)*	Median (µm)	Mode (µm)	Half-life
2-µm	Accusizer	1.53 ± 0.16	1.44 ± 0.06	1.70 ± 0.19	0.7 s
	Multisizer	1.80 ± 0.02	1.73 ± 0.03	1.74 ± 0.12	
4-µm	Accusizer	3.50 ± 0.25	3.67 ± 0.15	4.20 ± 0.20	1.7 s
	Multisizer	4.07 ± 0.09	4.13 ± 0.05	4.33 ± 0.07	
6-µm	Accusizer	5.58 ± 0.28	5.67 ± 0.22	6.36 ± 0.79	13.2 s
	Multisizer	6.24 ± 0.11	6.36 ± 0.05	6.46 ± 0.14	

Table 2.1. Size characteristics of microbubbles used in this study. *Measurements were made for $n \geq 3$ batches, with at least 3 measurements per batch. All size groups were found to be significantly different from each other for both sizing systems ($p < 0.01$).

2.4.1. Characterization of size-isolated microbubbles

Microbubbles were analyzed for size using data gathered from the Accusizer and Multisizer particle sizing systems, with median size and standard deviation of populations providing a benchmark for each group (Table 2.1). While both methods provide accurate concentration measurement, we recently showed that nonlinear scattering of the microbubbles may lead to binning errors and artifactual peaks in the Accusizer size distributions that slightly distort the size measurement (84). We therefore chose to use the electrical impedance Multisizer data as a more accurate representation of microbubble size. Each sample of size-isolated microbubbles was shown to have a consistent median diameter over the course of experimentation, with average median diameters of 1.7, 4.1 and 6.4 μm, and average mode diameters of 1.7, 4.3 and 6.5 μm, corresponding to the peaks in particle size distributions (Fig. 2.5). These three sizes are referred to as 2, 4 and 6-μm microbubble groups, respectively.

2.4.2. Microbubble persistence during sonication

The application of physiotherapy ultrasound (1 MHz, 2.0 W/cm^2, 10% duty cycle, 100 Hz PRF, 2-min total exposure) to a 10^8/mL suspension of microbubbles resulted in significant differences in microbubble survival depending on microbubble size. In general, larger microbubbles were more stable to insonation than smaller ones (Fig. 2.5d). For 2-μm bubbles, a 97% reduction in concentration was observed after five seconds of insonation (Fig. 2.5a). The 4-μm bubbles demonstrated a 67% reduction in concentration over the same timespan (Fig. 2.5b). The 6-μm microbubbles showed the greatest stability, dropping only 7% after five seconds of ultrasonic stimulation. A monoexponential function was fit to the concentration-time data to determine the half-life for each size group and to interpolate concentrations between the

experimental measurement times (Fig. 2.5d). Half-lives of the microbubbles were 0.7, 1.7 and 13.2 s, respectively (Table 2.1). These results were consistent with high-speed imaging results of microbubble destruction by Chomas et al. (21), who showed that smaller microbubbles with higher expansion ratios are more likely to experience fragmentation.

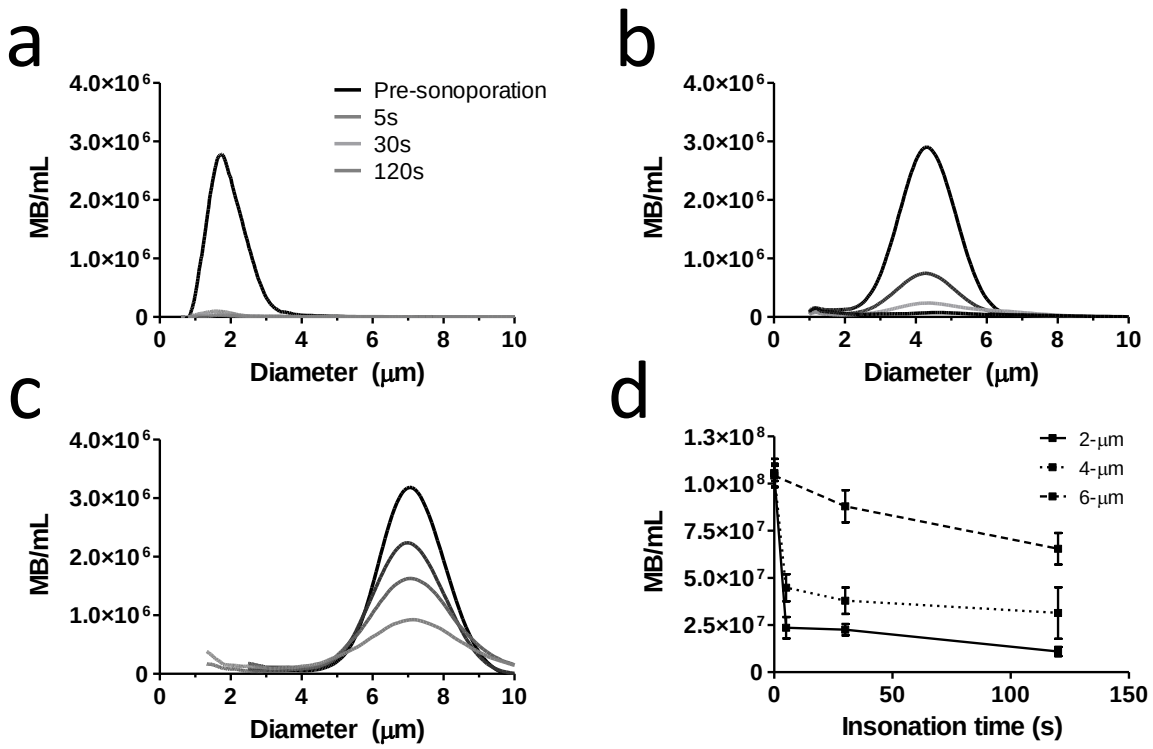

Figure 2.5. Microbubble size distributions and concentrations during ultrasonic agitation. Electric impedance measurements with the Multisizer for a) 2-μm, b) 4-μm and c) 6-μm diameter bubbles over the 2-min insonation at 37 °C. The initial concentration for each sample was 10^8/mL, and concentration measurements were taken at 5, 30 and 120 seconds (n = 3). Size distributions were processed using a fourth-order smoothing function. d) The results were aggregated to obtain microbubble concentration over time for each size group. Significant differences were found between all sizes at 5, 30 and 120 s ($p < 0.05$).

2.4.3. Visualization of sonoporation

Brightfield and fluorescence microscopy of sonoporated cells showed clear internalization of the FITC-dextran (Fig. 2.6). The control sample, which was exposed to microbubbles and FITC-dextran without insonation, showed little or no residual FITC-dextran on the cell surfaces.

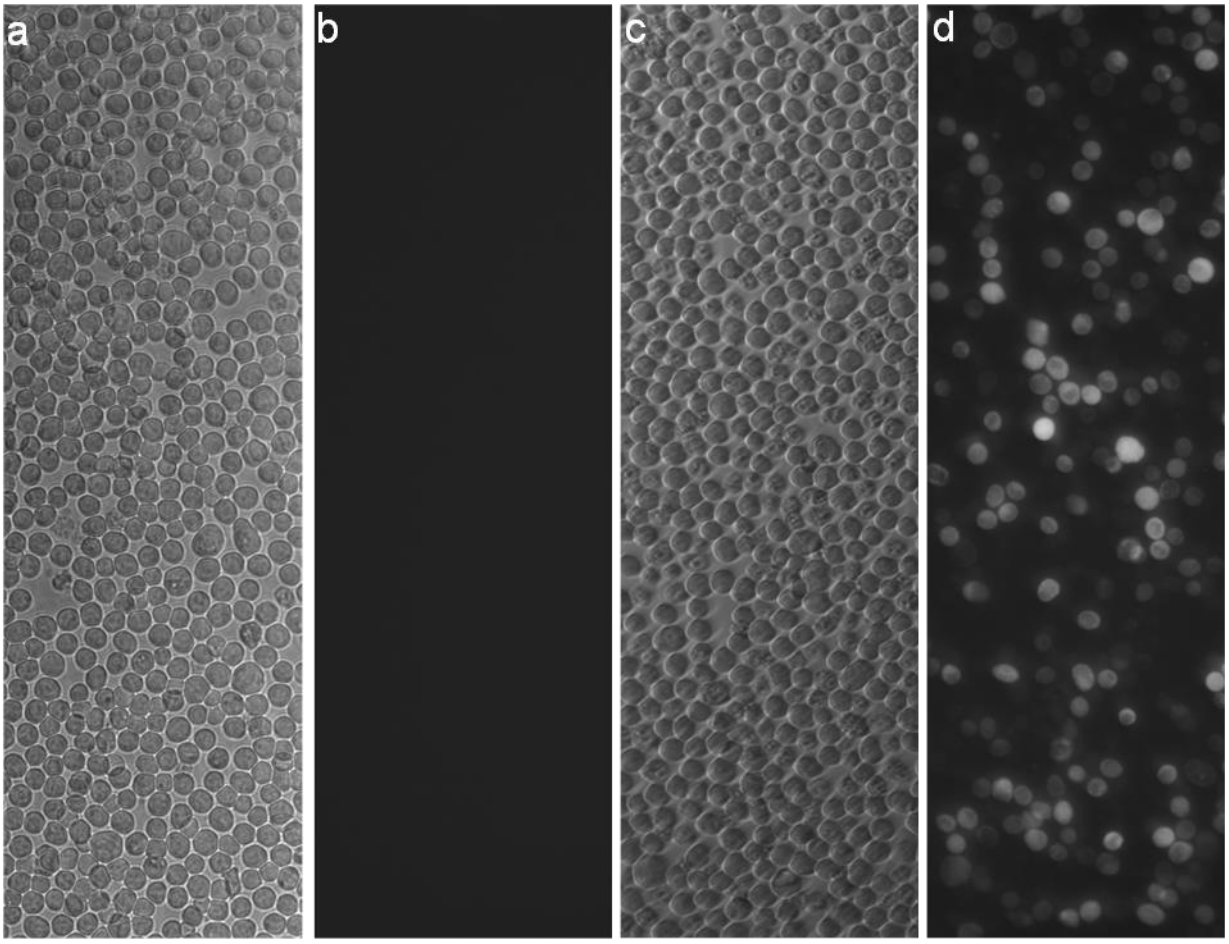

Figure 2.6. Microscopy images of control and sonoporated HeLa cells post-processed with anti-fluorescein were captured using an Olympus IX71 inverted microscope with a 20x objective. (a, b) Bright-field and fluorescence images of control cells treated with FITC-dextran and ultrasound, but not microbubbles. (c, d) Bright-field and fluorescence images of cells sonoporated with ultrasound, microbubbles and FITC-dextran. Note the cell-to-cell variation in fluorescence intensity seen in (d).

2.4.4. Sonoporation

A permeability assay was used to determine the sonoporation efficiency for each microbubble size group (32,33,53), holding ultrasound parameters as well as HeLa cell and FITC-dextran concentrations constant. Microscopy was used to confirm the uptake of FITC-dextran in sonoporated cells (Fig. 2.6). Flow cytometry allowed quantification of viability as well as the fraction and fluorescence intensity of live cells that were sonoporated (Fig. 2.3). A range of microbubble concentrations (10^6/mL to 10^8/mL) was examined for each size group. In general, all three effects (% sonoporated cells, % dead cells and sonoporated cell fluorescence intensity) increased with microbubble concentration for each size group under these sonication conditions (Fig. 2.7).

Interestingly, the smallest (2-µm diameter) microbubbles gave the highest percentage of sonoporated cells at all microbubble concentrations, with concentrations under 10^8 MB/mL exhibiting the largest size dependence (Fig. 2.7a). The smallest microbubbles also gave the lowest percentage of dead cells when compared to 4- and 6-µm microbubbles for each concentration (Fig. 2.7b). Of those live cells that were successfully sonoporated, the smallest microbubbles typically gave the lowest fluorescence intensity per cell (Fig. 2.7c).

Medium-sized (4-µm diameter) microbubbles, on the other hand, gave lower numbers of sonoporated cells (Fig. 2.7a) and higher numbers of dead cells (Fig. 2.7b) compared to the smallest microbubbles. Cell death rose significantly between 2 and 4-µm diameter microbubbles at concentrations above 10^7/mL, with differences most apparent at $5x10^7$ MB/mL. For those sonoporated cells that survived, the MFI rose significantly between cells treated with 2 and 4-µm diameter microbubbles (Fig. 2.7c).

The largest (6-µm diameter) microbubbles also gave lower numbers of sonoporated cells (Fig. 2.7a) and higher numbers of dead cells (Fig 2.7b) compared to the smallest microbubbles. While the number of sonoporated cells was approximately equal from 4- to 6-µm diameter microbubbles under 10^8 MB/mL, cell death actually decreased. This latter result appeared to be due to different microbubble/cell residence times between the two size groups (see *2.4.7 Effect of Mixing* section below). Finally, the MFI of sonoporated cells increased significantly from 4- to 6-µm diameter microbubbles.

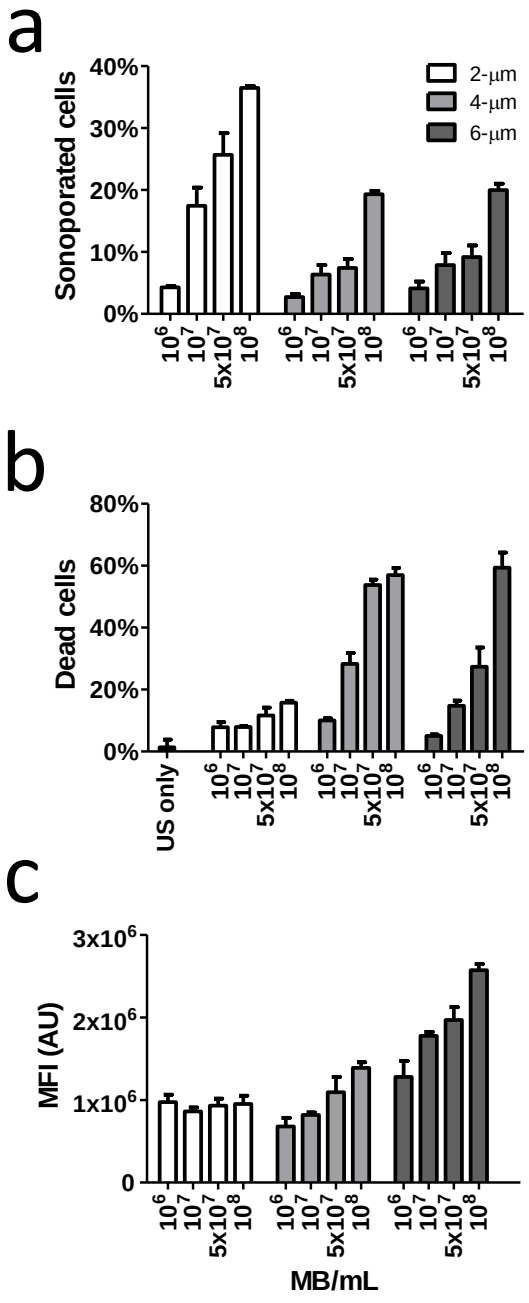

Figure 2.7. Microbubble size and concentration effects on sonoporation of HeLa cells. (a) Percentage of live cells that were sonoporated. Sonoporation with 2-μm bubbles was significantly different from 4- and 6-μm bubbles at all concentrations (n=3, $p<0.01$), while 4-μm and 6-μm bubbles were not significantly different, except at the lowest concentration of 10^6/mL. (b) Percentage of dead cells. Cell death was found to be significantly different between microbubble size groups at all concentrations except at 10^8 concentration for 4- and 6-μm treated samples (n=3, $p<0.005$). (c) Median fluorescence intensity (MFI) of sonoporated cells. The MFI of cells sonoporated with 6-μm bubbles was statistically different than those sonoporated with 2 and 4-μm bubbles at all concentrations ($p<0.01$), while the MFI of cells sonoporated with 2 and 4-μm bubbles was not statistically different at concentrations above 10^6/mL.

2.4.5. Transfection

A reporter gene assay was used to determine the transfection efficiency for each microbubble size group, again holding ultrasound parameters and cell and pDNA concentrations constant. HeLa cells were transfected with EGFP plasmid using identical parameters as in the sonoporation studies above; transfection and cell death were recorded 24 h after sonoporation. Cytometric analysis uses the same principle as protein quantification in densitometry or spectrophotometry of western blots, and median fluorescence intensity (MFI) of cell samples has been shown to provide a relative measure of EGFP expression in cells (88,89). In general, similar trends were seen between transfection (Fig. 2.8) and FITC-dextran uptake (Fig. 2.7) for microbubble size and concentration.

The smallest microbubbles gave the highest percentage of transfected cells at each microbubble concentration (Fig. 2.8a). In general, HeLa cells were transfected at much lower rates than they were sonoporated. For example, at a concentration of 10^8/mL, almost 40% of cells treated with 2-μm diameter microbubbles were sonoporated (Fig. 2.7a), whereas only about 15% of cells were transfected under the same conditions. The smallest microbubbles also gave the lowest percentage of dead cells (Fig. 2.8b). Of those live cells that were successfully transfected, the smallest microbubbles typically gave the lowest fluorescence intensity per cell (Fig. 2.8c).

Medium-sized microbubbles gave much lower numbers of transfected cells (Fig. 2.8a) and higher numbers of dead cells (Fig 2.8b) compared to the smallest microbubbles. Cell death rose significantly between 2 and 4-μm diameter microbubbles at concentrations above 10^7/mL. Indeed, 4-μm diameter microbubble-treated samples demonstrated the highest level of cell death at the highest tested concentration of 10^8/mL (Fig. 2.8b). For those transfected cells that survived, the MFI rose slightly between cells treated with 2 and 4-μm diameter microbubbles (Fig. 2.8c).

At the higher microbubble concentrations (>5x10^7/mL), the largest microbubbles gave lower numbers of transfected cells (Fig. 2.8a) and higher numbers of dead cells (Fig 2.8b) compared to the smallest microbubbles. At the lowest concentration (10^7/mL), however, 6-μm bubbles produced higher MFI and lower cell death than the 2-μm bubbles. Furthermore, the 6-μm bubbles gave higher numbers of transfected cells and lower numbers of dead cells compared to the 4-μm bubbles. As with sonoporation, this latter result may be due to different microbubble/cell residence times between the two size groups (discussed below). For all microbubble concentrations, the MFI of transfected cells was greater for 6-μm bubbles than for 2- or 4-μm bubbles.

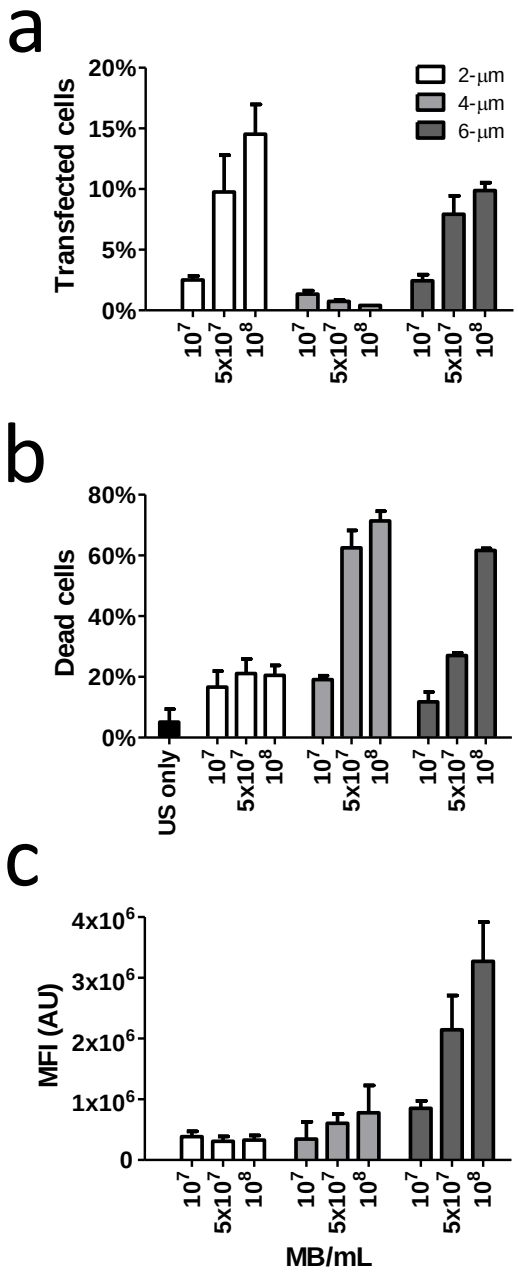

Figure 2.8. Microbubble size and concentration effects on pDNA transfection of HeLa cells. (a) Percentage of viable cells expressing EGFP after 24 h. The percentage of transfected cells differed significantly between microbubble size groups for each concentration, and between concentrations for each microbubble size group (n=3, $p<0.05$). (b) Cell death after 24 h. Cell death differed significantly for each microbubble size group between concentrations above 10^7/mL ($p < 0.01$), with the exception of $5x10^7$/mL concentration between 2- and 6-μm bubbles. However, a significant difference was observed between 4- and 6-μm bubbles at a concentration of 10^7/mL ($p < 0.05$). (c) MFI of EGFP-expressing cells after 24 h. Note the large increase in fluorescence intensity for cells sonoporated with 6-μm bubbles. MFIs were significantly different between cells sonoporated with 6-μm bubbles and 2- or 4-μm bubbles at all concentrations ($p<0.05$), as well as between cells sonoporated with 2- or 4-μm bubbles at $5x10^7$/mL.

2.4.6. Sonoporation vs. Transfection

In general, HeLa cells were transfected at much lower rates than they were sonoporated. For example, at a concentration of 10^8/mL, almost 40% of cells treated with 2-µm diameter microbubbles were sonoporated (Fig. 2.7a), whereas only about 15% of cells were transfected under the same conditions (Fig. 2.8a). The smallest decrease from % cells sonoporated to % transfected was seen for samples treated with 6-µm microbubbles (~10%).

2.4.7. Effect of mixing in the sonoporation cartridge

The cell/microbubble mixtures in the sonoporation and transfection experiments reported above were combined prior to sonoporation, but were not mixed during sonoporation. Thus, the bubbles may have de-mixed from the cells owing to buoyancy or acoustic radiation (Bjerknes forces), which both increase with microbubble size. We therefore re-designed the cartridge to allow for a mixing micro stir bar to maintain a homogenous mixture through the sonication treatment. Results are shown in Figure 2.9. Compared to unmixed sonoporations, mixed samples exhibited a progressive increase in total affected cells (sonoporated + dead cells) with increasing microbubble diameter and, specifically, a significant increase in sonoporation efficiency and cell death with 6-µm treated samples at $5x10^7$ MB/mL concentrations (Fig. 2.9).

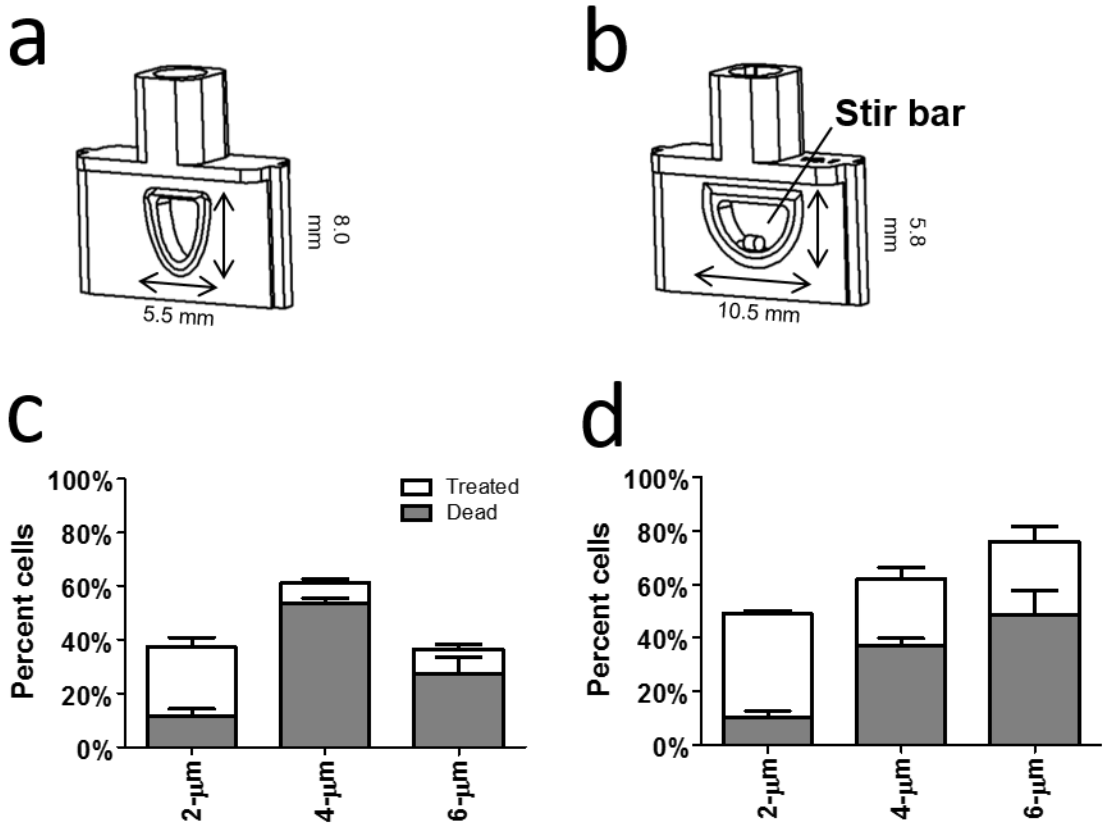

Figure 2.9. Examining the influence of Bjerknes forces. (a) The first cartridge design (unmixed) with a narrow-face window. (b) The mixing cartridge with a 2-mm long stir bar and wide-face window. (c) Percentage of sonoporated and dead cells in the unmixed samples using the first chamber shown in Fig. 1c. Note the peak in dead cells and total affected (sonoporated + dead) cells for 4-µm bubbles. (d) Percentage of sonoporated and dead cells in mixed samples using the second chamber shown in Fig. 1d. Mixing resulted in a linear increase in dead cells and total affected cells as a function of microbubble size ($n=3$, $p<0.001$).

MB size class	ΔX_{max} (μm)	$\Delta X_{max} / R_0$	R_{max} / R_0	R_{max} / R_{min}	Re_{max}	$<Re>$
2-μm	420	420	4.85	74.9	528	44.2
4-μm	660	330	3.21	93.0	944	77.1
6-μm	380	127	2.35	60.1	914	94.8

Table 2.2. Simulation results: ΔX_{max} = maximum absolute translation; $\Delta X_{max} / R_0$ = relative translation; R_{max} / R_0 = relative expansion; R_{max} / R_{min} = collapse ratio; Re_{max} = maximum instantaneous Reynolds number; $<Re>$ = time-averaged Reynolds number.

2.4.8. Theoretical microbubble dynamics

Simulations of the Marmottant model for the radial dynamics coupled with the Reddy and Szeri translation model, with the aforementioned parameters, were conducted for a pulse of ten cycles of acoustic forcing. For a PRF of 100 Hz, the simulations confirmed that the bubble oscillations completely dampen out between pulses, thus obviating the need to consider more than one pulse of the acoustic forcing. The simulation results show rapid radial collapse for all bubble sizes considered (Fig. 2.10). The maximum relative expansion, R_{max} / R_0, was observed for 2-μm bubbles, while the smallest relative expansion was observed for 6-μm bubbles. The maximum collapse ratio, R_{max} / R_{min}, however, was observed for 4-μm bubbles (Table 2.2). Thus, microbubble instability correlated with the relative expansion R_{max} / R_0, as has been observed previously (90–92).

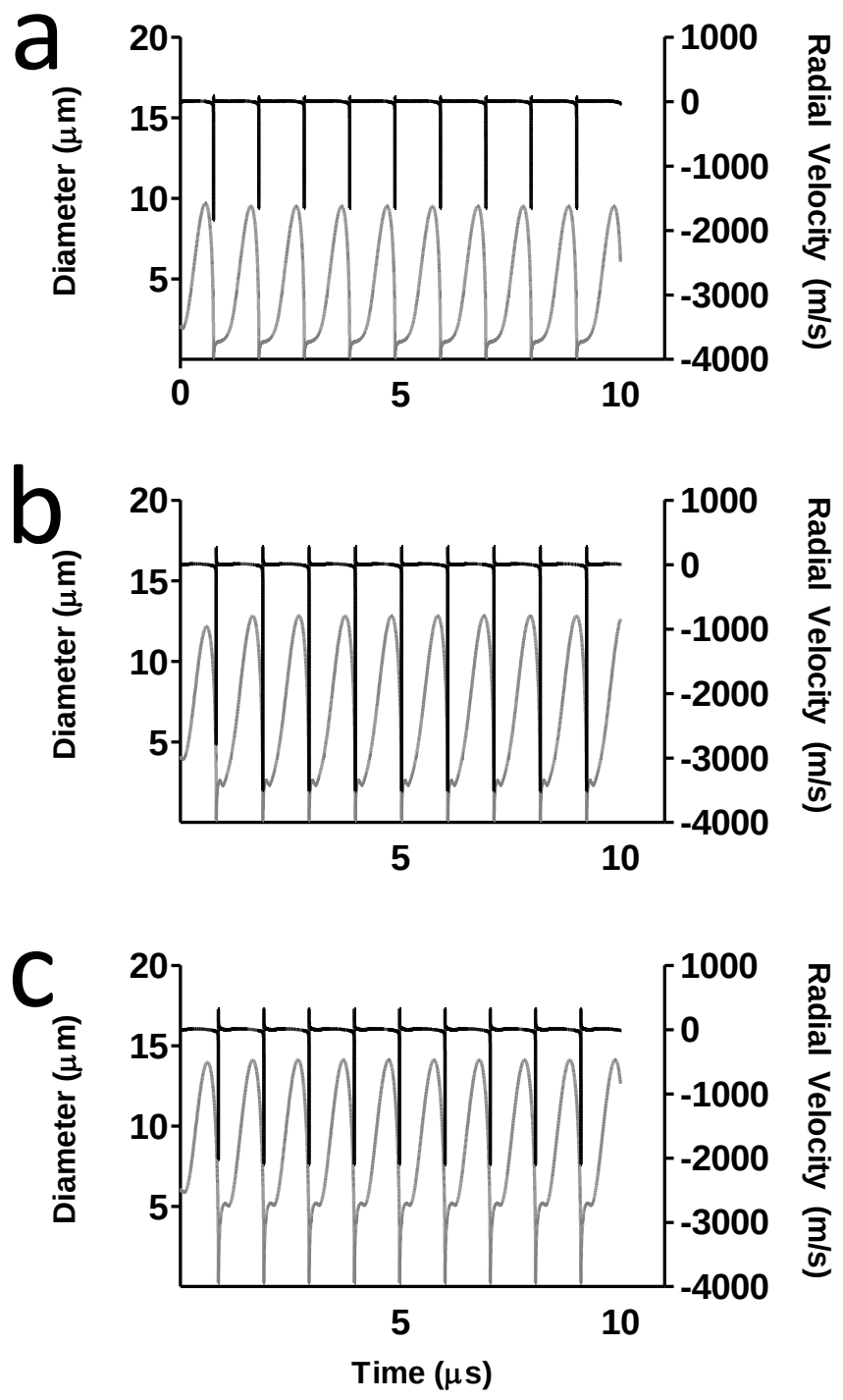

Figure 2.10. Radius (gray) and radial velocity (solid) vs. period of the acoustic forcing for initial microbubble diameters of 2- (a), 4- (b), and 6-μm (c). Velocity spikes occur in all cases during rapid radial collapse.

2.4.9. Reynolds number

The Reynolds number (*Re*) is a ratio of inertial to viscous forces, and the instantaneous values determined by our simulations are shown in Fig 2.11. Additionally, the calculated maximum and time-averaged values of *Re* are shown in Table 2.2. The time-averaged *Re* values were less than 100, indicating that overall viscous and inertial effects were of similar magnitude. The time-averaged *Re* calculations displayed an increasing trend with microbubble size. However, the high maximum *Re* values indicate that collapse was inertial for all microbubble sizes. Interestingly, 4-μm bubbles gave the highest maximum *Re* value, as well as the largest collapse ratio.

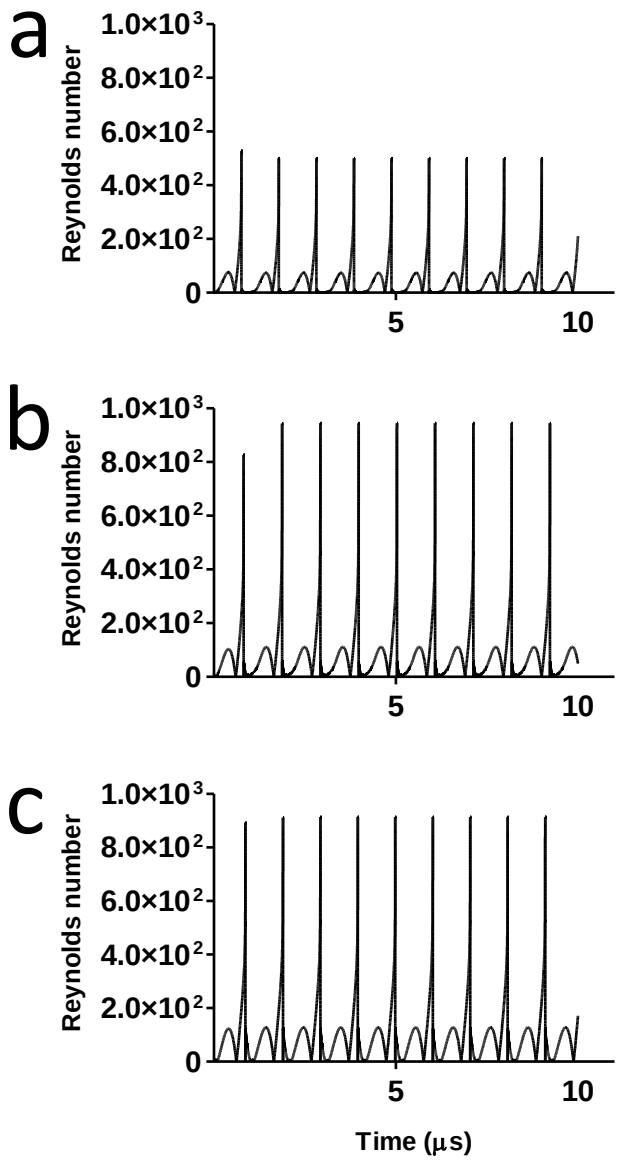

Figure 2.11. Instantaneous Reynolds number vs. period of the acoustic forcing for initial microbubble diameters of 2 (a), 4 (b) and 6- μm (c). Spikes in Reynolds number occur during rapid radial collapse in all cases.

2.4.10. Bjerknes forces

Translation simulations (Fig. 2.12) yielded the greatest relative translation for 2-μm bubbles and the greatest absolute translation for 4-μm bubbles. A rapid increase in bubble translation (lurching) was observed during collapse for all sizes. This occurred because the added momentum created by the bubble upon expansion decreases only slowly during collapse due to viscous drag, whereas the primary Bjerknes force decreased more rapidly due to the reduction in volume. Thus, the added momentum was roughly constant during the rapid collapse, causing a sharp increase in translational velocity (and displacement) as a result of the reduction in bubble volume and hydrodynamic drag (86). The theory predicted that 2, 4 and 6 μm bubbles translated 420, 660 and 380 nm per acoustic pressure cycle, respectively. Using these values, we estimate that 2, 4 and 6 μm bubbles translated a total of 420, 660 and 380 μm per second, respectively. These translational velocities far exceed those achieved by buoyancy. Since the chamber width was only 2.5 mm, we predicted that all bubbles would be pushed to the back wall of the chamber after only 7 seconds. The maximum residence time (neglecting those bubbles which are destroyed under insonation) before all bubbles were separated from cells by Bjerknes forces was 6.0, 3.8 and 6.6 seconds for 2, 4 and 6 μm bubbles, respectively.

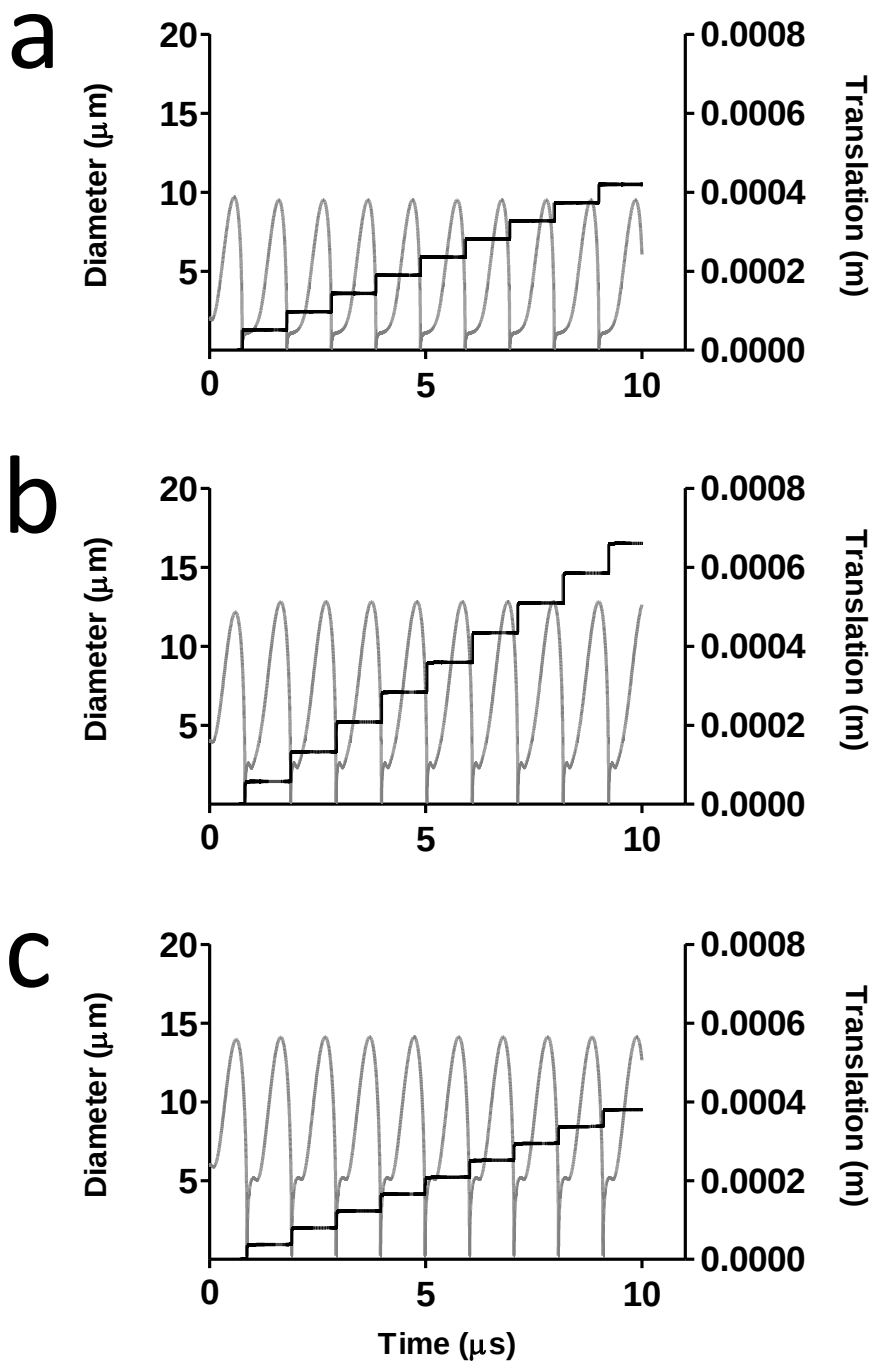

Figure 2.12. Dimensionless primary Bjerknes force-induced translation (solid) vs. period of the acoustic forcing for initial microbubble diameters of 2 (a), 4 (b) and 6- μm (c). The dimensionless radius (gray) is overlaid for comparison. Notice the forward lurching during rapid radial collapse experienced in all cases.

2.5. Discussion

It is well known that increasing ultrasonic forcing alone can increase the magnitude of microbubble-cell interactions, but we hypothesized that this would have a negative effect on microbubble persistence and microbubble-cell interactions. The goal of this study was therefore to characterize the effect of employing populations of larger microbubble sizes at a mild mechanical index (0.53), over a range of concentrations, to determine their effects on *in vitro* sonoporation and transfection. The enhanced persistence of larger microbubbles may be explained by their reduced maximum expansion ratios (R_{max}/R_0) compared to those seen in smaller microbubbles under the same acoustic conditions, as suggested by previous high-speed videomicroscopy studies (91,92). Our mathematical modeling of microbubble cavitation using the Marmottant model predicted that the expansion ratio of 6-μm microbubbles is less than half that of 2-μm microbubbles under these acoustic forcing conditions (Table 2.2). It seems likely that this increased longevity also extends the time in which large microbubbles sonoporate cells. MFI is an indicator of the magnitude of EGFP pDNA expression (93), and the results presented here show that the longer interaction time of the large-diameter microbubbles increases drug uptake. This enhanced drug-uptake effect seems to derive primarily from microbubble longevity, as revealed by the unvarying MFI across all concentrations of the shortest-lived 2-μm microbubbles, and the rapid increase in MFI with concentration for 6-μm treated cells. Similarly, cell death appears to be related to microbubble longevity. We speculate that while decreasing acoustic output may have a negative effect on sonoporation efficacy (94), it may also reduce cell death and improve therapeutic effect (33). There is the additional possibility that larger pores may be created by larger microbubbles (17). This would allow for favorable uptake of the larger pDNA molecules, but promote cell death due to increased cytoplasm-buffer material exchange.

Interestingly, the trend in the percentage of sonoporated and dead cells effected by low concentrations ($<10^8$ MB/mL) of microbubbles was non-linear in relation to increasing microbubble size (Fig. 2.7). The sonoporation cartridge used in this portion of the study was designed without a stir bar to minimize acoustic reflections within the sample (Fig. 2.9a), and thus we attributed this effect to the premature segregation of microbubbles from cells by buoyancy or Bjerknes radiation forces. The effect of microbubble sequestration was subsequently characterized by the use of a continuously mixing sonoporation cartridge (Fig. 2.9b), which indicated that suspensions treated with 6-µm microbubbles were more affected by sequestration than those treated with small- and mid-diameter (2 or 4 µm) microbubbles (Fig 2.9 c and d). Similarly, increasing 6-µm concentration to 10^8 microbubbles/mL in unmixed trials produced a dramatic increase in the total number of treated cells, suggesting that increasing the number of available microbubbles could partially mitigate the effect of sequestration. It was worth noting that the non-linear trend, resulting from the absence of stirring, highlighted a positive relationship between MFI and microbubble size, but not between MFI and cell death or sonoporation efficiency.

The results of this study indicate that several factors such as microbubble size, concentration and separation forces interact dynamically to affect sonoporation efficiency. With respect to the role of large-diameter microbubbles for sonoporation of suspended cells, the additional control over drug-delivery and improvement in drug-uptake is promising. Owing to the size-dependent nature of cavitation behavior (91), varying microbubble size should allow for a wider range of acoustic intensities, mechanical outputs and interaction times. Additionally, previous investigations have shown that different microbubble behaviors, such as inertial cavitation and translation, may affect cell viability and therapeutic effect (94), and the results here demonstrate that these behaviors can also be tuned with microbubble size.

In comparison with existing methods such as electroporation, size-isolated microbubbles may provide improvements in transfection efficiency and additional control over cellular poration (Fig. 2.13). In the context of optimizing microbubble-assisted sonoporation, we propose a three-step process: 1) selection of acoustic parameters based on the optimal performance of the sonoporation device; 2) adjustment of microbubble size to maximize drug delivery (the fraction of cells with drug uptake or, alternatively, the amount of drug uptake per cell) and minimize cell death for the particular target cell or tissue type; and 3) optimization of the microbubble concentration and sonoporation time. We note in the following chapter that size may offer a tradeoff between instantaneous power and total energy delivered per cell, owing to the vastly different persistence. Finally, while *in vivo* trials present very different biological and mechanical parameters, we speculate that large-diameter microbubbles will be most useful in such applications where increased microbubble persistence and mechanical energy outweigh the risk of small-scale tissue damage (58).

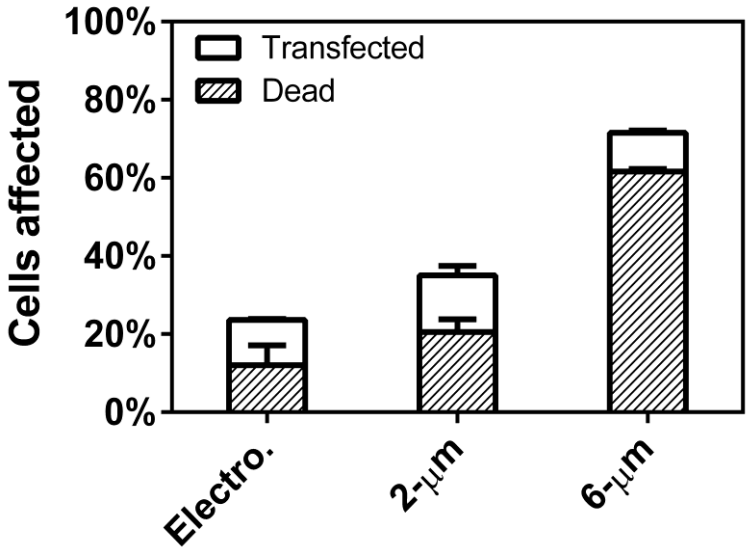

Figure 2.13. A comparison of CMV-EGFP-plasmid transfection efficiencies between electroporation, 2- and 6-μm unmixed microbubble sonoporation of HeLa cells.

Chapter 3. High efficiency molecular delivery with sequential low-energy sonoporation bursts

Theranostic applications of *in vitro* sonoporation include molecular delivery (e.g., transfection, drug loading and cell labeling), as well as molecular extraction for measuring intracellular biomarkers, such as proteins and mRNA. Prior research focusing mainly on the effects of acoustic forcing with polydisperse microbubbles has identified a "soft limit" of sonoporation efficiency at 50% when including dead and lysed cells. We show here that this limit can be exceeded with the judicious use of monodisperse microbubbles driven by a physiotherapy device (1.0 MHz, 2.0 W/cm^2, 10% duty cycle). We first examined the effects of microbubble size and found that small-diameter microbubbles (2 μm) deliver more instantaneous power than larger microbubbles (4 & 6 μm). However, owing to rapid fragmentation and a short half-life (0.7 s for 2 μm; 13.3 s for 6 μm), they also deliver less energy over the sonoporation time. This translates to a higher ratio of FITC-dextran (70 kDa) uptake to cell death/lysis (4:1 for 2 μm; 1:2 for 6 μm) in suspended HeLa cells after a single sonoporation. Sequential sonoporations (up to four) were consequently employed to increase molecular delivery. Peak uptake was found to be 66.1 ± 1.2% (n=3) after two sonoporations when properly accounting for cell lysis (7.0 ± 5.6%) and death (17.9 ± 2.0%), thus overcoming the previously reported soft limit. Substitution of TRITC-dextran (70 kDa) on the second sonoporation confirmed the effects were multiplicative. Overall, this study demonstrates the possibility of utilizing monodisperse small-diameter microbubbles as a means to achieve multiple low-energy sonoporation bursts for efficient *in vitro* drug uptake and sequential drug delivery.

3.1. Introduction

Sonoporation uses acoustically mediated cavitation of microbubbles to porate nearby cells through the induction of micro/nanoscale ruptures in the plasma membrane for intracellular delivery of diverse payloads, such as nucleic acids and nanoparticles (95). Unlike electroporation, which uses strong electric field gradients that act on all structures throughout the sample volume, sonoporation generates localized thermal and mechanical effects that function on cells regardless of cell-media composition. Engineering of the microbubbles allows for more advanced effects, such as targeting of surface proteins and co-imaging with diagnostic ultrasound.

One popular application of *in vitro* sonoporation has been cellular transfection with pDNA (34,68). However, sonoporation offers many more theranostic applications, such as *ex vivo* transfer of therapeutic and imaging molecules for *in vivo* transplantation (i.e., cell labeling(96–99), and transient pore formation for the release and detection of intracellular proteins and mRNA (100,101). Additionally, *in vitro* sonoporation can serve as a surrogate for drug testing on *in vivo* disease models (102,103).

One major challenge for sonoporation for theranostic applications has been increasing cell uptake efficiency. A review by Liu et al. revealed that out of 26 *in vitro* sonoporation studies spanning over a decade, none had demonstrated cellular uptake in excess of 50% when accounting for cell lysis and death in their measurements (67). The goal of our study was to surpass this "soft limit" by achieving at least 50% uptake efficiency with monodisperse microbubbles, while properly accounting for cells that were lysed or otherwise lost during handling.

Prior *in vitro* sonoporation studies have focused mainly on optimization of acoustic parameters with commercially available ultrasound contrast agents, which are highly polydisperse in size (29,104–106). Recent studies, however, have demonstrated microfluidic (107–114) and

centrifugal size sorting (115) methods to produce monodisperse microbubbles of select size. *In vivo* studies have shown dramatic effects of monodisperse microbubble size on imaging (80) and therapeutic (58) performance. This is not surprising: microbubble size is known to affect resonance, oscillation power and stability (21,92,116). We therefore chose to focus on microbubble size as the key parameter to optimize *in vitro* sonoporation efficiency, using a new high-throughput cartridge/bracket system with commonly employed ultrasound parameters (1 MHz, 0.53 MPa peak negative pressure) delivered by an inexpensive physiotherapy device.

Currently, the effect of microbubble size on sonoporation is limited to observations on individual cells. For example, research by Zhou et al. (17,43) demonstrated that larger microbubbles formed larger pores, potentiating the possibility of delivering larger drug molecules than previously possible with commercially available small-diameter microbubble formulations (53). For cell suspensions, however, the situation is made more complex by the three dimensional structure of the cell/microbubble suspension, the transient nature of microbubbles and other effects.

We thus structured our study to engineer a method of sequential sonoporations (Fig. 3.1) to overcome the 50% soft limit on uptake efficiency utilizing: 1) Previously examined microbubble size (2, 4 and 6 μm diameter) effects on dynamics and stability, 2) the effects on cell uptake (% treated cells: live FITC-present), death (% lysine-binding-dye stained cells), lysis (% reduction in total cell count) and unaffected cells. We then verified the limited multiplicative nature of the process through multi-colored sonoporation utilizing FITC- and TRITC-dextran (70 kDa) as indicators of cells sonoporated in the first and second rounds of treatment.

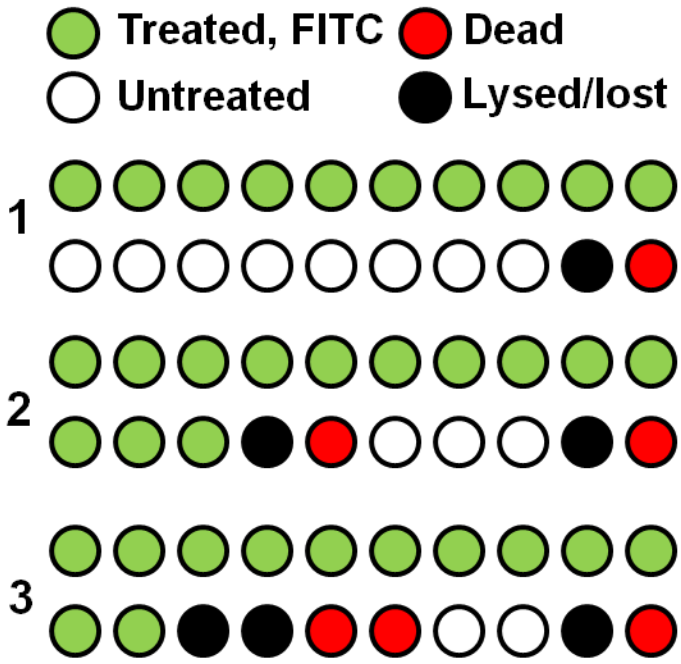

Figure 3.1. Illustration of changing cell populations over multiple sonoporations.

3.2. Materials

1,2-distearoyl-*sn*-glycero-3-phosphocholine (DSPC) and 1,2-distearoyl-sn-glycero-3-phosphoethanolamine-N-[(polyethylene glycol)-2000] (DSPE-PEG_{2000}) lipid powder was obtained from Avanti Polar Lipids (Alabaster, AL, USA) for microbubble preparation. Perfluorobutane (PFB) gas was obtained from FluoroMed (Round Rock, TX, USA). HeLa cells (ATCC, Manassas, VA, USA) were cultured in DMEM solution (Fisher Scientific, Hampton, NH, USA). 70 kDa FITC-dextran (Sigma-Aldrich, St. Louis, MO, USA) was used for sonoporation assays. Plasmid EGFP-C3 (Clontech, Mountain View, CA, USA) was used for transfection assays, and dead cells were stained with ethidium homodimer-1 or lysine-binding dye (Invitrogen, Grand Island, NY, USA).

3.3. Experimental Methods

3.3.1. Microbubble preparation and characterization

Lipid-encapsulated perfluorocarbon microbubbles were generated via sonication of DSPC and DSPE-PEG_{2000} lipid suspension at a concentration of 2 mg/mL and molar ratio of 9:1 in phosphate buffered saline (PBS) solution, in the presence of PFB gas. Microbubbles with median diameters of 2, 4 and 6 μm were separated based on size using differential centrifugation (80,115). Microbubble size and concentration were measured with an Accusizer 780 (PSS Nicomp, Santa Barbara, CA, USA) and a Multisizer 3® (Beckman Coulter, Brea, CA, USA).

3.3.2. Radial dynamics calculations

Simulations were conducted via MATLAB (Mathworks, Natick, MA, USA) as described in *2.3.9 Radial dynamics calculations*. The modeling of the radial dynamics of a lipid shell

microbubble is performed through implementation of the model by Marmottant et al. (2005), which considers a variable surface tension in three linear regimes, dependent on bubble area (13).

3.3.3. Calculation of microbubble oscillation power and energy

Doinikov's equation for the time-averaged non-dimensional power output was used to estimate the relative power delivered by each microbubble per second under these acoustic forcing conditions (116):

$$W(R_0) = \frac{1}{\Delta t}\int_0^T \left(\frac{R(t)}{R_0} - 1\right)^2 \times C(t)dt, \tag{3.1}$$

where Δt is one second (1000 cycles per pulse at 100 Hz pulse repetition frequency), R_0 is the initial microbubble radius (1, 2 or 3 μm), $C(t)$ is the dynamic microbubble concentration obtained from persistence data and $R(t)$ is the dynamic radius, which was obtained from Marmottant's model for the experimental acoustic driving conditions. These power values for each microbubble size were then integrated over time to obtain the energy delivered to each cell suspension, using the following equation:

$$E_{sono} = \sum_0^T W \times \Delta t\,, \tag{3.2}$$

where Δt is the time step (1.0 s) and T is the total exposure time of 120 s.

3.3.4. In vitro sonoporation system

The sonoporation system described in *2.3.2 Design and fabrication of the* in vitro *sonoporation system* was modified with a stir-bar cartridge to induce continuous mixing of cell-microbubble suspension during sonoporation. The acoustic chamber was constructed to

incorporate a 1-inch diameter ultrasound transducer from a Dynatron® 125 (Dynatronics, Salt Lake City, Utah) applying acoustic pulses to a removable 3-D printed sample holder held at a fixed location by a bracket assembly (Fig. 2.1; 117). The ultrasonic output from the transducer was characterized by a needle hydrophone (HNC-0200, Onda Corp., Sunnyvale, CA) and shown to output a 1.0 MHz, 0.53 ± 0.03 MPa peak negative pressure sound wave at a setting of 2.0 W/cm^2, and 1000 cycles per pulse at 100 Hz pulse repetition frequency at a setting of 10% duty cycle (Fig. 2.2). The cartridge was designed with two acoustically transparent polystyrene windows and an interior bevel to minimize cell retention, as well as a 2-mm magnetic stir bar. Window attenuation and waveform distortion were inspected and found to be minimal at a distance of 5 mm from the trailing acoustic window. The polypropylene bracket was designed for immersion in water up to 40 °C and allowed for the exchange of cartridges with minimal variation in cartridge position relative to the transducer. De-ionized and de-gassed water held at a temperature of 37 °C was used as an acoustic medium.

3.3.5. Cell culture and handling

HeLa cells were procured from ATCC (Cat no. CCL-2) and thawed from 10% DMSO solution. Thawed cells were cultured at 37 ºC, 5% CO_2 in DMEM with 10% fetal bovine serum supplement (Fisher Scientific, Hampton, NH) and 1% penicillin/streptomycin (Sigma-Aldrich, St. Louis, MO) and passaged until healthy growth patterns were observed. Cells were trypsinized and harvested at 70% confluence for use in sonoporation studies. Cell concentrations during sonoporation were held constant at $5x10^6 \pm 2.5x10^5$ for each experimental group.

3.3.6. Cellular sonoporation assay

FITC-dextran (70 kDa, 0.77 mg/mL, Sigma-Aldrich, St. Louis, MO), a long-chain sugar with a fluoroscein isothiocyanate moiety, was chosen as the indicator of cell permeabilization and uptake (53). 20 μL of FITC-dextran (7.7 mg/mL) was added to 180 μL of microbubble/cell suspension (11 μM final concentration). The sonoporated volume remained 200 μL for all sonoporation conditions. Microbubble concentration was fixed at $5x10^7$ for each group size (2, 4 and 6 μm diameter). Higher microbubble concentrations were avoided due to the high viscosity exhibited by larger size groups. Cell/microbubble/FITC-dextran suspensions were then subjected to ultrasound (1 MHz, 2.0 W/cm^2, 10% duty cycle) in the sonoporation system. Treated cell samples were removed from the cartridges and washed three times at 500 RCF in 15-mL cell media tubes. Anti-fluorescein (Invitrogen, Grand Island, NY) was added at a volume fraction of 2 μL in 1 mL (2 μg/mL) to quench residual fluorescence on exterior cell surfaces after the third wash to eliminate FITC fluorescence from non-permeabilized cells. Finally, ethidium homodimer-1 was applied at 0.2 M quantity to each sample to identify damaged (non-viable) cells and minimize false positives from auto-fluorescence.

3.3.7. Sequential sonoporations

Separate samples were prepared for each number of sequential sonoporations (n=3); thus, three samples were prepared for one sonoporation and analyzed, then three more samples were prepared for two sonoporations and analyzed after the second sonoporation, and so on. Total cell count was obtained before the first sonoporation and after the last sonoporation by removing 50 µL aliquots for flow cytometric measurement. For a single sonoporation, the samples were sonicated for ten seconds with 2-µm microbubbles (10^8/mL in 200 µL). For additional sonoporations, 2×10^7 microbubbles were added to the 200 µL sonoporation volume (10^8 microbubbles/mL). The total volume of microbubbles added after the fourth sonoporation (<12 µL) was considered minimal compared to the total sonoporation volume (200 µL). Sonoporations were repeated up to four times, then cells were removed from the cartridge and washed three times at 500 RCF in 1.5-mL tubes to remove excess dye. Lysine-binding dye was applied at 0.2 M quantity to each sample to identify damaged (non-viable) cells. Any surviving microbubbles were destroyed by transferring samples to a 12-mL syringe and pressurizing the sample to 10 atm for 5 s.

3.3.8. Predictions of sonoporated fractions

Predictions were made on the multiplicative effects of sequential sonoporations using the following system of equations. The fractions of treated (χ_T), dead (χ_D) and lysed (χ_L) cells after the first sonoporation were determined based on data from a prior study with single sonoporation under similar conditions (36), and their values were held constant to predict the effects from subsequent (second, third and fourth) sonoporations. The total number of initial cells (N_0) contained a small fraction ($\chi_{D,0}$ = 3%) of dead cells owing to trypsinization, resuspension and handling. Thus, the initial number of dead cells was given as:

$$N_{D0} = \chi_{D,0} N_0 \tag{3.3}$$

The remaining cells prior to sonoporation were therefore "untreated" cells (i.e., viable and non-fluorescent):

$$N_{U,0} = (1 - \chi_{D,0}) N_0 \tag{3.4}$$

The initial number of treated ($N_{T,i}$) and lysed ($N_{U,0}$) cells was zero. Following each sonoporation, the total number of cells (N_i) declines owing to lysis:

$$N_i = N_0 (1 - \chi_L)^i \tag{3.5}$$

where index i is the sonoporation number and $\chi_{,L}$ is the fraction of cells lysed in each sonoporation step ($\chi_{,L}$ = 3%). The number of lysed cells increases with each sonoporation:

$$N_{L,i} = N_0 - N_i \tag{3.6}$$

The number of dead cells following the i sonoporation step ($N_{D,i}$) is given by:

$$N_{D,i} = (1 - \chi_{,L})(N_{D,i-1} + \chi_D N_i) \tag{3.7}$$

where χ_D is the fraction of cells killed in each sonoporation step (χ_D = 7%). Therefore, the number of treated ($N_{T,i}$) and untreated ($N_{U,i}$) cells following the $\underline{i}$ sonoporation step are given by:

$$N_{T,i} = (1 - \chi_L - \chi_D)(N_{T,i-1} + \chi_T N_{U,i-1}) \quad (3.8)$$

$$N_{U,i} = N_i - N_{L,i} - N_{D,i} - N_{T,i} \quad (3.9)$$

where χ_T is the fraction of cells treated (viable and fluorescent) produced in each sonoporation step (χ_T = 49%). Equations 3.3-3.9 were iterated with each sonoporation step (i = 1 to 4) to predict the numbers of treated, dead, lysed and untreated cells. These simple model predictions were then compared to experimental results using the methods discussed below.

3.3.9. Multi-color sonoporations

To further characterize the effect of the second sonoporation in a double-sonoporated sample, we used a three-color assay. The first sonoporation was conducted with green FITC-dextran and cells were washed and treated with anti-FITC, and TRITC-dextran (7.5 mg/mL) was then substituted for FITC-dextran in the second sonoporation. Washed cells were treated with anti-tetramethylrhodamine (20 µg/mL) before far-red lysine-binding dye was added to stain dead cells.

3.3.10. Flow cytometric analysis

A flow cytometer (Accuri C5, Ann Arbor, MI) was used to count and analyze populations of fluorescent cells. Cells were gated in the forward-vs-side scatter plot and were isolated from the serpentine pattern of microbubbles (84). Once gated in the scatter plot, cells were analyzed for fluorescence by plotting FL1 (520 nm, FITC) vs. FL2 (585 nm, TRITC, ethidium homdimer-1) and gating for dead cells (FL4, 630 nm, far-red lysine-binding dye; Fig. 3.2).

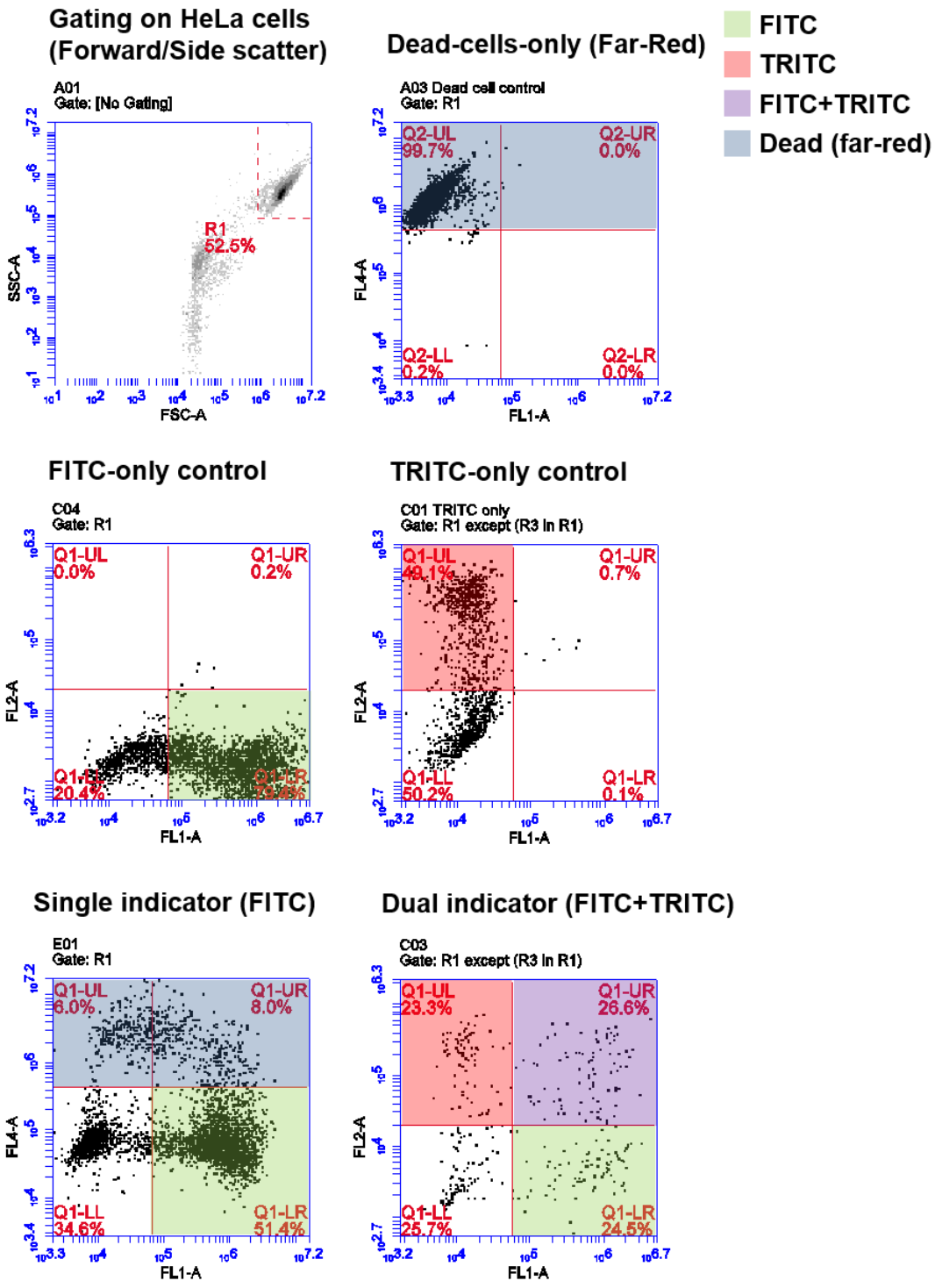

Figure 3.2. Flow cytometry gating for single- and dual-indicator studies. Fluorescence compensation was performed using controls for FITC/far-red (0% spectral overlap), and between FITC-TRITC (27.1% overlap). Cell samples were gated using scatter, and fluorescent cells were detected using three channels for FITC (FL1A), TRITC (FL2A) and far-red lysine-binding dye (dead cells, FL4A).

3.3.11. Data analysis

Comparison of sonoporation and transfection results was conducted through unpaired Student's t-tests between size groups in Prism software (GraphPad, La Jolla, CA, USA). Significant differences were determined for two sample groups if the p-value was found to be smaller than 0.05 ($n \geq 3$).

3.4. Results and Discussion

3.4.1. Microbubble dynamics and persistence

In section *2.4.1 Characterization of size-isolated microbubbles*, each sample of size-isolated microbubbles was shown to maintain a consistent median diameter over the course of experimentation, with average median diameters of 1.7, 4.1 and 6.4 μm, and average mode diameters of 1.7, 4.3 and 6.5 μm. These three sizes are referred to as 2, 4 and 6 μm microbubble groups, respectively.

In previous studies, sonoporation stress was modeled as a function of wall velocity (118–120). We therefore calculated the theoretical radius-time curves for the three microbubble sizes (Fig. 2.10) using the experimentally validated model by Marmottant et al. for large-amplitude oscillations in (12). Under the acoustic driving conditions employed in this study, theory predicts that smaller microbubbles should experience more severe oscillations, i.e., larger relative expansion ratios and wall velocities.

However, the theory does not account for microbubble instabilities, such as dissolution and fragmentation, which may limit the lifetime. We therefore measured microbubble persistence under these acoustic conditions. Our previous results showed that larger microbubbles were more stable to insonation than smaller ones (Fig. 2.5d, Table 2.2). For 2-μm bubbles, a 97% reduction

in concentration was observed after five seconds of sonoporation. The 4-μm bubbles demonstrated a 67% reduction in concentration over the same time span. The 6-μm microbubbles showed the greatest stability, dropping only 7% after five seconds of ultrasonic stimulation.

3.4.2. Theoretical power and energy output

With knowledge of the experimental lifetimes and theoretical dynamics, we were able to compute theoretical power and energy outputs for each microbubble size from equations 3.1 and 3.2, respectively (Fig. 3.3). Our modeling results predicted that increasing microbubble size would reduce the instantaneous power output of each microbubble, but increase the total energy delivered owing to longer persistence (Fig. 2.5d, Table 2.2). This presented an interesting dichotomy: small microbubbles provide high-intensity bursts, whereas large microbubbles produce greater overall energy at a lower intensity. Our next experiment was designed to examine the relative importance of power and energy to sonoporation by measuring the effects on uptake, death and lysis.

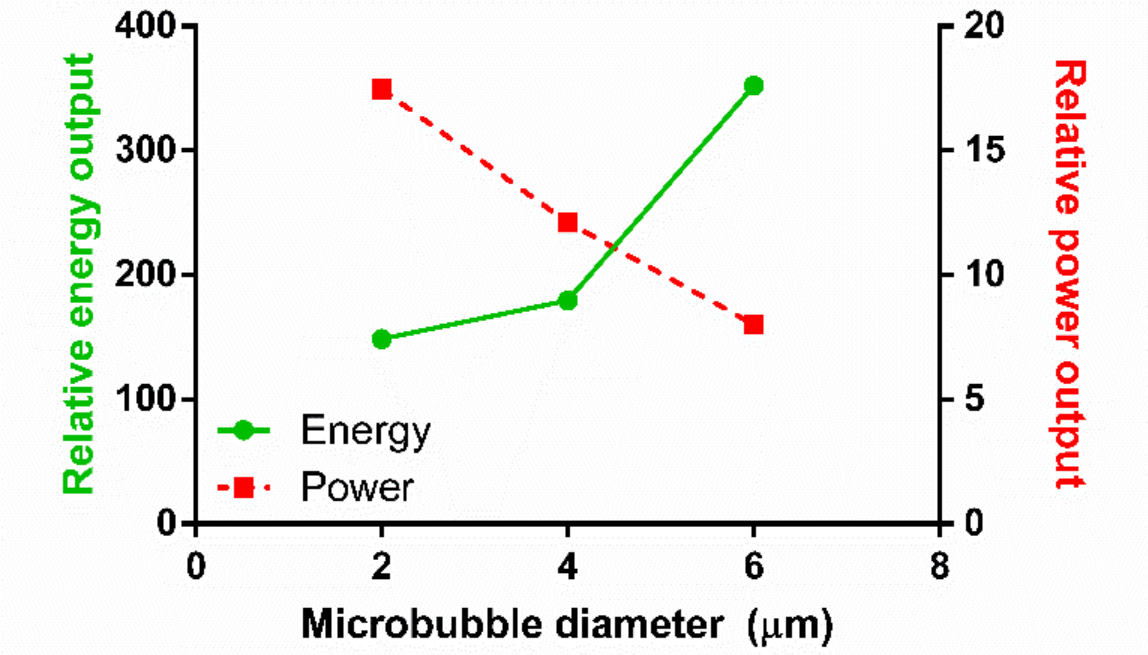

Figure 3.3. Theoretical energy output. Microbubble size vs. calculated power (dotted line) and energy (solid line), obtained from Doinikov's non-dimensional power equation (Equation 1) and an energy model incorporating time and observed concentration values (Equation 2), respectively.

Sono #	Treated		Dead		Untreated		Lysed/Lost	
	Mean	SD	Mean	SD	Mean	SD	Mean	SD
0	0.6	0.3	2.8	0.9	93.9	4.9	2.6	5.5
1	49.7	0.4	9.9	0.8	39.4	0.8	0.7	2.9
2	66.1	1.2	17.9	0.8	9.0	1.8	7.0	5.6
3	38.4	2.6	43.8	3.8	5.1	1.4	12.4	3.1
4	13.2	6.3	51.2	6.0	5.3	0.5	29.9	2.6

Table 3.1. The effect of multiple sonoporations on cellular uptake, death and lysis.

3.4.3. Sequential sonoporations

The second goal of this study was to optimize cellular uptake in context of minimizing cell death and lysis over multiple sonoporations. The results from *2.4.7 Effect of mixing in the sonoporation cartridge*, indicated that 2-µm microbubbles produced enough sonication power to induce cell membrane rupture, but the total energy delivered was relatively nonlethal. This suggests a new paradigm for understanding and controlling *in vitro* sonoporation: that high-intensity bursts are more effective than high-energy exposures. Thus, small-diameter (2 µm) microbubbles are desirable due to their ability to induce high uptake (49.7%) and low cell death (9.9%) after a single sonoporation. Their primary deficiency is the large number of unaffected cells (>39%) remaining after a single sonoporation. In order to overcome this limitation, we next investigated the use of sequential sonoporations.

As implemented, sequential sonoporation retains the high-power, low-energy nature of 2-µm bubbles while multiplying the energy output in relatively small increments. Figure 3.4 shows that increasing the number of sonoporations resulted in increased number of live fluorescent ("treated") cells, as well as an increase in cell death and lysis. FITC-dextran uptake peaked at 66.1 ± 1.2% after two sonoporations including lysis. Omitting lysed cells from the total cell count, sonoporation efficiency was found to be 71.1 ± 1.3%. In this fashion, we were able to exceed the soft limit of 50% uptake when including both lysed and dead cells in the total count (Table 3.1).

Corresponding to this decrease in uptake between sonoporation #2 and 3 was a significant increase in cell death (17.9 ± 2.0 → 43.8 ± 3.77%). This increase was less pronounced between #3 and 4 (43.8 ± 5.1% → 51.2 ± 6.0%). Instead, cell lysis increased significantly between the third and fourth sonoporations (12.4 ± 3.1% → 29.9 ± 2.6%).

While it is still possible that microbubble and acoustic parameters could be optimized for high-efficiency single sonoporations, there appears to be an intrinsic interaction limit stemming from the transient nature of microbubbles, which restricts the number of cells the microbubble suspension can affect before clearance. It is therefore advantageous to use sequential sonoporations. Our results suggested that sonoporations are multiplicative out to the second sonoporation under these conditions (Fig. 3.5), beyond which the cell death and lysis rates increase disproportionately. A second potential advantage of sequential sonoporation is multi-drug delivery, which we examined next with the use of two different fluorescent probes.

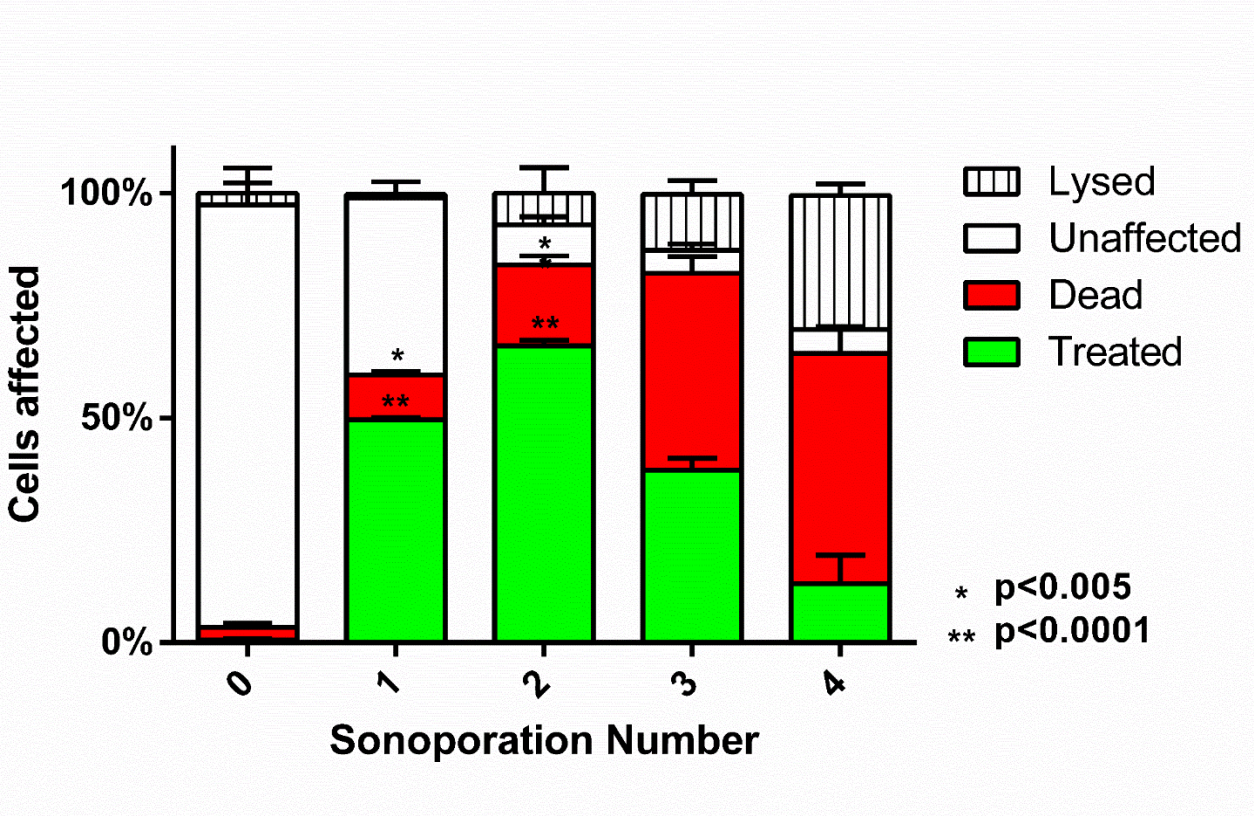

Figure 3.4. The effect of sequential sonoporations on cell uptake, death and lysis as measured by flow cytometry. The initial microbubble concentration for each sample was 10^8/mL, and cell counts were obtained before and after sonoporation to determine cell loss (n=3). FITC-Dextran uptake peaked at the second sonoporation ($p<0.05$), with cell death and lysis increasing disproportionately over subsequent sonoporations.

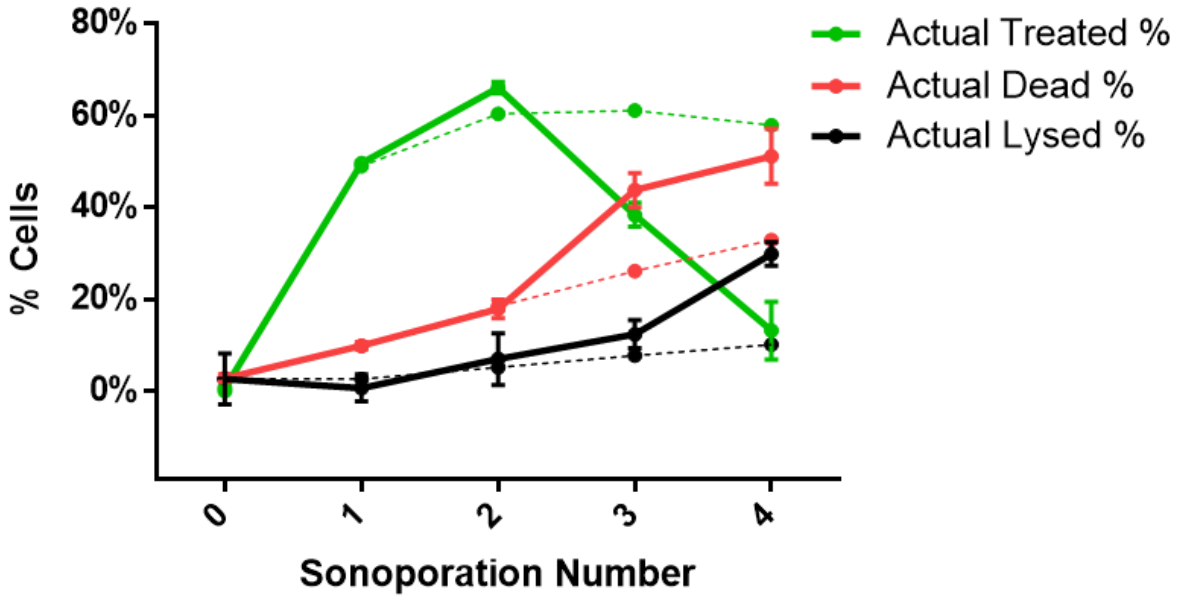

Figure 3.5. A comparison of predicted (dotted) and experimentally derived (solid lines) treated cells (green), cell death (red) and lysis (black lines).

	FITC-only		TRITC-only		Co-Fluorescent	
	Mean	SD	Mean	SD	Mean	SD
Live	23.8	1.3	23.3	0.5	26.6	1.6
Dead	20.8	0.3	19.9	1.2	23.7	3.4

Table 3.2. The % presence of three distinct fluorescent populations after two sonoporations in intact cells.

3.4.4. Multi-color sonoporations

Fractions of live cells were analyzed by multi-color sonoporation in order to separate uptake from the effects of cell death. Fluorescent marker uptake from the first sonoporation indicated that approximately 55% of live cells were treated after each sonoporation. Changing the fluorescent uptake marker from FITC to TRITC for the second sonoporation resulted in three distinct fluorescent populations: FITC-only (23.8 ± 1.3%), TRITC-only (23.3 ± 0.5%), and FITC+TRITC co-fluorescent (26.6 ± 1.6%) cells (Fig. 3.6, Table 3.2). Cell death in multi-color experiments were similar to those found in FITC-only trials (22.1 ± 1.4% vs. 17.9 ± 2.0%). Indeed, dual-color sonoporations produced multiplicative trends similar to predicted values (see supplemental information): a single sonoporation induced FITC-dextran uptake in 49.7% of the cells, and the second sonoporation resulted in 66% uptake (73.7% when not counting dead or lysed cells). Substituting TRITC for the second sonoporation further supported multiplicative uptake, with 25-30% co-fluorescent (FITC and TRITC-present) cells resulting from two sonoporations.

As an investigative tool, sequential sonoporation may yield further insight into cellular stress and mortality to supplement single-cell sonoporation studies done under the microscope (17). In our study, further analyses of cell populations revealed that after two sonoporations, the number of dead co-fluorescent cells was not significantly higher than dead single-sonoporated cells, suggesting that cell stress thresholds were only exceeded after cells were sonoporated three

times. Future studies could investigate the effect of cellular resting periods between sonoporations to further reduce cell stress and improve therapeutic efficiency.

Combined with systematic identification of cell stress thresholds, sequential sonoporation allows for predictable and sequential delivery of multiple drugs to cell populations, facilitating the study of interdependent drug effects. Further optimization of the sequential sonoporation methodology could employ microbubbles of various concentrations, diameters and shell compositions in each sonoporation (as well as various ultrasound parameters) to achieve the desired percentage, magnitude and specificity of effect for each drug type. Finally, commercially available formulations used in previous sonoporation studies are often generated by the user, utilizing mechanical perturbation or resuspension of dried product in media. This may introduce variations in size-distributions and concentration as demonstrated by vastly differing size-distributions of Definity™ microbubbles from vial-to-vial (62,121). We believe that strict control and verification of microbubble size-distribution and concentration will allow for improved consistency and reproducibility of future sonoporation studies.

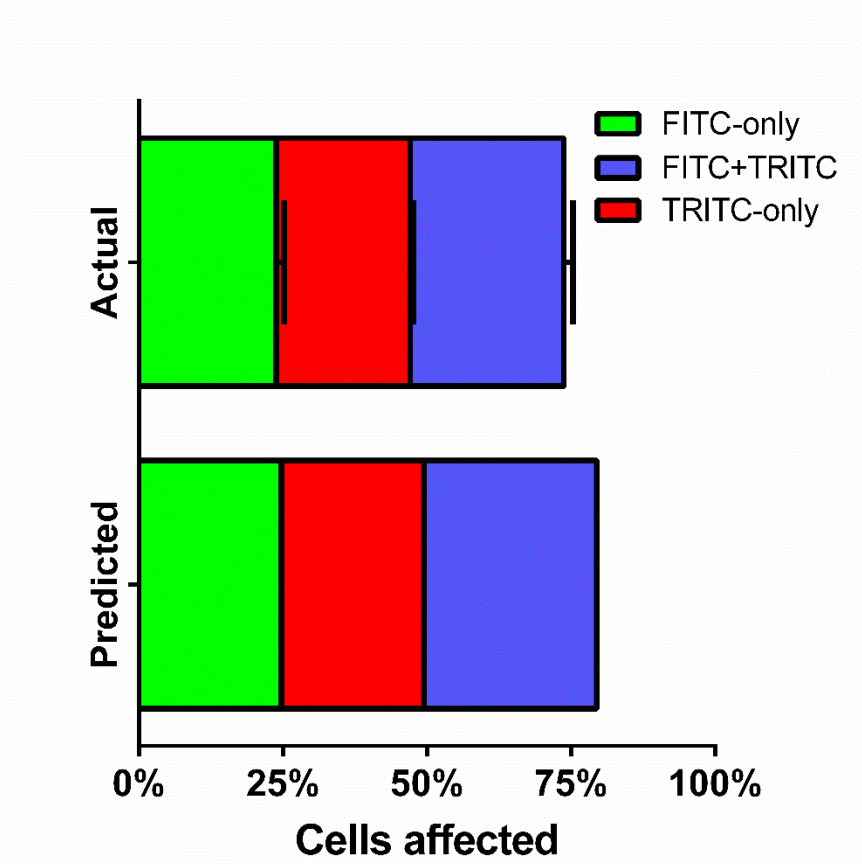

Figure 3.6. Multi-color uptake of FITC- and TRITC-dextran uptake over two sonoporations. FITC-dextran was used as an uptake marker in the first sonoporation, and cells were washed and processed before a second sonoporation in the presence of TRITC-dextran (n=3).

Chapter 4. The effect of microbubble-volume dose on blood-brain barrier opening by focused ultrasound

Focused ultrasound with microbubbles is currently being developed to transiently, locally and noninvasively open the blood-brain barrier (BBB) for improved pharmaceutical delivery. Prior work has demonstrated that, for a given concentration dose, microbubble size affects both the intravascular circulation persistence and extent of BBB opening. When matched to the total volume of entrapped gas injected (volume dose), however, the circulation half-life was found to be independent of microbubble size. Whether BBB opening is dominated by the pharmacodynamics of this volume dose or size-intrinsic mechanisms is unknown. In the current study, we measured the effects of microbubble size (2 vs. 6 μm diameter) and concentration, covering a range of overlapping volume doses (1-40 μL/kg). We first demonstrated precise targeting and a linear dose-response of Evans blue dye extravasation to the rat striatum for a set of constant microbubble and ultrasound parameters. We found that dye extravasation increased linearly with volume dose, regardless of bubble size—an effect that was observed for both the initial sonication ($R^2 = 0.90$) and a second treatment on the contralateral side ($R^2 = 0.68$). Based on these results, we conclude that microbubble volume dose, not size, determines the extent of BBB opening by focused ultrasound. This result should greatly simplify planning for focused ultrasound treatments by constraining the protocol to a single microbubble parameter – volume dose – which gives equivalent results for varying size distributions.

4.1. Introduction

The blood brain-barrier is an obstacle in the treatment of neurological diseases and disorders owing to the impermeability of the tight-junction-rich brain vasculature to hydrophilic

molecules larger than ~400 Da (122). Surgical approaches or chemical agents used to breach the blood-brain barrier (BBB) are highly invasive or induce off-target effects, respectively. Ligand-receptor based delivery schemes are attractive due to their targeting potential, but such vehicles are limited in their specificity, affinity and overall ability to deliver sufficient quantities of therapeutic agent through active transport mechanisms (123). Sonoporation by focused ultrasound (FUS) in the presence of microbubbles is a particularly attractive noninvasive approach for permeabilizing the BBB due to its transient effect on vasculature (124), as well as its ability to target specific brain regions utilizing stereotaxic coordinates (58) or image guidance (125). The microbubbles used in sonoporation are theranostic agents owing to their dual roles as therapeutic agents and highly echogenic ultrasound imaging probes. Compared to viral, liposomal, nanoparticle- or polymer-based methods, sonoporation/microbubble-mediated gene or drug delivery offers an alternative delivery vehicle with the potential for ligand-receptor targeting (126), payload conjugation and biocompatibility (70,127), as well as *in situ* targeting by the use of focused ultrasound. Additionally, microbubble-assisted sonopration offers a less invasive alternative to *in vivo* electroporation, and clinical translatability owing to its common use in echocardiology as an FDA-approved ultrasound contrast agent (128).

Previous work on BBB sonoporation has focused on delivery of either chemotherapeutic agents or gene therapy (125,129–131). Early work on BBB sonoporation in humans focused on safety and model drug propagation using the MRI contrast agent, gadolinium, as an indicator of permeabilization (132). The first characterization studies of sonoporation parameters investigated the effects of acoustic intensity in rabbits on MRI-scanned temperature and tissue changes (56), as well as the effects of microbubble size in non-human primates (64). The first study of chemotherapeutic delivery to the brain using sonoporation demonstrated remarkable tumor

reduction in rat glioma models compared to administering drug alone (133). In 2015, Carpentier et al. (130) and Hynynen et al. (unpublished) first demonstrated successful BBB permeabilization and the delivery of chemotherapeutic agents to brain tumors in human subjects. In the context of recurring treatments, a single-site multi-sonoporation study demonstrated the feasibility and safety of repeated sonoporations of the BBB (134). Additionally, sonoporation of microbubbles intravenously co-injected with adeno-associated viral vectors has been used for transgene delivery to the brain (135–137,131,138).

Characterization of sonoporation parameters for BBB opening have primarily focused on acoustic parameters, and few studies have focused on the actual object inducing permeabilization: the microbubble. Size has been identified as a primary determinant of a microbubble's persistence in circulation *in vivo* (80). When matched for concentration, 6-µm diameter bubbles circulate over tenfold longer than 2-µm bubbles. Remarkably, when matched for volume dose (using 27-fold more 2-µm bubbles than 6-µm bubbles), the half-life was equivalent. Using equivalent bubble concentration, Choi et al. demonstrated a significant increase in BBB opening with microbubble size (58). Prior work from the Borden lab showed a microbubble size effect on *in vitro* sonoporation (139). To our knowledge, however, the effect of volume dose on BBB opening has not been investigated. It is therefore unclear whether molecular delivery will scale with microbubble diameter, even at the same volume dose, owing to inertial versus stable cavitation, acoustic resonance, the microbubble-to-vessel aspect ratio, interaction volume or other size effects. Alternatively, do microbubble pharmacodynamics – which were shown to scale with volume dose instead of size (80) – determine the extent of BBB permeabilization?

To examine the effect of microbubble size and volume, we performed BBB permeabilization studies in rats using two size-isolated microbubble formulations (2- and 6-µm

diameter). We used a concentration range with overlapping volume doses (1-41 µL). The two striata of the rat brain were selected, as these regions are well-define, large anatomical structures in the brain and are common targets for evaluating therapeutics in rat models of Parkinson's disease. To characterize microbubble persistence under multi-site sonoporation, both left and right striata were sonicated in serial FUS applications.

4.2. Materials

Size-isolated cationic microbubbles (MB) were obtained from Advanced Microbubble Laboratories (Boulder, CO, USA) with the following diameters: 2-, 6-µm; and shell composition: 70 mol% 1,2-distearoyl-*sn*-glycero-3-phosphocholine (DSPC), 20 mol% 1,2-distearoyl-3-trimethylammonium-propane (DSTAP) and 10 mol% 1,2-distearoyl-sn-glycero-3-phosphoethanolamine-N-[(polyethylene glycol)-2000]. Cationic microbubbles have been shown to enhance microbubble-endothelium surface interactions compared to neutral microbubbles (140), and demonstrate less adherence to leukocytes in a classical ischemia-reperfusion damage model (141). Microbubble size and concentration were measured using a Z2 Coulter counter (Beckman Coulter, Sharon Hill, PA). Evans Blue (EB) powder (Sigma Aldrich, St. Louis, MO) was solubilized in phosphate buffered saline (PBS, pH 7.4, Thermo Fisher Scientific, Waltham, MA). For EB concentration vs. intensity measurements, microbubbles and saline (0.9% NaCl) were mixed to generate 4 mL/kg total injection volumes containing 1, 2 or 4 wt% EB and $4x10^8$ MB/kg bodyweight. For microbubble concentration vs. intensity measurements, $4x10^8$, $2x10^9$ and $4x10^9$ MB/kg of 2-µm MB, or $4x10^7$, $2x10^8$ and $4x10^8$ MB/kg of 6-µm MB were mixed with 4 mL/kg of 2 wt% EB solution.

4.3. Experimental Methods

4.3.1. Sonoporation

In vivo sonoporations were conducted using a Therapy Imaging Probe System (TIPS) focused ultrasound transducer and controller (Philips, Andover, MA). Thirty six adult male Sprague Dawley Rats weighing 300-400 g and 13-15 weeks of age were utilized for this study in accordance with National Institutes of Health Animal Care Guidelines. Figure 4.1 illustrates the sonoporation of striatum and the experimental timeline used for all studies unless otherwise noted. Rats were anesthetized with isoflurane and placed on a heated stereotaxic platform. A centimeter-long incision was made along the sagittal suture starting at lambda and used as a window to align the ultrasound transducer to bregma. The incision was then pushed back from the bregma, exposing uninterrupted scalp to the sonicating transducer, which was then coated in ultrasound gel. A water-filled drape was mated to the scalp, and the transducer was targeted to a depth of 6 mm under the skull surface. The transducer was moved 0.5 mm anterior and 3 mm lateral to bregma using a motorized stage, and the MB/EB cocktail was subsequently injected via a tail vein catheter. The right striatum was sonicated at a setting of 1 MHz center frequency, 1 MPa peak negative pressure, 100 Hz pulse repetition frequency and 10% duty cycle. After five minutes, the transducer was moved to laterally 6 mm (- 3 mm relative to midline) to the left striatum, which was then treated for another five minutes.

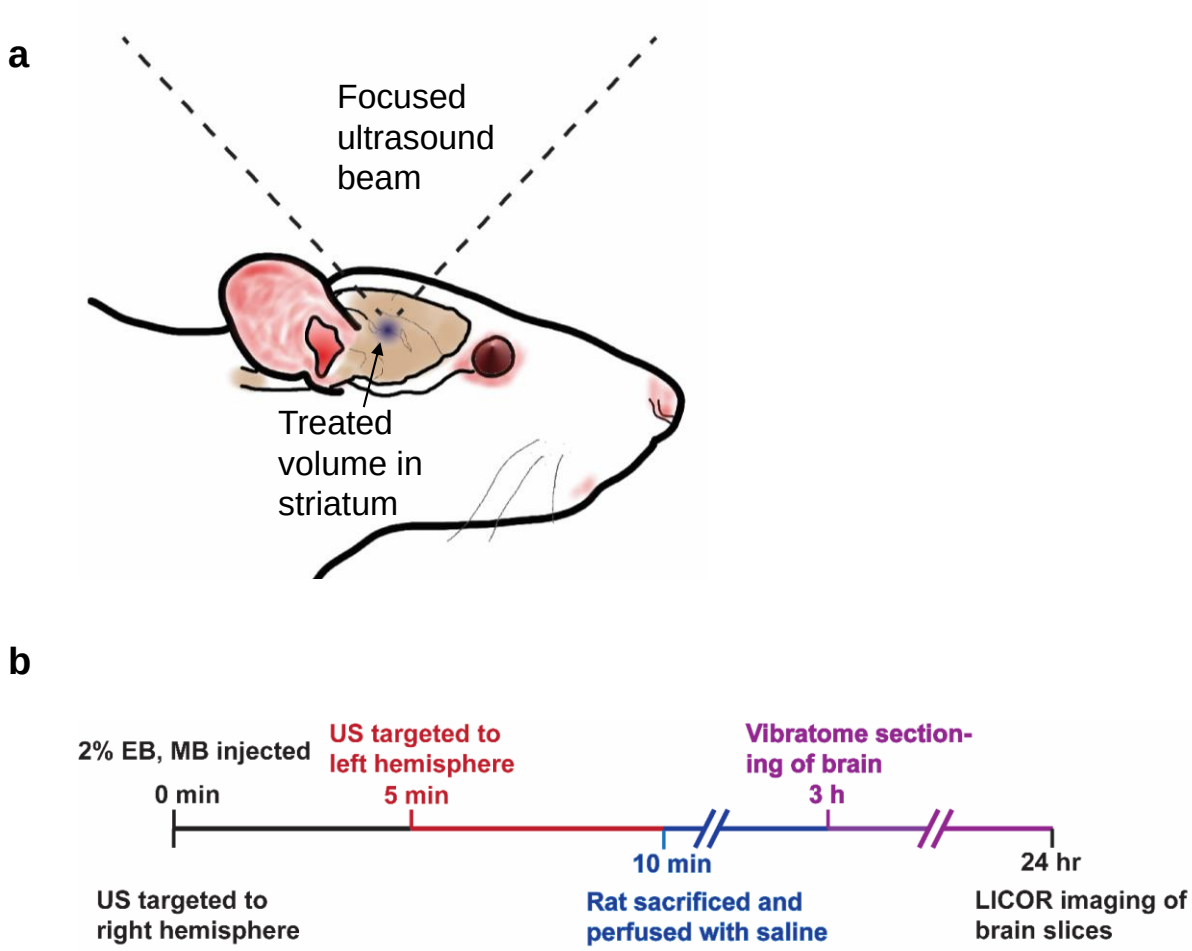

Figure 4.1. a) Transcranial sonoporation layout with Philips Therapy-Imaging Probe System. b) Timeline of sonoporation, perfusion and post-processing steps.

4.3.2. Analysis of BBB Opening

Immediately after sonoporation, rats were deeply anesthetized with isoflurane and transcardially perfused with heparinized saline at room temperature. Five 400-µm thick brain slices spanning the striatum were made using a Vibratome (Leica, Buffalo Grove, IL). Brain slices were placed in 4% paraformaldehyde solution and allowed to fix overnight at 4°C. Twenty-four hours after sonoporation, slices were imaged using the 700 nm channel of a flatbed near infrared (NIR) Odyssey scanner (Li-Cor, Lincoln, NE) at 42-µm resolution, 0.5 intensity.

Raw images of five brain slices from each specimen were obtained from the Odyssey scanner, stacked and overlaid into one image utilizing ImageJ software (NIH, Bethesda, MD) for image analysis. Integrated fluorescence intensity from equally sized ROIs was determined to represent the total EB fluorescence from one brain (n = 3 per condition). Statistical analysis such as means, standard deviation, Student's unpaired t-test and linear regressions were conducted in Graphpad Prism v6.0 (La Jolla, CA).

4.4. Results

4.4.1. Characterization of size-isolated microbubbles

Microbubble size distributions were assessed by microscopy and quantified by Coulter counter (Fig. 4.2). The two size-isolated lipid microbubble formulations showed median diameters of 1.7 and 5.7 μm and mean diameters of 1.7 and 5.8 μm, respectively. The size distributions exhibited minimal overlap. These two microbubble formulations are referred to as 2 and 6-μm.

4.4.2. Qualitative analysis of sonoporation

Brightfield and NIR fluorescence scanned images of slices taken from the targeted striatal regions demonstrated consistent targeting of EB to the center of the striatum on both right (0-5 min sonoporation) and left (5-10 min) hemispheres of the brain, with less EB present in the left (contralateral) hemisphere (Fig. 4.3). Extravasated EB and small pockets of red blood cells were visible in the focal region, with diffuse EB surrounding the focal region. NIR images of these brain slices demonstrate further presence of EB in larger regions surrounding the focal region.

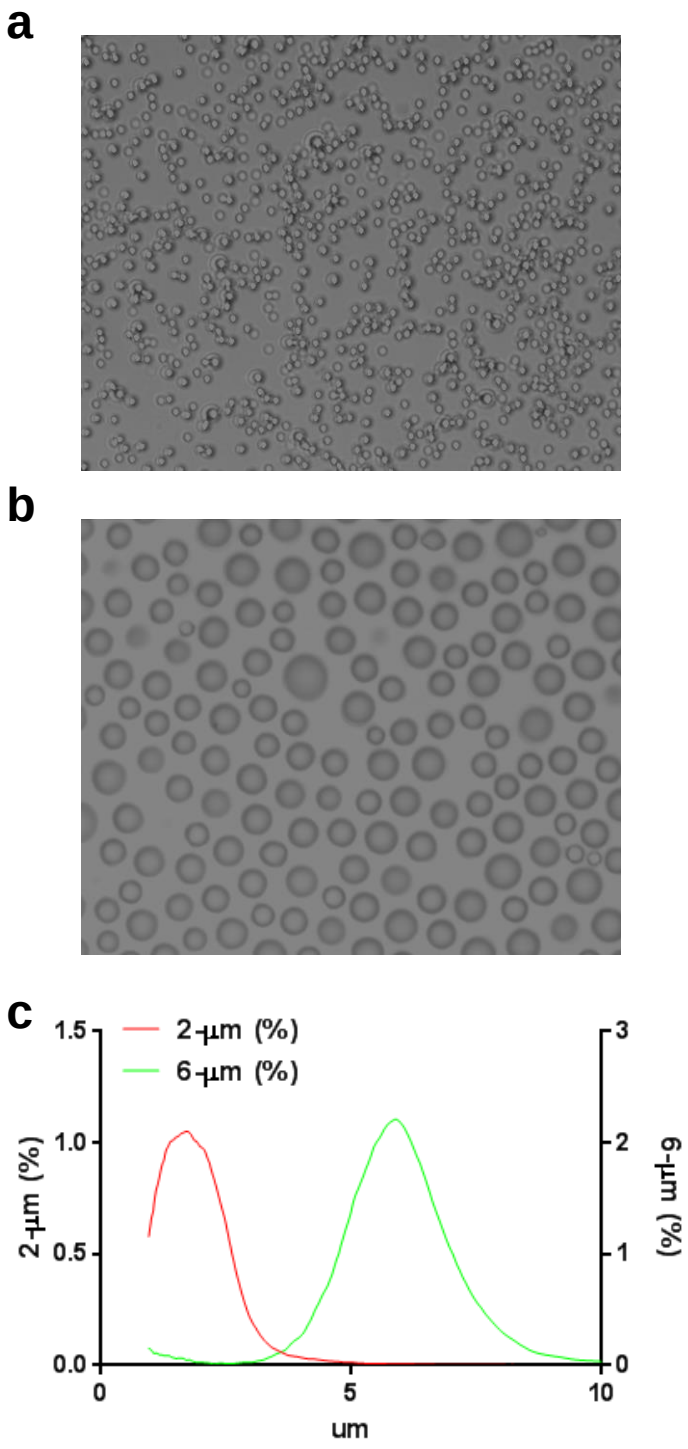

Figure 4.2. Size distribution of a) 2- and b) 6-µm microbubbles. (c) Size distribution plots by number %.

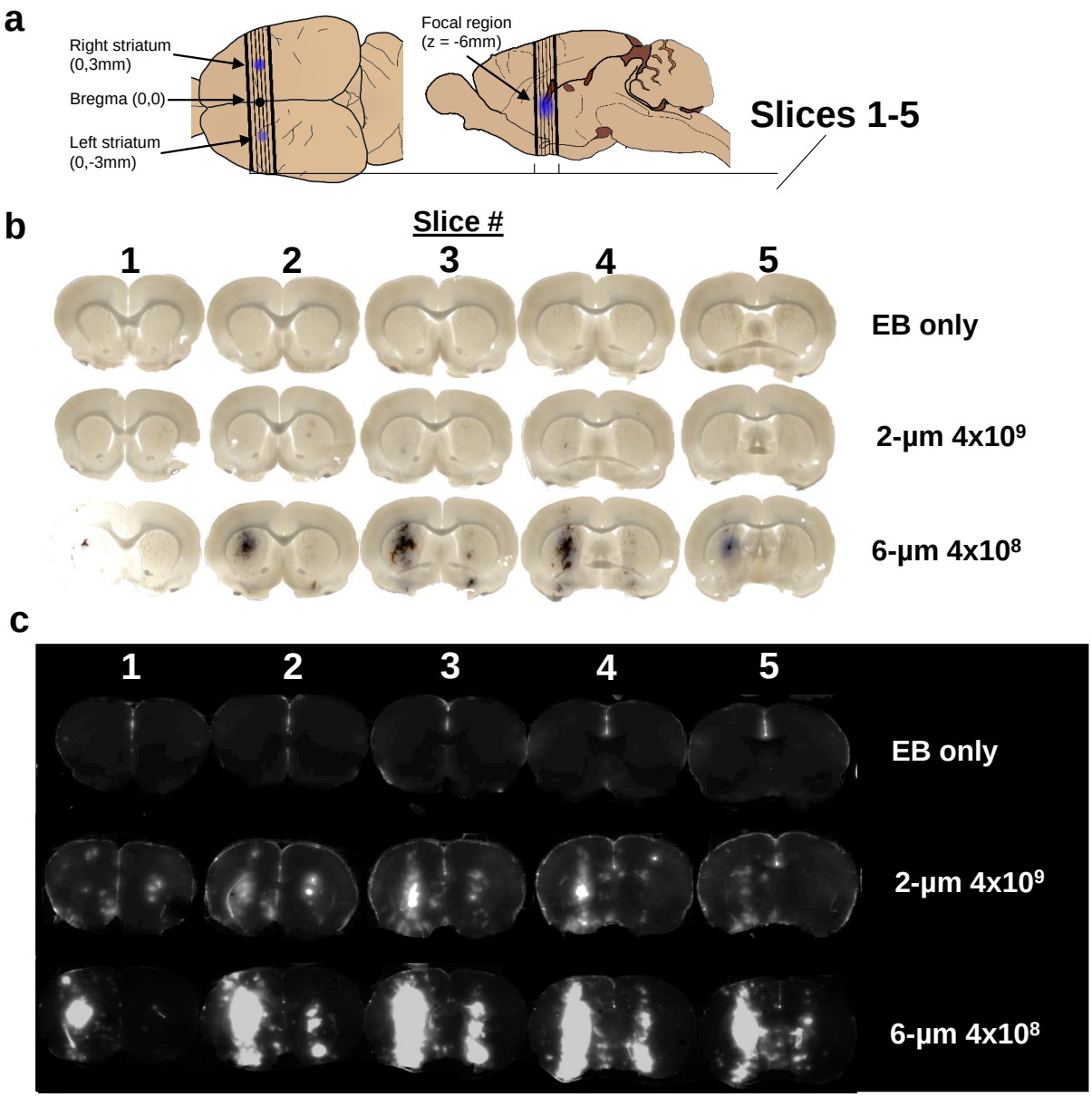

Figure 4.3. a) Location of Evans Blue permeabilization within left and right stiratum, and brain slices analyzed for LICOR measurements. b) Brightfield and c) LICOR images of no-microbubble; 2% EB, 2-µm, $2x10^9$ MB/mL·kg; and 4% 6-µm $2x10^9$ MB/ml·kg treated brains.

4.4.3. Evans Blue (EB) dose response

We next examined whether EB exhibited a linear dose-response at constant sonoporation parameters. When plotted as a function of slice number, EB fluorescence followed a consistent trend, exhibiting peak intensity at the third (middle) slice across all EB concentrations (Fig. 4.4a), with a minimum integrated intensity per slice of $8.0\times10^6 \pm 9.9\times10^4$ AU in slice 1 of the control brains, and a maximum (non-saturated) intensity of $9.4\times10^7 \pm 2.9\text{x}10^7$ AU in slice 3, when the concentration of EB was 4 wt% (n = 3). EB concentrations of 0, 1, 2 and 4 wt% positively correlated with increasing fluorescence intensity values of $2.6\times10^6 \pm 2.6\times10^6$, $5.9\times10^7 \pm 1.3\times10^7$, $2.2\times10^8 \pm 4.4\times10^7$ and $4.7\times10^8 \pm 2.3\times10^7$ AU (n = 3), respectively, in slice 3. Figure 4.4b shows a linear fit of the data points (fluorescence intensity = 1.13 [EB] + 0, $R^2 = 0.97$), thereby showing the expected dose-response trend and validating the sensitivity of our analysis method.

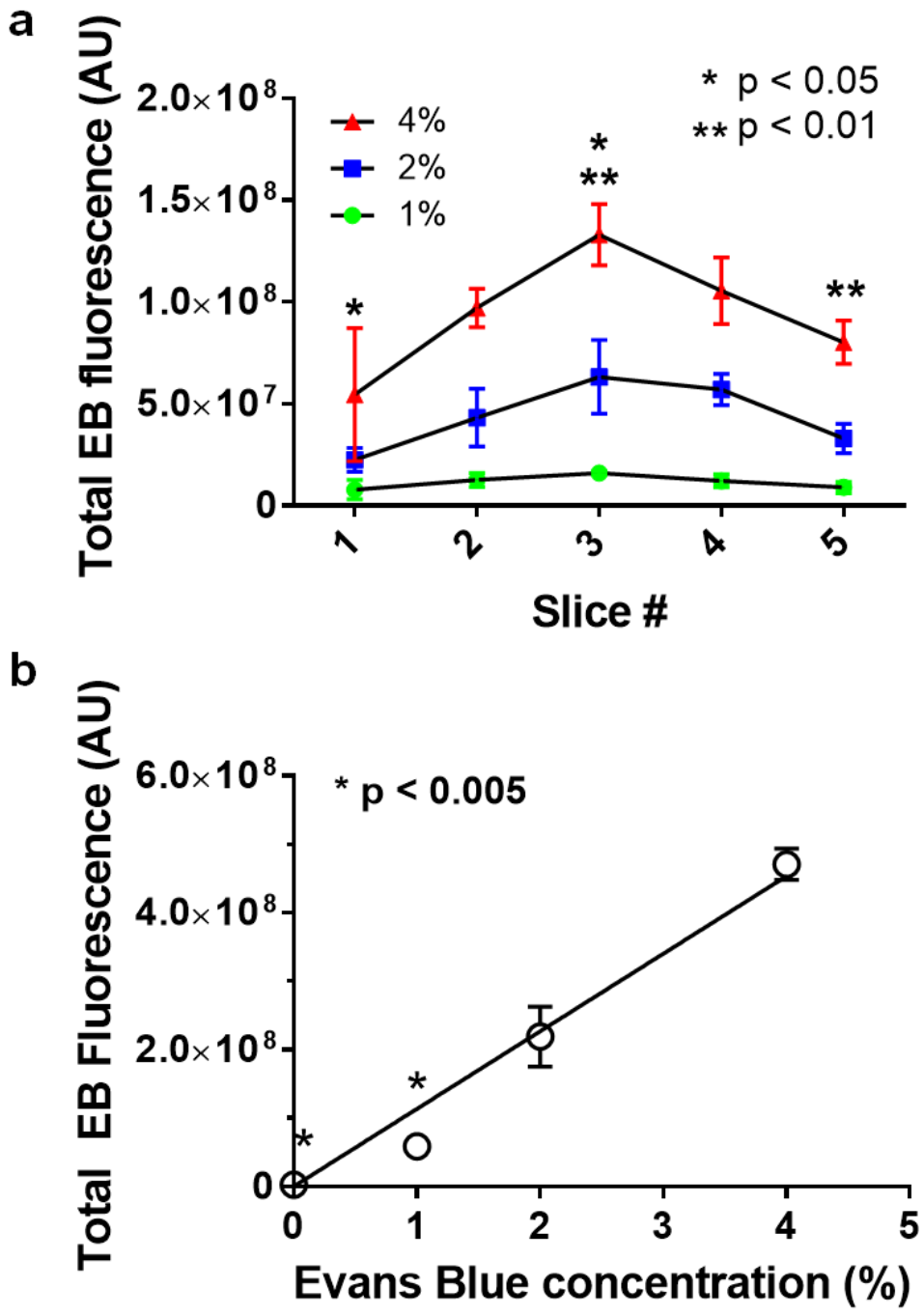

Figure 4.4. a) Fluorescence intensity per slice for 0, 1, 2 and 4% Evans blue, 6-µm microbubble ($4x10^8$ MB/mL·kg) treated brain slices. b) Injected Evans Blue concentration vs. total fluorescence intensity from five sonoporated brain slices (n=3). Line of best fit was obtained through linear regression, with EB concentration vs. fluorescence (x vs. y) represented as $y = 1.1x10^8x$, ($R^2 = 0.97$).

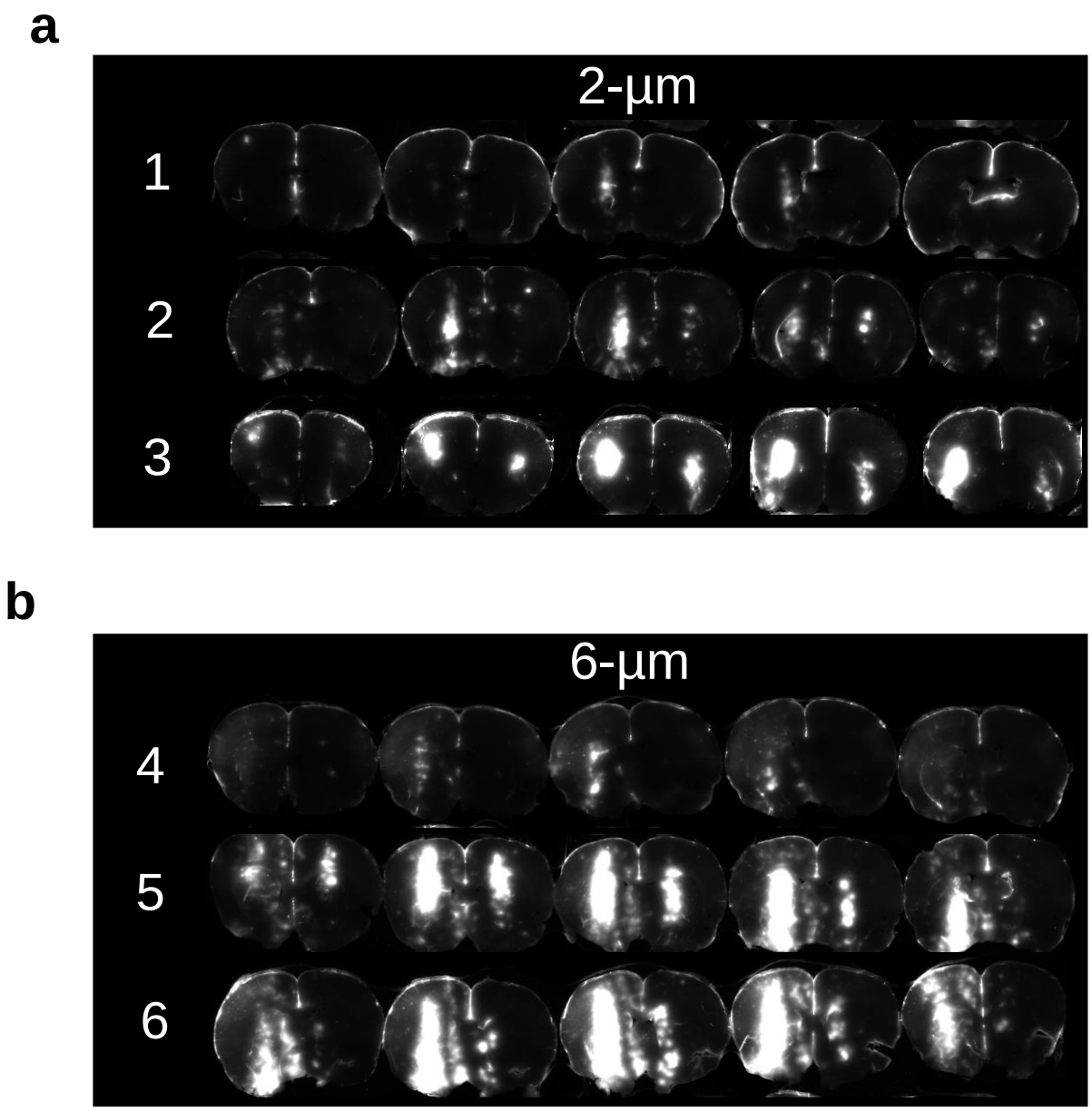

Figure 4.5. NIR scan of brain slices corresponding to brains treated with a) 2-µm microbubbles at 1) $4x10^8$, 2) $2x10^9$, 3) $4x10^9$ MB/kg concentrations, and b) 6-µm microbubbles at 4) $4x10^7$, 5) $2x10^8$, 6) $4x10^9$ MB/kg concentrations.

4.4.4. Effect of MB size, concentration and volume on BBB disruption

Our data showed a linear trend between microbubble number dose and EB fluorescence for both microbubble sizes (Fig. 4.6a). Control injections with 2 wt% EB and without microbubbles gave a very small value for the NIR fluorescence intensity ($1.1 \pm 0.16 \times 10^7$ AU; n = 3). The 2-µm microbubbles showed a linear trend with a relatively small slope (fluorescence intensity = 0.02 [MB], $R^2 = 0.84$). Under the same FUS conditions, 6-µm microbubbles also followed a linear trend with a threefold greater slope (fluorescence intensity = 0.6 [MB], $R^2 = 0.86$).

We next examined the effect of volume dose. Mean microbubble diameters and concentrations were used to calculate the total volumes of 2- and 6-µm microbubbles. Microbubble volume, irrespective of size, produced a linear response in both right (initial sonoporation, 0-5 min) and left (second sonoporation, 5-10 min) hemispheres (Fig. 4.6b). Thus, both microbubble sizes collapsed to a single line when represented as volume dose, for both the right and left striata. The linear fit showed a threefold greater slope for the right hemisphere (fluorescence intensity = 0.006 [MB], $R^2 = 0.90$) compared to the contralateral hemisphere (fluorescence intensity = 0.002 [MB], $R^2 = 0.68$).

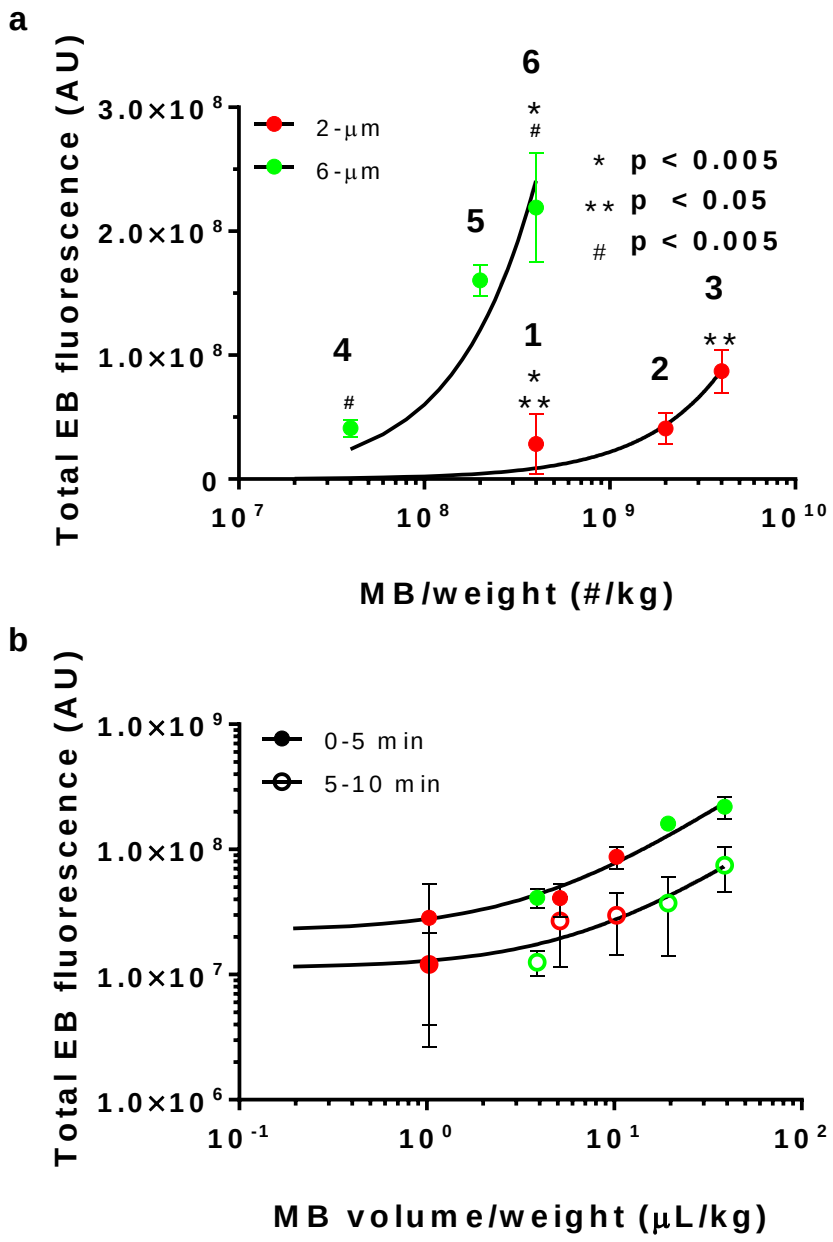

Figure 4.6. (a) Total microbubble volume vs. total Evans Blue fluorescence after the first 5 minutes of sonoporation (solid circles) and subsequent 5 minutes (empty circles). Numbers above data points correspond to brains displayed in Fig. 4.5. Lines of best fit were obtained through linear regression, with concentration vs. fluorescence (x vs. y) represented for 2-μm as $y = 0.02x$ ($R^2 = 0.84$) and 6-μm as $y = 0.6x$ ($R^2 = 0.86$). (b) Lines of best fit for microbubble volume vs. fluorescence (x vs. y) were found to be $y = 0.006x$ ($R^2 = 0.90$) for the first 5 minutes of sonoporation and $y = 0.002x$ ($R^2 = 0.68$) for the second 5 minutes of sonoporation.

4.5. Discussion

The primary goal of this study was to identify the effects of microbubble size, concentration and volume on the extent of trans-BBB molecular delivery with focused ultrasound. The linear dose-response for EB concentration and consistent spatial targeting to the striatum provided confidence that our methodology has sufficient accuracy and precision. In line with past studies, we saw that increasing microbubble size at a fixed concentration increases BBB opening efficiency, with 6-μm diameter microbubbles producing significantly greater EB fluorescence than their 2-μm counterparts. However, when EB fluorescence was plotted against the total volume dose of microbubbles injected, we observed a clear linear relationship with both sizes collapsing to a single line for each of the initial and contralateral treatments. This result demonstrates that size and concentration can be merged into a single parameter, volume dose, to optimize BBB opening efficiency. Thus, a single 6-μm bubble appears to be just as effective at trans-BBB molecular delivery as twenty-seven 2-μm bubbles. This surprising result may be explained from the standpoint of pharmacodynamics, where it was previously demonstrated that at matched volume dose 2- and 6-μm bubbles exhibit essentially the same half-life for *in vivo* ultrasound contrast persistence in mice, even though the echogenicity of the two formulations was drastically different (80). We therefore conclude that for these cationic lipid-shelled microbubbles, persistence in the blood – rather than the particular size-dependent acoustic response – is responsible for BBB opening.

Microbubble surface area is another important consideration. The microbubble surface may be used to load drugs and genes (142,143), but it may also stimulate an immune response (144). Thus, for drug delivery applications involving microbubble loading, it may be advantageous to use smaller microbubbles. For example, at the same volume dose, the 2-μm

diameter bubbles provide threefold more surface area (and hence drug loading) than their 6-μm counterparts. On the other hand, when avoidance of complement activation and immune stimulation takes priority, then 6-μm diameter microbubbles may be preferable. Interestingly, our study on BBB opening and the prior work on ultrasound contrast persistence both indicate that surface area does not have a significant effect on these properties (80).

Chapter 5. Conclusions

5.1. Optimizing in vitro sonoporation with microbubble size

We conclude that microbubble size is an important parameter for *in vitro* sonoporation, markedly affecting microbubble persistence and sonoporation mechanics. Larger microbubbles were shown to persist longer, and induced significantly greater FITC-dextran uptake and EGFP expression, while small-diameter microbubbles effected greater cell viability and sonoporation efficiency. Maximum drug uptake was effected by 6-μm microbubbles at 10^8 MB/mL concentration, while peak sonoporation efficiency was demonstrated with 2-μm microbubbles at 10^8 MB/mL concentration. Bjerknes forces influenced large-diameter microbubbles more than small-diameter microbubbles, and high microbubble concentrations mitigated some of this influence. Additional work is necessary to optimize acoustic parameters for transfection of primary cells, for example, and determine effects of microbubble size on *in vivo* sonoporation.

5.2. High efficiency molecular delivery with sequential low-energy sonoporation bursts

While acoustic parameters and microbubble concentration certainly play significant roles in *in vitro* sonoporation, size appears to provide additional control over the *power* and *energy* delivered to cells *in vitro*. Our data indicate that the prolonged persistence of larger microbubbles delivers more total energy to the cell membrane, increasing cell death. In contrast, owing to a drastically larger expansion ratio, smaller microbubbles deliver high power and a short half-life, porating cells with minimal loss of viability. By extending this efficiency gain through multiple bursts of low-energy sonoporation, we were able to further augment cellular uptake – above the putative 50% threshold – without excessive cell death and lysis. Indeed, two sequential

sonoporations with 2-μm bubbles induced the highest FITC-dextran uptake: in excess of 66% of all cells, including lysed populations, were live and sonoporated. Our multi-color sonoporation assay utilizing FITC- and TRITC-dextran confirmed that this gain proceeds in a multiplicative fashion. Further treatments resulted in diminished viability, indicating a finite energy threshold for cell death. This general strategy to first explore the effects of power and energy on cell uptake and viability, followed by optimization of multiple treatments, can be applied to other cell types *in vitro* and *in vivo* to further enhance the utility of sonoporation for theranostic applications.

5.3. The effect of microbubble-volume dose on blood-brain barrier opening by focused ultrasound

In vivo, we demonstrate a novel and precise method of measuring relative BBB permeabilization utilizing NIR scanning of Evans Blue in freshly obtained rat brains following FUS treatment with microbubbles. Our study focused on the effects of microbubble size (2 and 6 μm diameter) and concentration (10^7 to 10^{10} kg^{-1}) on the extent of molecular dye extravasation into the striatum. Surprisingly, our results demonstrate that the extent of BBB opening increases linearly with volume dose, with both sizes collapsing to a single curve. We conclude that volume dose, not size, is the relevant parameter for optimizing focused ultrasound sonoporation, as it has been shown previously to dictate the pharmacodynamics of ultrasound contrast.

5.4. Future work

Precise characterization of sonoporation parameters aids in the achievement of efficient drug delivery, as demonstrated in the studies presented here. Future studies *in vivo* can take advantage of microbubble volume dose to achieve a specific effect while keeping permeabilization constant: for greater surface drug loading, larger concentrations of smaller microbubbles may be utilized to maximize surface area for a given volume, while larger microbubbles may be selected to minimize surface area and potential immunogenicity for permeabilization-focused applications. Future investigations could characterize the effect of microbubble size on pore-size and disruption of brain parenchyma, which may be important factors in selecting the appropriate microbubble size and concentration. Additionally, the effect of microbubble size and concentration on glial cell activation and inflammation, as well as recovery processes, remains unstudied, and may warrant further optimization in light of recent clinical trials.

References

1. Liu Y, Yan J, Prausnitz MR. Can Ultrasound Enable Efficient Intracellular Uptake of Molecules? A Retrospective Literature Review and Analysis. Ultrasound Med Biol. 2012 May;38(5):876–88.

2. Dove JD, Mountford PA, Murray TW, Borden MA. Engineering optically triggered droplets for photoacoustic imaging and therapy. Biomed Opt Express. 2014 Dec 1;5(12):4417.

3. Mountford PA, Thomas AN, Borden MA. Thermal Activation of Superheated Lipid-Coated Perfluorocarbon Drops. Langmuir. 2015 Apr 28;31(16):4627–34.

4. Okada K, Shimizu M, Isobe T, Kameshima Y, Sakai M, Nakajima A, et al. Characteristics of microbubbles generated by porous mullite ceramics prepared by an extrusion method using organic fibers as the pore former. J Eur Ceram Soc. 2010 Apr;30(6):1245–51.

5. Kendall MR, Bardin D, Shih R, Dayton PA, Lee AP. Scaled-up production of monodisperse, dual layer microbubbles using multi-array microfluidic module for medical imaging and drug delivery. Bubble Sci Eng Technol. 2012 May;4(1):12–20.

6. Ferrara K, Pollard R, Borden M. Ultrasound Microbubble Contrast Agents: Fundamentals and Application to Gene and Drug Delivery. Annu Rev Biomed Eng. 2007;9:415–47.

7. Borden MA, Pu G, Runner GJ, Longo ML. Surface phase behavior and microstructure of lipid/PEG-emulsifier monolayer-coated microbubbles. Colloids Surf B Biointerfaces. 2004 Jun;35(3-4):209–23.

8. Epstein PS, Plesset MS. On the Stability of Gas Bubbles in Liquid-Gas Solutions. J Chem Phys. 1950;18(11):1505.

9. Katiyar A, Sarkar K, Jain P. Effects of encapsulation elasticity on the stability of an encapsulated microbubble. J Colloid Interface Sci. 2009;336(2):519–25.

10. Leighton TG, Wilkinson M, Walton AJ, Field JE. Studies of non-linear bubble oscillations in a simulated acoustic field. Eur J Phys. 1990;11(6):352.

11. Lauterborn W, Ohl C-D. Cavitation bubble dynamics. Ultrason Sonochem. 1997;4(2):65–75.

12. Marmottant P, Meer S van der, Emmer M, Versluis M, Jong N de, Hilgenfeldt S, et al. A model for large amplitude oscillations of coated bubbles accounting for buckling and rupture. J Acoust Soc Am. 2005 Dec 1;118(6):3499–505.

13. Marmottant P, van der Meer S, Emmer M, Versluis M, de Jong N, Hilgenfeldt S, et al. A model for large amplitude oscillations of coated bubbles accounting for buckling and rupture. J Acoust Soc Am. 2005;118(6):3499.

14. de Jong N, Emmer M, Chin CT, Bouakaz A, Mastik F, Lohse D, et al. “Compression-Only” Behavior of Phospholipid-Coated Contrast Bubbles. Ultrasound Med Biol. 2007 Apr;33(4):653–6.

15. Postema M, van Wamel A, Lancée CT, de Jong N. Ultrasound-induced encapsulated microbubble phenomena. Ultrasound Med Biol. 2004 Jun;30(6):827–40.

16. Fan Z, Kumon RE, Park J, Deng CX. Intracellular delivery and calcium transients generated in sonoporation facilitated by microbubbles. J Controlled Release. 2010 Feb;142(1):31–9.

17. Zhou Y, Yang K, Cui J, Ye JY, Deng CX. Controlled permeation of cell membrane by single bubble acoustic cavitation. J Controlled Release [Internet]. 2011 [cited 2012 Aug 21]; Available from: http://www.sciencedirect.com/science/article/pii/S0168365911008534

18. Nomikou N, Tiwari P, Trehan T, Gulati K, McHale AP. Studies on neutral, cationic and biotinylated cationic microbubbles in enhancing ultrasound-mediated gene delivery in vitro and in vivo. Acta Biomater. 2012 Mar;8(3):1273–80.

19. Kamaev PP, Hutcheson JD, Wilson ML, Prausnitz MR. Quantification of Optison bubble size and lifetime during sonication dominant role of secondary cavitation bubbles causing acoustic bioeffects. J Acoust Soc Am. 2004;115(4):1818.

20. De Cock I, Zagato E, Braeckmans K, Luan Y, de Jong N, De Smedt SC, et al. Ultrasound and microbubble mediated drug delivery: Acoustic pressure as determinant for uptake via membrane pores or endocytosis. J Controlled Release. 2015 Jan;197:20–8.

21. Chomas JE, Dayton P, May D, Ferrara K. Threshold of fragmentation for ultrasonic contrast agents. J Biomed Opt. 2001;6:141.

22. Flynn HG, Church CC. Transient pulsations of small gas bubbles in water. J Acoust Soc Am. 1988;84(3):985–98.

23. Hilgenfeldt S, Brenner MP, Grossmann S, Lohse D. Analysis of Rayleigh–Plesset dynamics for sonoluminescing bubbles. J Fluid Mech. 1998;365:171–204.

24. Prentice P, Cuschieri A, Dholakia K, Prausnitz M, Campbell P. Membrane disruption by optically controlled microbubble cavitation. Nat Phys. 2005 Nov;1(2):107–10.

25. Dayton PA, Allen JS, Ferrara KW. The magnitude of radiation force on ultrasound contrast agents. J Acoust Soc Am. 2002 Nov;112(5 Pt 1):2183–92.

26. Akhatov I, Mettin R, Ohl CD, Parlitz U, Lauterborn W. Bjerknes force threshold for stable single bubble sonoluminescence. Phys Rev E. 1997;55(3):3747.

27. Leighton TG, Walton AJ, Pickworth MJW. Primary bjerknes forces. Eur J Phys. 1990;11(1):47.

28. Lai C-Y, Wu C-H, Chen C-C, Li P-C. Quantitative relations of acoustic inertial cavitation with sonoporation and cell viability. Ultrasound Med Biol. 2006 Dec;32(12):1931–41.

29. Qiu Y, Zhang C, Tu J, Zhang D. Microbubble-induced sonoporation involved in ultrasound-mediated DNA transfection in vitro at low acoustic pressures. J Biomech. 2012 May;45(8):1339–45.

30. Gelderblom E, Wolbers F, De Jong N, Van den Berg A, Versluis M. Time-resolved high-speed fluorescence imaging of bubble-induced sonoporation. In: Proceedings of Meetings on Acoustics [Internet]. Acoustical Society of America; 2013 [cited 2014 Nov 19]. p. 075070. Available from: http://scitation.aip.org/content/asa/journal/poma/19/1/10.1121/1.4800331

31. Forbes MM, Steinberg RL, O'Brien WD. Examination of Inertial Cavitation of Optison in Producing Sonoporation of Chinese Hamster Ovary Cells. Ultrasound Med Biol. 2008 Dec;34(12):2009–18.

32. Karshafian R, Bevan PD, Burns PN, Samac S, Banerjee M. Ultrasound-induced uptake of different size markers in mammalian cells. In: IEEE Ultrasonics Symposium 2005. 2005. p. 13–6.

33. Karshafian R, Samac S, Bevan PD, Burns PN. Microbubble mediated sonoporation of cells in suspension: Clonogenic viability and influence of molecular size on uptake. Ultrasonics. 2010 Jun;50(7):691–7.

34. Miller DL, Bao S, Morris JE. Sonoporation of cultured cells in the rotating tube exposure system. Ultrasound Med Biol. 1999;25(1):143–9.

35. Fan Z, Chen D, Deng CX. Improving ultrasound gene transfection efficiency by controlling ultrasound excitation of microbubbles. J Controlled Release. 2013 Sep;170(3):401–13.

36. Larina IV, Evers BM, Esenaliev RO. Optimal drug and gene delivery in cancer cells by ultrasound-induced cavitation. Anticancer Res. 2005 Feb;25(1A):149–56.

37. Mehier-Humbert S, Yan F, Frinking P, Schneider M, Guy RH, Bettinger T. Ultrasound-Mediated Gene Delivery: Influence of Contrast Agent on Transfection. Bioconjug Chem. 2007 May;18(3):652–62.

38. Zhou Y, Shi J, Cui J, Deng CX. Effects of extracellular calcium on cell membrane resealing in sonoporation. J Controlled Release. 2008;126(1):34–43.

39. Kudo N, Okada K, Yamamoto K. Sonoporation by Single-Shot Pulsed Ultrasound with Microbubbles Adjacent to Cells. Biophys J. 2009 Jun;96(12):4866–76.

40. Podell S, Burrascano C, Gaal M, Golec B, Maniquis J, Mehlhaff P. Physical and biochemical stability of Optison, an injectable ultrasound contrast agent. Biotechnol Appl Biochem. 1999 Dec;30 (Pt 3):213–23.

41. Bloch SH, Wan M, Dayton PA, Ferrara KW. Optical observation of lipid- and polymer-shelled ultrasound microbubble contrast agents. Appl Phys Lett. 2004;84(4):631.

42. van Wamel A, Kooiman K, Harteveld M, Emmer M, ten Cate FJ, Versluis M, et al. Vibrating microbubbles poking individual cells: Drug transfer into cells via sonoporation. J Controlled Release. 2006 May;112(2):149–55.

43. Zhou Y, Kumon RE, Cui J, Deng CX. The size of sonoporation pores on the cell membrane. Ultrasound Med Biol. 2009;35(10):1756–60.

44. Fan Z, Liu H, Mayer M, Deng CX. Spatiotemporally controlled single cell sonoporation. Proc Natl Acad Sci. 2012;109(41):16486–91.

45. Fan Z, Chen D, Deng CX. Improving ultrasound gene transfection efficiency by controlling ultrasound excitation of microbubbles. J Controlled Release. 2013 Sep;170(3):401–13.

46. Zeghimi A, Uzbekov R, Arbeille B, Escoffre J-M, Bouakaz A. Ultrastructural modifications of cell membranes and organelles induced by sonoporation. In IEEE; 2012 [cited 2014 Nov 21]. p. 2045–8. Available from: http://ieeexplore.ieee.org/lpdocs/epic03/wrapper.htm?arnumber=6562434

47. Chen X, Leow RS, Hu Y, Wan JMF, Yu ACH. Single-site sonoporation disrupts actin cytoskeleton organization. J R Soc Interface. 2014 Mar 26;11(95):20140071–20140071.

48. Juffermans LJM, Kamp O, Dijkmans PA, Visser CA, Musters RJP. Low-Intensity Ultrasound-Exposed Microbubbles Provoke Local Hyperpolarization of the Cell Membrane Via Activation of BKCa Channels. Ultrasound Med Biol. 2008 Mar;34(3):502–8.

49. Chen X, Wan JMF, Yu ACH. Sonoporation as a Cellular Stress: Induction of Morphological Repression and Developmental Delays. Ultrasound Med Biol. 2013 Jun;39(6):1075–86.

50. Leung KS, Chen X, Zhong W, Yu ACH, Lee C-YJ. Microbubble-mediated sonoporation amplified lipid peroxidation of Jurkat cells. Chem Phys Lipids. 2014 May;180:53–60.

51. Grossi IM, Fitzgerald LA, Umbarger LA, Nelson KK, Diglio CA, Taylor JD, et al. Bidirectional control of membrane expression and/or activation of the tumor cell IRGpIIb/IIIa receptor and tumor cell adhesion by lipoxygenase products of arachidonic acid and linoleic acid. Cancer Res. 1989 Feb 15;49(4):1029–37.

52. Leighton TG. The acoustic bubble. London: Academic Press; 1994.

53. Karshafian R, Bevan PD, Williams R, Samac S, Burns PN. Sonoporation by ultrasound-activated microbubble contrast agents: effect of acoustic exposure parameters on cell membrane permeability and cell viability. Ultrasound Med Biol. 2009;35(5):847–60.

54. Tung Y-S, Choi JJ, Baseri B, Konofagou EE. Identifying the inertial cavitation threshold and skull effects in a vessel phantom using focused ultrasound and microbubbles. Ultrasound Med Biol. 2010 May;36(5):840–52.

55. Tung Y-S, Vlachos F, Feshitan JA, Borden MA, Konofagou EE. The mechanism of interaction between focused ultrasound and microbubbles in blood-brain barrier opening in mice. J Acoust Soc Am. 2011 Nov;130(5):3059–67.

56. Hynynen K, McDannold N, Vykhodtseva N, Jolesz FA. Noninvasive MR imaging-guided focal opening of the blood-brain barrier in rabbits. Radiology. 2001 Sep;220(3):640–6.

57. Choi JJ, Pernot M, Small SA, Konofagou EE. Noninvasive, transcranial and localized opening of the blood-brain barrier using focused ultrasound in mice. Ultrasound Med Biol. 2007 Jan;33(1):95–104.

58. Choi JJ, Feshitan JA, Baseri B, Shougang Wang, Yao-Sheng Tung, Borden MA, et al. Microbubble-Size Dependence of Focused Ultrasound-Induced Blood-Brain Barrier Opening in Mice In Vivo. IEEE Trans Biomed Eng. 2010 Jan;57(1):145–54.

59. McDannold N, Vykhodtseva N, Hynynen K. Blood-brain barrier disruption induced by focused ultrasound and circulating preformed microbubbles appears to be characterized by the mechanical index. Ultrasound Med Biol. 2008 May;34(5):834–40.

60. Choi JJ, Selert K, Gao Z, Samiotaki G, Baseri B, Konofagou EE. Noninvasive and localized blood-brain barrier disruption using focused ultrasound can be achieved at short pulse lengths and low pulse repetition frequencies. J Cereb Blood Flow Metab Off J Int Soc Cereb Blood Flow Metab. 2011 Feb;31(2):725–37.

61. Samiotaki G, Konofagou EE. Dependence of the reversibility of focused- ultrasound-induced blood-brain barrier opening on pressure and pulse length in vivo. IEEE Trans Ultrason Ferroelectr Freq Control. 2013 Nov;60(11):2257–65.

62. Wang S, Samiotaki G, Olumolade O, Feshitan JA, Konofagou EE. Microbubble Type and Distribution Dependence of Focused Ultrasound-Induced Blood–Brain Barrier Opening. Ultrasound Med Biol. 2014 Jan;40(1):130–7.

63. Bakay L, Ballantine HT, Hueter TF, Sosa D. Ultrasonically produced changes in the blood-brain barrier. AMA Arch Neurol Psychiatry. 1956 Nov;76(5):457–67.

64. Tung Y-S, Marquet F, Teichert T, Ferrera V, Konofagou EE. Feasibility of noninvasive cavitation-guided blood-brain barrier opening using focused ultrasound and microbubbles in nonhuman primates. Appl Phys Lett. 2011;98(16):163704.

65. Samiotaki G, Vlachos F, Tung Y-S, Konofagou EE. A quantitative pressure and microbubble-size dependence study of focused ultrasound-induced blood-brain barrier opening reversibility in vivo using MRI. Magn Reson Med. 2012 Mar;67(3):769–77.

66. Wu J. Delivery of DNA and Antibodies Into Cells Using Sonoporation and Electroporation. In AIP; 2005 [cited 2012 Apr 30]. p. 94–9. Available from: http://link.aip.org/link/?APC/754/94/1&Agg=doi

67. Liu Y, Yan J, Prausnitz MR. Can Ultrasound Enable Efficient Intracellular Uptake of Molecules? A Retrospective Literature Review and Analysis. Ultrasound Med Biol. 2012;

68. Christiansen JP, French BA, Klibanov AL, Kaul S, Lindner JR. Targeted tissue transfection with ultrasound destruction of plasmid-bearing cationic microbubbles. Ultrasound Med Biol. 2003;29(12):1759–67.

69. Nomikou N, Tiwari P, Trehan T, Gulati K, McHale AP. Studies on neutral, cationic and biotinylated cationic microbubbles in enhancing ultrasound-mediated gene delivery in vitro and in vivo. Acta Biomater. 2012 Mar;8(3):1273–80.

70. Borden MA, Caskey CF, Little E, Gillies RJ, Ferrara KW. DNA and Polylysine Adsorption and Multilayer Construction onto Cationic Lipid-Coated Microbubbles. Langmuir. 2007 Aug;23(18):9401–8.

71. Panje CM, Wang DS, Pysz MA, Paulmurugan R, Ren Y, Tranquart F, et al. Ultrasound-Mediated Gene Delivery with Cationic Versus Neutral Microbubbles: Effect of DNA and Microbubble Dose on *In Vivo* Transfection Efficiency. Theranostics. 2012;2(11):1078–91.

72. Wang DS, Panje C, Pysz MA, Paulmurugan R, Rosenberg J, Gambhir SS, et al. Cationic versus neutral microbubbles for ultrasound-mediated gene delivery in cancer. Radiology. 2012 Sep;264(3):721–32.

73. Sun RR, Noble ML, Sun SS, Song S, Miao CH. Development of therapeutic microbubbles for enhancing ultrasound-mediated gene delivery. J Control Release Off J Control Release Soc. 2014 May 28;182:111–20.

74. Guzmán HR, Nguyen DX, McNamara AJ, Prausnitz MR. Equilibrium loading of cells with macromolecules by ultrasound: effects of molecular size and acoustic energy. J Pharm Sci. 2002;91(7):1693–701.

75. Chen S, Shohet RV, Bekeredjian R, Frenkel P, Grayburn PA. Optimization of ultrasound parameters for cardiac gene delivery of adenoviral or plasmid deoxyribonucleic acid by ultrasound-targeted microbubble destruction. J Am Coll Cardiol. 2003 Jul 16;42(2):301–8.

76. Bao S, Thrall BD, Miller DL. Transfection of a reporter plasmid into cultured cells by sonoporation< i> in vitro</i>. Ultrasound Med Biol. 1997;23(6):953–9.

77. Chen W-S, Brayman AA, Matula TJ, Crum LA, Miller MW. The pulse length-dependence of inertial cavitation dose and hemolysis. Ultrasound Med Biol. 2003 May;29(5):739–48.

78. Chen W-S, Matula TJ, Brayman AA, Crum LA. A comparison of the fragmentation thresholds and inertial cavitation doses of different ultrasound contrast agents. J Acoust Soc Am. 2003;113(1):643.

79. Fan Z, Chen D, Deng CX. Characterization of the dynamic activities of a population of microbubbles driven by pulsed ultrasound exposure in sonoporation. Ultrasound Med Biol. 2014 Jun;40(6):1260–72.

80. Sirsi S, Feshitan J, Kwan J, Homma S, Borden M. Effect of microbubble size on fundamental mode high frequency ultrasound imaging in mice. Ultrasound Med Biol. 2010;36(6):935–48.

81. Feshitan JA, Chen CC, Kwan JJ, Borden MA. Microbubble size isolation by differential centrifugation. J Colloid Interface Sci. 2009;329(2):316–24.

82. Pellegrin P, Fernandez A, Lamb NJ, Bennes R. Macromolecular uptake is a spontaneous event during mitosis in cultured fibroblasts: implications for vector-dependent plasmid transfection. Mol Biol Cell. 2002;13(2):570–8.

83. Dauer M, Obermaier B, Herten J, Haerle C, Pohl K, Rothenfusser S, et al. Mature Dendritic Cells Derived from Human Monocytes Within 48 Hours: A Novel Strategy for Dendritic Cell Differentiation from Blood Precursors. J Immunol. 2003 Apr 15;170(8):4069–76.

84. Satinover SJ, Dove JD, Borden MA. Single-Particle Optical Sizing of Microbubbles. Ultrasound Med Biol. 2014 Jan;40(1):138–47.

85. Morgan KE, Allen JS, Dayton PA, Chomas JE, Klibaov AL, Ferrara KW. Experimental and theoretical evaluation of microbubble behavior: Effect of transmitted phase and bubble size. Ultrason Ferroelectr Freq Control IEEE Trans On. 2000;47(6):1494–509.

86. Reddy AJ, Szeri AJ. Shape stability of unsteadily translating bubbles. Phys Fluids. 2002;14(7):2216.

87. Magnaudet J, Legendre D. The viscous drag force on a spherical bubble with a time-dependent radius. Phys Fluids. 1998;10(3):550.

88. Cheng L, Fu J, Tsukamoto A, Hawley RG. Use of green fluorescent protein variants to monitor gene transfer and expression in mammalian cells. Nat Biotech. 1996 May;14(5):606–9.

89. Soboleski MR, Oaks J, Halford WP. Green fluorescent protein is a quantitative reporter of gene expression in individual eukaryotic cells. FASEB J. 2005;19(3):440–2.

90. Chomas JE, Dayton P, Allen J, Morgan K, Ferrara KW. Mechanisms of contrast agent destruction. IEEE Trans Ultrason Ferroelectr Freq Control. 2001 Jan;48(1):232–48.

91. Chomas JE, Dayton P, May D, Ferrara K. Threshold of fragmentation for ultrasonic contrast agents. J Biomed Opt. 2001;6:141.

92. Postema M, van Wamel A, Lancée CT, de Jong N. Ultrasound-induced encapsulated microbubble phenomena. Ultrasound Med Biol. 2004 Jun;30(6):827–40.

93. Gerena-L&#xfffd;pez Y, Nolan J, Wang L, Gaigalas A, Schwartz A, Fern&#xfffd;ndez-Repollet E. Quantification of EGFP expression on Molt-4 T cells using calibration standards. Cytometry. 2004 Jul;60A(1):21–8.

94. Fan Z, Chen D, Deng CX. Characterization of the Dynamic Activities of a Population of Microbubbles Driven by Pulsed Ultrasound Exposure in Sonoporation. Ultrasound Med Biol. 2014 Jun;40(6):1260–72.

95. Husseini GA, Pitt WG. Micelles and nanoparticles for ultrasonic drug and gene delivery. Adv Drug Deliv Rev. 2008 Jun;60(10):1137–52.

96. Partlow KC, Brant JA, Marsh JN, Nolta JA, Hughes MS, Lanza GM, et al. Ultrasound energy rapidly labels stem/progenitor cells with nanoparticle beacons without disrupting membrane integrity. In: 2007 Ieee Ultrasonics Symposium Proceedings, Vols 1-6. New York: Ieee; 2007. p. 1768–71.

97. Mo R, Lin S, Wang G, Wang Y, Wu EX. Preliminary in vitro study of ultrasound sonoporation cell labeling with superparamagnetic iron oxide particles for MRI cell tracking. Conf Proc Annu Int Conf IEEE Eng Med Biol Soc IEEE Eng Med Biol Soc Annu Conf. 2008;2008:367–70.

98. Skachkov I, Luan Y, van Tiel S, van der Steen T, Kooiman K, Bernsen M, et al. Ultrasound contrast agents mediated cell labeling for MRI tracking. New York: Ieee; 2012.

99. Kolarova M, Polakova K, Tomankova K, Havrdova M, Markova Z, Zboril R. Rapid Cellular Uptake of Superparamagnetic Iron Oxide Nanoparticles by Using Low-Intensity Ultrasound. Nanocon 2013 5th Int Conf. 2014;578–83.

100. D'Souza AL, Tseng JR, Pauly KB, Guccione S, Rosenberg J, Gambhir SS, et al. A strategy for blood biomarker amplification and localization using ultrasound. Proc Natl Acad Sci. 2009;106(40):17152–7.

101. Forbrich A, Paproski R, Hitt M, Zemp R. Microbubble-Enhanced Ultrasound Liberation of mRNA Biomarkers In Vitro. Ultrasound Med Biol. 2013 Jun;39(6):1087–93.

102. Li YS, Davidson E, Reid CN, McHale AP. Optimising ultrasound-mediated gene transfer (sonoporation) in vitro and prolonged expression of a transgene in vivo: Potential applications for gene therapy of cancer. Cancer Lett. 2009 Jan;273(1):62–9.

103. Iwanaga K, Tominaga K, Yamamoto K, Habu M, Maeda H, Akifusa S, et al. Local delivery system of cytotoxic agents to tumors by focused sonoporation. Cancer Gene Ther. 2007;14(4):354–63.

104. Hallow DM, Mahajan AD, Prausnitz MR. Ultrasonically targeted delivery into endothelial and smooth muscle cells in *ex vivo* arteries. J Controlled Release. 2007;118(3):285–93.

105. Reslan L, Mestas J-L, Herveau S, Béra J-C, Dumontet C. Transfection of cells in suspension by ultrasound cavitation. J Controlled Release. 2010;142(2):251–8.

106. Escoffre J, Novell A, Piron J, Zeghimi A, Doinikov A, Bouakaz A. Microbubble attenuation and destruction: are they involved in sonoporation efficiency? IEEE Trans Ultrason

Ferroelectr Freq Control [Internet]. 2013 Jan [cited 2014 Sep 2];60(1). Available from: http://ieeexplore.ieee.org/lpdocs/epic03/wrapper.htm?arnumber=6396485

107. Hettiarachchi K, Talu E, Longo ML, Dayton PA, Lee AP. On-chip generation of microbubbles as a practical technology for manufacturing contrast agents for ultrasonic imaging. Lab Chip. 2007;7(4):463–8.

108. Talu E, Hettiarachchi K, Powell RL, Lee AP, Dayton PA, Longo ML. Maintaining Monodispersity in a Microbubble Population Formed by Flow-Focusing. Langmuir. 2008 Mar;24(5):1745–9.

109. Talu E, Hettiarachchi K, Zhao S, Powell RL, Lee AP, Longo ML, et al. Tailoring the size distribution of ultrasound contrast agents: possible method for improving sensitivity in molecular imaging. Mol Imaging. 2007;6(6):384.

110. Dollet B, van Hoeve W, Raven J-P, Marmottant P, Versluis M. Role of the Channel Geometry on the Bubble Pinch-Off in Flow-Focusing Devices. Phys Rev Lett [Internet]. 2008 Jan [cited 2015 Mar 19];100(3). Available from: http://link.aps.org/doi/10.1103/PhysRevLett.100.034504

111. Van Hoeve W, Dollet B, Versluis M, Lohse D. Microbubble formation and pinch-off scaling exponent in flow-focusing devices. Phys Fluids 1994-Present. 2011;23(9):092001.

112. Chen C, Zhu Y, Leech PW, Manasseh R. Production of monodispersed micron-sized bubbles at high rates in a microfluidic device. Appl Phys Lett. 2009;95(14):144101.

113. Parhizkar M, Edirisinghe M, Stride E. Effect of operating conditions and liquid physical properties on the size of monodisperse microbubbles produced in a capillary embedded T-junction device. Microfluid Nanofluidics. 2013 May;14(5):797–808.

114. Parrales MA, Fernandez JM, Perez-Saborid M, Kopechek JA, Porter TM. Acoustic characterization of monodisperse lipid-coated microbubbles: Relationship between size and shell viscoelastic properties. J Acoust Soc Am. 2014;136(3):1077–84.

115. Feshitan JA, Chen CC, Kwan JJ, Borden MA. Microbubble size isolation by differential centrifugation. J Colloid Interface Sci. 2009;329(2):316–24.

116. Doinikov AA, Haac JF, Dayton PA. Resonance frequencies of lipid-shelled microbubbles in the regime of nonlinear oscillations. Ultrasonics. 2009;49(2):263–8.

117. Kang-Ho Song, Alexander Fan, Jonathan Brlansky, Tammy Trudeau, Arthur Gutierrez-Hartmann, Michael Calvisi, et al. Efficient microbubble-assisted sonoporation for in vitro applications. In.

118. Lewin PA, Bjørnø L. Acoustically induced shear stresses in the vicinity of microbubbles in tissue. J Acoust Soc Am. 1982;71:728.

119. Wu J. Theoretical study on shear stress generated by microstreaming surrounding contrast agents attached to living cells. Ultrasound Med Biol. 2002;28(1):125–9.

120. Doinikov AA, Bouakaz A. Theoretical investigation of shear stress generated by a contrast microbubble on the cell membrane as a mechanism for sonoporation. J Acoust Soc Am. 2010;128(1):11.

121. Goertz DE, de Jong N, van der Steen AFW. Attenuation and Size Distribution Measurements of Definity™ and Manipulated Definity™ Populations. Ultrasound Med Biol. 2007 Sep;33(9):1376–88.

122. Pardridge WM. The blood-brain barrier: bottleneck in brain drug development. NeuroRx. 2005;2(1):3–14.

123. Pardridge WM, Boado RJ. Reengineering biopharmaceuticals for targeted delivery across the blood-brain barrier. Methods Enzymol. 2012;503:269–92.

124. Marquet F, Tung Y-S, Teichert T, Ferrera VP, Konofagou EE. Noninvasive, Transient and Selective Blood-Brain Barrier Opening in Non-Human Primates In Vivo. Brechbiel MW, editor. PLoS ONE. 2011 Jul 22;6(7):e22598.

125. McDannold N, Vykhodtseva N, Raymond S, Jolesz FA, Hynynen K. MRI-guided targeted blood-brain barrier disruption with focused ultrasound: histological findings in rabbits. Ultrasound Med Biol. 2005 Nov;31(11):1527–37.

126. Ellegala DB. Imaging Tumor Angiogenesis With Contrast Ultrasound and Microbubbles Targeted to v 3. Circulation. 2003 Jul 22;108(3):336–41.

127. Chen CC, Borden MA. Ligand Conjugation to Bimodal Poly(ethylene glycol) Brush Layers on Microbubbles. Langmuir. 2010 Aug 17;26(16):13183–94.

128. Ferrara KW, Borden MA, Zhang H. Lipid-shelled vehicles: engineering for ultrasound molecular imaging and drug delivery. Acc Chem Res. 2009;42(7):881–92.

129. Treat LH, McDannold N, Zhang Y, Vykhodtseva N, Hynynen K. Improved Anti-Tumor Effect of Liposomal Doxorubicin After Targeted Blood-Brain Barrier Disruption by MRI-Guided Focused Ultrasound in Rat Glioma. Ultrasound Med Biol. 2012 Oct;38(10):1716–25.

130. Carpentier A, Canney M, Vignot A, Horodyckid C, Goldwirt L, Leclercq D, et al. Temporary disruption of the blood-brain barrier using an implantable ultrasound system for recurrent glioblastoma patients under IV carboplatin chemotherapy: initial phase 1/2a clinical trial observations. J Ther Ultrasound. 2015;3(Suppl 1):O14.

131. Wang S, Olumolade OO, Sun T, Samiotaki G, Konofagou EE. Noninvasive, neuron-specific gene therapy can be facilitated by focused ultrasound and recombinant adeno-associated virus. Gene Ther. 2015;22(1):104–10.

132. Schlachetzki F, Hölscher T, Koch HJ, Draganski B, May A, Schuierer G, et al. Observation on the integrity of the blood-brain barrier after microbubble destruction by diagnostic transcranial color-coded sonography. J Ultrasound Med Off J Am Inst Ultrasound Med. 2002 Apr;21(4):419–29.

133. Liu H-L, Hua M-Y, Chen P-Y, Chu P-C, Pan C-H, Yang H-W, et al. Blood-brain barrier disruption with focused ultrasound enhances delivery of chemotherapeutic drugs for glioblastoma treatment. Radiology. 2010 May;255(2):415–25.

134. Downs ME, Buch A, Sierra C, Karakatsani ME, Chen S, Konofagou EE, et al. Long-term safety of repeated blood-brain barrier opening via focused ultrasound with microbubbles in non-human primates performing a cognitive task. PloS One. 2015;10(5):e0125911.

135. Thévenot E, Jordão JF, O'Reilly MA, Markham K, Weng Y-Q, Foust KD, et al. Targeted delivery of self-complementary adeno-associated virus serotype 9 to the brain, using magnetic resonance imaging-guided focused ultrasound. Hum Gene Ther. 2012 Nov;23(11):1144–55.

136. Alonso A, Reinz E, Leuchs B, Kleinschmidt J, Fatar M, Geers B, et al. Focal Delivery of AAV2/1-transgenes Into the Rat Brain by Localized Ultrasound-induced BBB Opening. Mol Ther Nucleic Acids. 2013;2:e73.

137. Hsu P-H, Wei K-C, Huang C-Y, Wen C-J, Yen T-C, Liu C-L, et al. Noninvasive and targeted gene delivery into the brain using microbubble-facilitated focused ultrasound. PloS One. 2013;8(2):e57682.

138. Mead BP, Mastorakos P, Suk JS, Klibanov AL, Hanes J, Price RJ. Targeted gene transfer to the brain via the delivery of brain-penetrating DNA nanoparticles with focused ultrasound. J Control Release Off J Control Release Soc. 2016 Feb 10;223:109–17.

139. Song K-H, Fan AC, Brlansky JT, Trudeau T, Gutierrez-Hartmann A, Calvisi ML, et al. High Efficiency Molecular Delivery with Sequential Low-Energy Sonoporation Bursts. Theranostics. 2015;5(12):1419–27.

140. Sirsi SR, Hernandez SL, Zielinski L, Blomback H, Koubaa A, Synder M, et al. Polyplex-microbubble hybrids for ultrasound-guided plasmid DNA delivery to solid tumors. J Controlled Release. 2012 Jan;157(2):224–34.

141. Lindner JR, Coggins MP, Kaul S, Klibanov AL, Brandenburger GH, Ley K. Microbubble persistence in the microcirculation during ischemia/reperfusion and inflammation is caused by integrin-and complement-mediated adherence to activated leukocytes. Circulation. 2000;101(6):668–75.

142. Sirsi SR, Borden MA. Advances in ultrasound mediated gene therapy using microbubble contrast agents. Theranostics. 2012;2(12):1208–22.

143. Sirsi S, Borden M. State-of-the-Art Materials for Ultrasound-Triggered Drug Delivery. Adv Drug Deliv Rev. 2014 Jun 15;0:3–14.

144. Chen CC, Borden MA. The Role of Poly(ethylene glycol) Brush Architecture in Complement Activation on Targeted Microbubble Surfaces. Biomaterials. 2011 Sep;32(27):6579–87.